

**SIMULATION AND DEVELOPMENT OF THE RADIAL
TIME PROJECTION CHAMBER FOR THE BONUS12
EXPERIMENT IN CLAS12**

by

Nathan M Dzbenksi
M.S. May 2016, Old Dominion University

A Dissertation Submitted to the Faculty of
Old Dominion University in Partial Fulfillment of the
Requirements for the Degree of

DOCTOR OF PHILOSOPHY

PHYSICS

OLD DOMINION UNIVERSITY
May 2020

Approved by:

Gail Dodge (Director)

Ian Balitsky (Member)

Balsa Terzic (Member)

Stefen Bultmann (Member)

Holly Gaff (Member)

ABSTRACT

SIMULATION AND DEVELOPMENT OF THE RADIAL TIME PROJECTION CHAMBER FOR THE BONUS12 EXPERIMENT IN CLAS12

Nathan M Dzbenksi
Old Dominion University, 2020
Director: Dr. Gail Dodge

Knowledge of the structure of nucleons (*i.e.* protons and neutrons) is a central topic of interest to nuclear/particle physicists. Much more is known about the structure of the proton than the neutron due to the lack of high-density free neutron targets. The Barely Off-shell Nucleon Structure experiment (BONuS12) at Jefferson Lab (JLab) is a second generation experiment upgraded/optimized to advance our knowledge of the neutron's structure using the deep-inelastic scattering of electrons off deuterium. Typically, since deuterium is a nuclear target, corrections for off-shell and nuclear binding effects must be taken into account in order to extract results on the neutron. These corrections are model-dependent and therefore have limited our success in extracting neutron information using deuterium targets.

In the BONuS12 experiment, 10.6 GeV electrons are scattered off of a deuterium target. By detecting the low momentum spectator proton at backward angles, the uncertainty due to final state interactions is minimized. The goal of the experiment is to measure the ratio of the neutron to proton structure functions (F_2^n/F_2^p) as the Bjorken scaling variable x approaches 1. The newly designed Radial Time Projection Chamber (RTPC) for BONuS12 detects the spectator proton in coincidence with the scattered electron, which is detected in the CEBAF Large Acceptance Spectrometer (CLAS12).

This work presents the simulation and development of the new BONuS12 RTPC. The design, construction, and testing of the Drift-gas Monitoring Sysytem (DMS) for the BONuS12 experiment is also described. The results of the DMS operation as well as the first preliminary data from the BONuS12 experimental run are given. Because the BONuS12 data analysis depends on CLAS12 working effectively, an effort to verify the CLAS12 operation with the extraction of the inclusive deep inelastic cross section from the first experiment in CLAS12 (Run Group A) will be presented.

Copyright, 2020, by Nathan M Dzbenksi, All Rights Reserved.

ACKNOWLEDGMENTS

This project has taken me on an incredible journey filled with equal amounts joy/excitement and self-doubt. Throughout all the ups and downs, hard days and long nights, has been my wife, Kendal. She's been incredibly level-headed and strong during the past 6 years, which was a major reason I was able to do what I did here. I'd also like to thank my son Jensen for making me laugh and smile more than I ever have in my life over the past year. I hope he never stops enjoying life as much as he does now. Lastly, I want to thank my mother who moved her entire life over 600 miles last year to help us take care of Jensen so I could finish this work. Without all three of you, I would not be who I am today.

This project would not have been possible without the incredibly smart and dedicated folks in the BONuS12 group. Gail Dodge, my dissertation director, has been an unwavering source of support and knowledge throughout my time at ODU. I always enjoy working alongside people with such drive and intellect. It forces me to do more and work harder. Sebastian Kuhn, Stephen Bueltmann, Mohammad Hattawy, Gabriel Charles, David Payette, and Jiwan Poudel have served as those motivating people throughout. I want to thank them and the rest of the BONuS12 team for all the help and guidance in this work.

Lastly, I want to thank everyone I have had the pleasure of working with at JLab. I need to thank Maurizio Ungaro and Harut Avakian, particularly, for answering my seemingly endless questions about GEMC and RGA analysis, respectively. Thank you to Eric Christy, another member of the BONuS12 group, who helped me with his model to extract the differential cross sections. Finally, I want to thank the members of my dissertation committee, who all have provided feedback and remained flexible through the strange/difficult times we are currently going through.

Thank you all so much. It has been a pleasure.

TABLE OF CONTENTS

	Page
LIST OF TABLES	viii
LIST OF FIGURES	xiv
Chapter	
1. INTRODUCTION	1
1.1 QUANTUM PHYSICS AND THE STANDARD MODEL IN A NUT-SHELL	1
1.2 THE TROUBLE WITH UNDERSTANDING THE NUCLEON	4
1.3 SCATTERING EXPERIMENTS AND BONUS12	5
1.4 DATA ANALYSIS OF CLAS12 FIRST EXPERIMENT DATA	6
2. PHYSICS FORMALISM	7
2.1 NUCLEON STRUCTURE	8
2.2 ELECTRON-SCATTERING KINEMATICS	10
2.3 ELASTIC SCATTERING	14
2.4 RESONANCE REGION	18
2.5 DEEP INELASTIC SCATTERING	20
2.6 PARTONS AND BJORKEN-SCALING	21
2.7 NUCLEON STRUCTURE-FUNCTION RATIO F_N^2/F_P^2	24
2.8 MODELS AND PREDICTIONS	26
2.9 DIFFICULTIES IN EXTRACTING F_2^N/F_2^P FROM DEUTERIUM ..	28
2.10 SPECTATOR TAGGING	30
2.10.1 IMPULSE APPROXIMATION	32
2.10.2 MINIMIZING FINAL STATE INTERACTIONS	33
3. THE BONUS12 EXPERIMENT	36
3.1 CONTINUOUS ELECTRON BEAM ACCELERATOR FACILITY ..	37
3.2 CEBAF LARGE ACCEPTANCE SPECTROMETER	37
3.2.1 TORUS MAGNET	39
3.2.2 CHERENKOV COUNTERS	39
3.2.3 DRIFT CHAMBERS	40
3.2.4 FORWARD TIME OF FLIGHT	41
3.2.5 ELECTROMAGNETIC CALORIMETER	41
3.2.6 FARADAY CUP	43
3.2.7 SOLENOID MAGNET	43
3.2.8 CENTRAL TIME OF FLIGHT	43
3.3 BONUS12 RTPC	44
3.3.1 COMPONENTS AND THEIR PURPOSE	44

3.3.2	RTPC CONSTRUCTION AND INTEGRATION	48
3.3.3	BONUS12 DRIFT-GAS MONITORING SYSTEM	51
4.	BONUS12 SIMULATION AND DEVELOPMENT	57
4.1	GEANT4 MONTE CARLO (GEMC)	57
4.2	GARFIELD++	58
4.3	BONUS12 RTPC SIMULATIONS	58
4.3.1	GEOMETRY & MATERIALS	59
4.3.2	EVENT GENERATOR	61
4.3.3	DRIFT ELECTRONS	63
4.3.4	GAS OPTIMIZATION	66
4.3.5	DRIFT EQUATIONS	69
4.4	DMS SIMULATIONS	70
4.4.1	GEOMETRY	71
4.4.2	ELECTRIC FIELD	72
4.4.3	DRIFT VELOCITY	76
5.	DATA ANALYSIS	78
5.1	CLAS12 OFFLINE SOFTWARE	78
5.2	CALIBRATION	81
5.3	CHRISTY-BOSTED MODEL AND MC SIMULATED DATA	82
5.4	FIDUCIAL CUTS	83
5.5	KINEMATIC AND PID CUTS	88
5.6	BINNING AND ACCEPTANCE	97
5.7	FARADAY CUP AND INTEGRATED LUMINOSITY	98
5.8	DIFFERENTIAL CROSS SECTION EXTRACTION	101
6.	RESULTS AND CONCLUSIONS	102
6.1	RGA CROSS SECTION	102
6.2	BONUS12	104
6.2.1	DMS	104
6.2.2	RTPC	108
6.3	CONCLUSIONS	112
APPENDICES		
A.	DMS ENGINEERING DRAWINGS	117
B.	DMS GARFIELD++ CODE SNIPPET	125
C.	RGA CROSS SECTION DATA	127
VITA		133

LIST OF TABLES

Table	Page
I Lund file header	62
II Details about each simulated particle in an event (Lund format).....	63
III Summary of calibrated runs for Run Group A. The run number on the far-left column is the run that represents the calibration constants for the run range on the far right.	82
IV Summary of binning in x and y	98

LIST OF FIGURES

Figure	Page
1 The 17 fundamental particles of The Standard Model of Particle Physics.	3
2 The Feynman diagram of neutron decay.	9
3 Feynman diagram of an electron scattering from a nucleon.	12
4 Scattering process on a quasi-static differential cross section.	13
5 The contributions of higher order diagrams.	16
6 Feynman diagram of deep inelastic electron scattering from a proton.	20
7 The transition from inelastic scattering to deep inelastic scattering of a virtual photon and the quark within a nucleon.	22
8 Comparison of CJ15 PDFs $xf(x, Q^2)$ for different flavors ($f = u, d, \bar{d} + \bar{u}, \bar{d} - \bar{u}, s$ and $g/10$).	25
9 Model dependence of F_2^n/F_2^p	27
10 Measured values of F_2^p vs Q^2 for different values of x	29
11 Variations of the F_2^A/F_2^D ratio from unity indicating various nuclear binding effects.	30
12 Impulse approximation (a) and final state interaction diagrams (b).	31
13 (a) The Deep Inelastic Scattering ratio n_D^{FSI}/n_D calculated <i>vs.</i> the momentum p_s of the spectator nucleon emitted at different angles θ_s . (b) The Deep Inelastic Scattering ratio n_D^{FSI}/n_D calculated <i>vs.</i> the emission angle θ_s of the spectator for different values of the spectator momentum.	34
14 CEBAF upgraded for the 12 GeV era.	36
15 The CEBAF Large Acceptance Spectrometer at 12 GeV (CLAS12).	38
16 The High Threshold Cerenkov Counter.	40
17 Hexagonal wire layout for the drift chamber.	40
18 Exploded view of a sector of the Electromagnetic Calorimeter (EC) for CLAS12.	42

19	The Central Time of Flight Detector.	44
20	Cross section of the RTPC showing a proton traversing the detector with ionization electrons drifting toward the readout pad board.	45
21	(a) Electron microscope picture of a section of typical GEM electrode, 50 μm thick. The holes pitch and diameter are 140 and 70 μm , respectively. (b) Electric field in the region of the holes of a GEM electrode.	46
22	Design of the RTPC with only one-quarter of the translation boards attached.	47
23	Map of the DREAM chip.	47
24	The BONuS12 data acquisition map. Signals from the readout pad board go through the translation boards to the front-end unit electronics. The raw events get read into the slow controls and gets uploaded to the back end unit computer systems.	48
25	Assembly station for the RTPC.	49
26	The fully assembled BONuS12 RTPC with the FEUs attached, but not yet with the 3-layer FMTs attached.	50
27	The RTPC gas panel. The target gas flows through the top part of the panel, the buffer gas flows through the middle region of the panel, and the drift gas flows through the bottom region of the panel.	51
28	Design concept of the Drift-gas Monitoring System (DMS) for the BONuS12 experiment.	52
29	Partial assembly of the DMS showing the wired cathode at the top and the anode ground plate at the bottom with the field shaping electrodes in between.	53
30	Assembled DMS with electrode wiring.	53
31	Fully assembled DMS with electronics panel shown in the back.	54
32	Cathode and electrode HV supply circuit.	55
33	Anode HV supply circuit.	55
34	The DMS DAQ flow from signal to computer.	56
35	BONuS12 RTPC geometry implemented in GEMC	60

36	CLAS12 Solenoid Field Map (courtesy of V. Lagerquist)	64
37	Magnetic field strength versus z for values of r	65
38	Drift angle vs drift time for various gas mixtures. Only electrons created at $r = 6$ cm are included in this plot.....	66
39	Diffusion in drift angle vs diffusion in drift time for various gas mixtures..	68
40	Drift time versus drift angle for He:CO ₂ using various potentials.....	69
41	Plots of drift electron properties.	70
42	Parameters a and b for drift angle (a_ϕ and b_ϕ) and drift time (a_t and b_t). .	71
43	Electric-field contour map along the cross-section in $x - y$ plane.....	73
44	Electric-field profile along the plane of the anode. The cathode and anode's locations are denoted as blue and red lines respectively. The sources and PMT's location and subsequent electron beams are pictured as green dotted lines.	73
45	Zoomed in electric-field profile to between the two sources. The cathode and anode's locations are denoted as blue and red lines respectively. The sources and PMT's location and subsequent electron beams are pictured as green dotted lines.....	74
46	Electric field profile with electrode separation of 1.2 mm and diameter of 50 μm	75
47	Electric field profile with electrode separation of 1.2 mm and diameter of 1 mm.	75
48	Electric field profile with electrode separation of 0.6 mm and diameter of 2 mm.	76
49	Simulated drift time for ionization electrons created by radiation electrons from the near and far sources to the anode. The gas mixture is 80:20 He:CO ₂ with a cathode potential of -6 kV and an anode potential of +1800V.	77
50	Total cross section vs. W^2 for existing data (black triangles) and the Christy-Bosted fit in red.	83

51	Count distributions of the U, V, and W dimensions of the pre-shower calorimeter (PCAL). The raw histograms are on the top and the bottom histograms contain the cuts: $U > 30$ cm, $30 < V < 390$ cm, and $30 < W < 390$ cm. All plots are normalized to account for any mismatch in total statistics. Red lines are from RGA data and black lines are for the Monte-Carlo (MC) data.....	84
52	Count distributions of the U, V, and W dimensions of the inner EC. The raw histograms are on the top and the bottom histograms contain the cuts on the PCAL: $U > 30$ cm, $30 < V < 390$ cm, and $30 < W < 390$ cm. All plots are normalized to account for any mismatch in total statistics. Red lines are from RGA data and black lines are for the Monte-Carlo (MC) data.	85
53	Count distributions of the U, V, and W dimensions of the outer EC. The raw histograms are on the top and the bottom histograms contain the cuts on the PCAL: $U > 30$ cm, $30 < V < 390$ cm, and $30 < W < 390$ cm. All plots are normalized to account for any mismatch in total statistics. Red lines are from RGA data and black lines are for the Monte-Carlo (MC) data.	86
54	2D histograms of the uncut PCAL hits on the left and after the fiducial cuts are applied (right).	86
55	2D histograms of the inner EC hits. On the left is before cuts on the PCAL, and on the right is after the fiducial cuts on the PCAL are applied.	87
56	2D histograms of the outer EC hits. On the left is before cuts on the PCAL, and on the right is after the fiducial cuts on the PCAL are applied.	87
57	The electron vertex v_z before (left) and after (right) all described cuts. Red lines are from RGA data and black lines are for the Monte-Carlo (MC) data.	89
58	Sampling fraction as a function of particle momentum. The dots represent the mean along the center and values $\pm 2.5\sigma$ from that mean. The red lines are the fitted polynomials.....	89
59	Slice of the sampling fraction for $2.58 < p < 3.66$ GeV fitted to a Gaussian. The sigma is used to find the $\pm 2.5\sigma$ fit seen in Fig. 58.	90
60	Kinematic variables before cuts. Red lines are from RGA data and black lines are for the Monte-Carlo (MC) data.	92
61	Kinematic variables after all described cuts. Red lines are from RGA data and black lines are for the Monte-Carlo (MC) data.	92

62	E' , EC energies, and nphe before cuts. Red lines are from RGA data and black lines are for the Monte-Carlo (MC) data.	93
63	E' , EC energies, and nphe after all described cuts. Red lines are from RGA data and black lines are for the Monte-Carlo (MC) data.....	93
64	E' vs. θ and W vs. x_B before cuts. The Monte Carlo data is on the left and the RGA data is on the right.	94
65	E' vs. θ and W vs. x_B after all described cuts. The Monte Carlo data is on the left and the RGA data is on the right.....	94
66	Q^2 vs. W and Q^2 vs x_B before cuts. The Monte Carlo data is on the left and the RGA data is on the right.	95
67	Q^2 vs. W and Q^2 vs x_B after all described cuts. The Monte Carlo data is on the left and the RGA data is on the right.....	95
68	$E_{EC_{tot}}$ vs E_{PCAL} and Sampling fraction vs. p before cuts. The Monte Carlo data is on the left and the RGA data is on the right.....	96
69	$E_{EC_{tot}}$ vs E_{PCAL} and Sampling fraction vs. p after all described cuts. The Monte Carlo data is on the left and the RGA data is on the right.....	96
70	Binning in the x, y space for MC data (left) and RGA Run 5036 data (right). These plots contain all events that pass the inclusive DIS cuts imposed as described in Section 5.5.....	97
71	Acceptance for $y = 0.3375$ (left) and $y = 0.4175$ (right) vs x	99
72	Acceptance for $y = 0.4875$ (left) and $y = 0.5625$ (right) vs x	99
73	Acceptance for $y = 0.6375$ (left) and $y = 0.7125$ (right) vs x	100
76	Plots of inclusive DIS differential cross section vs x_B for various values of y . The green band represents the uncertainty of the DIS cross section calculated from the Christy-Bosted fits to F_1 and F_2 [46].	103
77	DMS drift time histograms for CH1 (left) and CH2 (right) on Run 11953.	105
78	DMS drift velocity vs. time graph during Run 11953.....	105
79	DMS drift velocity for channel 1 vs. run.	106
80	DMS drift velocity for channel 2 vs. run.	106
81	DMS gas pressure vs. run.	107

82	DMS drift velocity over all RGF runs.	107
83	Two examples of reconstructed tracks in one time window in the RTPC using Version 27 of the reconstruction software in a Cartesian x, y space for Run 11637 (2.14 GeV). [<i>Courtesy D. Payette.</i>]	108
84	Two examples of reconstructed tracks in one time window in the RTPC using Version 26 of the reconstruction software in an Cartesian x, y space for Run 12240 (10.4 GeV). [<i>Courtesy D. Payette.</i>]	109
85	The time shift (t_{shift}), momentum, and theta (θ) of the reconstructed protons in Run 11637.	110
86	On the left: 2D distributions of the calculated momentum (“mom_predicted” in the plot) on the x -axis and reconstructed momentum (“mom_measured” in the plot) for protons on the y -axis in Run 11637. On the right: The difference between the predicted and measured values of the momentum for Run 11637.	111
87	On the left: 2D distributions of the calculated theta (“theta_predicted” in the plot) on the x -axis and reconstructed theta (“theta_measured” in the plot) for protons on the y -axis in Run 11637. On the right: The difference between the predicted and measured values of theta for Run 11637.	111

CHAPTER 1

INTRODUCTION

Throughout human history we have been driven to understand the world around us. It is surely one of the characteristics that defines us as a species. Coupling that curiosity with our ability to create and construct incredible machines has allowed us to probe some of the most elusive parts of our Universe. From the Hubble Telescope taking images of the earliest moments of our Universe to the Large Hadron Collider probing the most fundamental particles that we currently know, we have been wildly successful at fulfilling that drive to understand.

Despite that success, there are many issues that continue to elude us. We currently have no tangible explanation for the asymmetry between matter and anti-matter. In the very early Universe there were equal amounts of matter and anti-matter, yet today our visible Universe seems to be comprised primarily of matter and not anti-matter. Another puzzle is that of dark matter and dark energy, which are collectively believed to make up 96% of our Universe, are phenomena we know almost nothing about. Even the matter that we do know about, we know surprisingly little about its structure and composition.

Atoms make up much of that visible Universe. Since the early 1900's we have known these atoms to be made of protons, neutrons and electrons. The discovery of protons and electrons essentially occurred in the late 19th Century, but the neutron was not discovered until 1932 by Sir James Chadwick. The neutron was not just found later than the electron and proton, we also know much less about it. The electron is well-known in the physics community to be a near point-like particle made of no constituent particles, but the proton and neutron have been proven to be made of more fundamental particles.

1.1 QUANTUM PHYSICS AND THE STANDARD MODEL IN A NUTSHELL

Knowing exactly what makes up these protons and neutrons relies on knowledge of the Standard Model of Particle Physics, often simply referred to as The Standard

Model. This model, developed in stages throughout the latter half of the 20th Century, essentially lays out the existence of all possible fundamental¹ particles in the Universe.

There are 17 particles in the Standard Model (outlined in Fig. 1). These 17 can first be broken down into two subgroups called bosons and fermions. Bosons follow what is known as Bose-Einstein statistics, which essentially states that they can occupy the same space at the same time. In the language of quantum physics, two bosons can be described by the same quantum numbers. These bosons, with a slight exception for the Higgs boson, are all considered force carriers. Photons are the force carriers for the electromagnetic force. Gluons carry the strong force. W and Z bosons are the force carriers for the weak force. The Higgs boson is a bit different in that it is not necessarily a force carrier. Its existence is tied to the breaking of electroweak symmetry² and it gives fermions their mass.

The other subgroup is fermions, which are 12 particles³ that obey a Fermi-Dirac statistical rule called the Pauli Exclusion Principle. Developed by Enrico Fermi, Paul Dirac and Wolfgang Pauli, this rule states that fermions cannot occupy the same place at the same time. Again in quantum physics language, no two fermions can be described by the same quantum numbers. There are two types of fermions in the Standard Model: 6 quarks and 6 leptons. Leptons, which include electrons, pions, tau and their associated neutrinos, cannot combine together alone to make larger structures. Quarks, on the other hand, do combine to make larger structures, like protons, neutrons, atoms, molecules, people and light posts (obviously with the contribution of some leptons). Quarks also obey the exclusion principle, which is why - with the Coulomb repulsion of atomic electrons - walking into a light post hurts. You both cannot be in the same place at the same time.

Quantum numbers, the characteristics that help define the differences between fermions and bosons, are what describe a quantum system. More precisely, quantum numbers are the eigenvalues of operators that commute with the Hamiltonian. These quantum numbers can describe quantities like angular momentum, spin or

¹The word “fundamental” here means that they are not made of constituent particles.

²In the early Universe, the electromagnetic and weak forces were one force. As the Universe began to cool, the symmetry that kept these two forces together broke. The Higgs boson essentially facilitated that breaking.

³Each of these fermions also has an associated anti-particle, which has the same mass but opposite electric charge. For example, an anti-electron (known as a positron) also has a mass of 0.511 MeV/c² but a charge of +1.

THE STANDARD MODEL

of particle physics

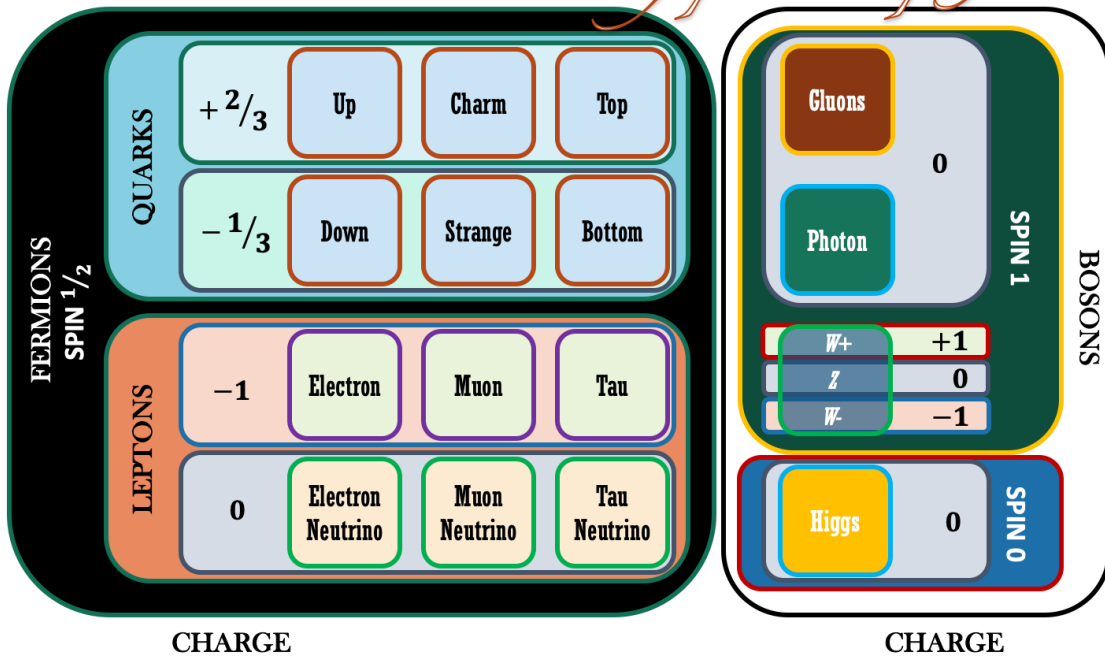


Fig. 1: The 17 fundamental particles of The Standard Model of Particle Physics.

parity. The namesake to these numbers and this entire field of physics comes from the fact that these quantities exist in discrete steps (*e.g.* integer or half-integer steps), and are thus quantized.

One of those quantized observables is called spin. Because these fundamental particles are so incredibly small, they are considered point-like. Therefore many of these quantum numbers are simply mathematical constructs that tend to correspond to something physical we are familiar with. The spin quantum number is no exception. Fundamental fermions, as seen in Fig. 1, have spin $1/2$, while fundamental bosons have integer spin of 0 or 1. Two, three or more quarks combine by way of gluons (*i.e.* the strong force). Two quarks combine to make particles called mesons⁴ (*e.g.* pions and kaons) and their spin states combine to form an overall integer 0 or 1, which also makes them bosons. Three quarks combine to make particles called baryons⁵ (*e.g.*

⁴The word meson comes from the Greek word μεσοσ(“mesos”) meaning medium.

⁵Baryon comes from the a Greek word βαρυσ(“varys”) meaning heavy.

protons and neutrons), which have spin 1/2 or 3/2 making them fermions as well. The collective group of quarks, mesons, and baryons are known as hadrons⁶.

Charge is another important quantized observable. When three quarks combine to make something like a proton or neutron, their charges also combine. A proton, for example, is made of two up quarks⁷ (each with charge +2/3) and a down quark (charge -1/3), so its overall charge is +1. A neutron is made of two down quarks and an up quark, so its charge is zero.

1.2 THE TROUBLE WITH UNDERSTANDING THE NUCLEON

Protons and neutrons make up the nucleus of an atom so they are called nucleons. These nucleons are not just made of three stationary quarks, but are very dynamic and busy particles. These three quarks that define whether it is a proton or neutron are called valence quarks. However, there are also quark-antiquark pairs that are in a constant state of creation and annihilation, called sea quarks. Then there are gluons which are carriers of the strong force binding quarks together. All of these particles have momenta and collectively define the structure of the nucleon. One issue in particle physics has been defining this structure, including the size of these nucleons and the momentum distribution of those fundamental particles that exist within it.

There has been a lot of effort exploring the structure and momentum distribution of the proton, yet there are some major puzzles that still exist. One of the most famous has to do with the proton spin called the “proton spin crisis.” This crisis refers to our collective inability to explain how all of the particles that exist in the proton conspire together to always give the proton spin 1/2. Less famous puzzles include knowing the proton radius, where its mass comes from, and what the momentum distribution is of its fundamental constituent particles.

All of these puzzles also exist for the neutron, except with even less understanding. Whereas protons (more specifically hydrogen) are easily confined to form targets for experiments, no such free neutron targets exist. Free neutrons are unstable and decay in about 15 minutes. Also because they do not have electric charge, they cannot be easily confined into a dense target. One new experiment designed to solve

⁶Hadron comes from the Greek word $\alpha\delta\rho\sigma$ (“adros”) meaning massive or large. Point-like quarks can combine to make a particles much heavier than the combined quarks themselves.

⁷Quark names are essentially meaningless. There is no physical characteristics that warrant a quark being called up or strange. They were simply given a name that stuck.

this problem of neutron targets is the Barely Off-shell Nucleon Structure Experiment at 12 Giga-electron Volts (or BONuS12). The BONuS12 experiment will use a target filled with deuterium (*i.e.* a nucleus consisting of one proton and one neutron and orbited by a single electron) to confirm or reject theories related to the structure of the neutron and the momentum distribution of its constituents.

1.3 SCATTERING EXPERIMENTS AND BONUS12

In order to probe the enigmas of particles that are on the order of 50 trillion times smaller than a grain of sand, particle and nuclear physicists often use scattering experiments. These experiments accelerate particles to known energies and collide them with a target. The collision of accelerated particles on a target causes them both to scatter and, in some cases, fragment. The scattered particles resulting from the collision then enter particle detectors where information like energy, position, momentum, and time are gathered by exploiting various physics processes. With this information physicists can extract quantities related to the structure of nucleon (*e.g.* the momentum distribution of the fundamental constituents within it).

The Thomas Jefferson National Accelerator Lab (JLab) in Newport News, Virginia, contains an electron accelerator used for scattering experiments meant to explore nuclear and subatomic matter. Here is where, in 2005, the first BONuS experiment ran in JLab’s Experimental Hall B. The goal of that experiment was to explore the structure of the neutron by investigating the momentum distribution of the quarks and gluons inside. The results of the experiment made progress in reducing uncertainties in the quantities that describe neutron structure, which helped to begin confirming or denying some theories that exist which attempt to describe these characteristics.

Jefferson Lab, in 2012, began an energy upgrade to bring the electron beam energy to 12 GeV, and with that came the development of an upgraded BONuS experiment (called BONuS12). Just like the BONuS6 experiment (*i.e.* the original BONuS experiment that ran at 6 GeV), it is designed to explore a larger range in the momentum distribution of its fundamental constituent particles. Changes were made to improve the overall operation of the detector.

1.4 DATA ANALYSIS OF CLAS12 FIRST EXPERIMENT DATA

Throughout the rest of this work we will primarily discuss BONuS12, the physics necessary to understand its goals and operation, and the efforts made to make the BONuS12 experiment operational before its Spring 2020 run. As a part of that BONuS12 development comes the need to confirm that data coming in from Hall B experiments at JLab makes sense and is calibrated correctly.

While the BONuS12 Radial Time Projection Chamber (RTPC) will detect scattered protons, the scattered electron will enter the existing detectors in Hall B (known as CLAS12), so understanding that electron data is important. For that, a portion of this work will be dedicated to analyzing data from the first experiment that ran after the start of the 12 GeV physics era at JLab (*i.e.* Run Group A). The process known as inclusive deep inelastic scattering will be examined since we know much about it. The word *inclusive* means that in the scattering of an electron off a nucleon or atom, we detect and analyze only the the electron, which means all possible particles created are included in the interaction. In particular, we will look at what is known as the cross section of the process from the data and compare it to simulations that use well known values of that cross section. This will provide evidence that the detectors within CLAS12, where the BONuS12 experiment will run, are working effectively and are calibrated correctly.

CHAPTER 2

PHYSICS FORMALISM

The idea that matter is made of elementary particles has been around since about the 6th Century B.C.E., but it was not until 2400 years later in 1808 [1] that the first publication came out by John Dalton describing small particles called atoms. Between 1879 [2] and 1897 [3] works that discovered the existence of electrons started to be published and taken seriously. By 1914, Rutherford [4] and others established that there was a dense structure at the center of atoms that had a positive charge surrounded by the lighter-mass electrons on the outside. In 1913, the positively charged *nucleus* of the hydrogen atom was confirmed by Rutherford [5], which he called the *proton*. It was not until 1932 that James Chadwick discovered the neutron.

Alongside the discoveries of these subatomic particles was the development of theories explaining their behavior. Electrons began to be understood as both a particle and a wave, depending on which way you try to observe it. Then it was realized all particles can act this way. Max Plank developed the idea that energy radiated from atomic systems did so only in discrete quantities or *quanta*. In 1905, Einstein [6] proclaimed that light is made of particles called photons, which was consistent with Plank's *quantum* hypothesis. Throughout the early 1900's this concept of quantum mechanics was developed.

In this journey through understanding the quantum world came the realization that the four fundamental forces in nature (*i.e.* gravity, electromagnetic, strong and weak nuclear) are fields that interact with quantum particles, which were also considered fields. The theory describing particles interacting via the electromagnetic force became known as quantum electrodynamics (QED), which was developed around the 1950-1960's. The interaction of particles with the strong nuclear force was described by a theory called quantum chromodynamics (QCD) developed around the late 1970's. This chapter will, in effect, follow this history with a slant toward its relevance for the BONuS12 experiment.

2.1 NUCLEON STRUCTURE

The proton and neutron are the two components that make up a group called nucleons since they make up the nucleus of an atom. They both interact through all four forces (*i.e.* strong nuclear, weak nuclear, electromagnetic, and gravitational). As mentioned in the Introduction, they are both fermions. Because they are both made up of three quarks, they are also both baryons.

The quarks that make up these nucleons (all baryons, in fact) and that are responsible for the nucleon's quantum numbers are called *valence quarks*. The proton is made of two *up* valence quarks and one *down* valence quark, denoted by *uud*. The neutron is made up of two down valence quarks and an up valence quark, or *udd*. Of course, there are also *sea quarks* made of $q\bar{q}$ pairs, where $q\bar{q}$ is any variety of quark-antiquark pair. However, the strong interaction which binds all of these quarks together acts the same no matter the quark flavor.¹ Therefore, the quark model does not predict any distinctions between protons and neutrons. In fact, from the view of the strong force, they are the identical particle in different states.² Yet, protons and neutrons are clearly not identical particles.

There are obvious differences between the two nucleons. One important difference between nucleons is their stability when not bound to each other. The proton is a stable particle on its own, with a lifetime of more than 2.1×10^{29} years. The neutron, however, has a lifetime of about 882 seconds (or about 15 minutes). The proton is the only nucleon that can exist in a nucleus on its own, which is the hydrogen atom. The more obvious difference in the two nucleons is their electric charge. The charge of the proton is +1 in units of electron charge, while the neutron is neutral (*i.e.* charge = 0). This charge arises from their valence quark content. The up quark has a charge equal to $q_u = +2/3$ and the down quark has a charge of $q_d = -1/3$, so for the proton with *uud* quarks,

$$2q_u + q_d = 2(+2/3) + (-1/3) = +1, \quad (1)$$

¹The word *flavor* is used to describe a type of quark. Remember there are 6 *flavors* of quarks: up, down, top, bottom, strange, and charm.

²There is a symmetry of the strong interaction in neutrons and protons called isospin (also referred to as isotopic or isobaric spin). Isospin is a dimensionless quantity that does not describe a physical “spin” of the particle. It does, however, offer a description of the two different states of nucleons. In particular, the projection of isospin along the z-axis (I_z or I_3) provides insight into the difference between protons and neutrons, which are otherwise almost identical particles. Protons have $I_z = 1/2$ and neutrons have $I_z = -1/2$.

and for the neutron with ddu quarks,

$$2q_d + q_u = 2(-1/3) + (+2/3) = 0. \quad (2)$$

The spatial charge distribution of quarks is well known for both nucleons. The momentum distribution of those quarks inside the nucleon, however, is not as well known, particularly for the neutron. The same is true for the overall structure of the nucleons, again more so for the neutron.

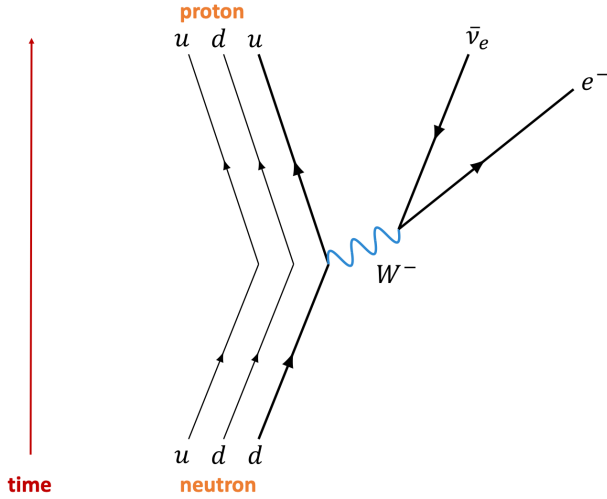


Fig. 2: The Feynman diagram of neutron decay.

The discrepancy of knowledge between the proton and neutron is the last major difference of the nucleons we will discuss here, because it goes directly toward the principle goal of the BONuS12 experiment. We know much more about the structure of the proton and momentum distribution of the quarks inside the proton for the reason discussed in the last paragraph. That is, a single protons can make up the nucleus of an atom, while no such atom exists with a single neutrons. Free neutrons soon decay via the weak interaction

$$n \longrightarrow p + e^- + \bar{\nu}_e, \quad (3)$$

as seen in Fig. 2 as a Feynman diagram. Feynman diagrams were developed by physicist Richard Feynman to display particle interactions that occur in a relatively simplistic manner. Moving from the bottom to the top in the diagram of Fig. 2, we see a down quark within the neutron change states to an up quark mediated by the W^- boson, which then decays to an electron (e^-) and electron antineutrino ($\bar{\nu}_e$).

This neutron decay occurs in about 15 minutes. That decay coupled with the fact that the neutron has no electric charge makes isolating neutrons to create a dense target for scattering experiments extremely difficult. Yet, scattering experiments are the primary means by which physicists study the structure of particles. Therefore, studying the structure of the neutron is inherently made difficult by this lack of free neutron target.

2.2 ELECTRON-SCATTERING KINEMATICS

To study the structure and physics of particles, nuclear and particle physicists use scattering experiments. There are two ways of creating a scattering experiment. One way is to accelerate a light particle (an electron, for example) and direct it toward a stationary target, which is the method used at Jefferson Lab in Newport News, Virginia. The other way is to accelerate two particles in opposite directions and then direct the two toward each other, which is the method used at the Large Hadron Collider (LHC) at CERN in Geneva, Switzerland. The physics, or kinematics,³ of both scattering experiments is essentially the same.

When the scattering particle and target collide, some of the momentum and energy of the scattered particle is transferred to the target particle. Nuclear and particle physicists express that energy and momentum as a four-momentum. Classical momentum is a vector, which means it has a magnitude and direction. That direction is typically expressed in three dimensions (for the familiar Cartesian coordinate system that would be along the x, y, and z-axis). Therefore a momentum can be expressed as $\mathbf{p} = (p_x, p_y, p_z)$, where \mathbf{p} is the momentum vector bold-faced to indicate that it is a vector. Because, in particle physics, the particles travel close to the speed of light, we have to deal with special relativity. For the purposes of this work, special relativity essentially forces us to consider not just three-dimensional space, but four dimensional space-time with different reference frames for any non-accelerating moving objects. This drives us to require there be a four-dimensional space-time momentum $p = (p_0, p_1, p_2, p_3)$, where $p_1 = p_x$, $p_2 = p_y$, and $p_3 = p_z$ in Cartesian coordinates. The new term p_0 is equal to E/c , where E is the energy of the particle and c is the speed of light.

³The word kinematics refers to the mechanics of the particles without concern for the forces that caused the motion. Essentially, we are not concerned with *how* the particles were accelerated, just that they have a particular energy at the time of collision.

If we take this four-momentum

$$p_\mu = \left(\frac{E}{c}, p_x, p_y, p_z \right), \quad (4)$$

where μ is just an index indicating a particular particle, and square it, we have

$$p^\mu p_\mu = -\frac{E^2}{c^2} + p_x^2 + p_y^2 + p_z^2 = -\frac{E^2}{c^2} + \mathbf{p}^2. \quad (5)$$

This quantity is invariant under a Lorentz transformation (meaning it remains the same no matter the non-accelerating reference frame) and is equal to the Lorentz scalar $-m^2 c^2$, which means

$$-\frac{E^2}{c^2} + p^2 = -m^2 c^2. \quad (6)$$

Multiplying both sides of Eq. 6 by $-c^2$ and rearranging a little gives us

$$E^2 = p^2 c^2 + m^2 c^4, \quad (7)$$

which if we take the square root of both sides results in

$$E = \sqrt{(pc)^2 + (mc^2)^2}. \quad (8)$$

In the rest frame of the particle (*i.e.* the frame where the particle is considered to have no momentum, thus $p = 0$), this equation reduces to something that should be familiar:

$$E = mc^2. \quad (9)$$

This rough derivation provides a little insight to the power and purpose of using four-momentum. We will use this notation extensively throughout the rest of this work.

The other useful notation to understand is called natural units, where $c = \hbar = 1$. Under these units, Eq. 7 becomes

$$E^2 = p^2 + m^2. \quad (10)$$

While this offers much in the way of simplicity when working with complex equations, the disadvantage is that we lose information regarding dimensional analysis of the equation. Nevertheless, for the most part, we will use natural units in this work.

Consider an electron with four-momentum k scattering off of a nucleon with momentum p . The Feynman diagram for such an interaction is in Fig. 3, where k' and

p' are the final momentum of the scattered electron and nucleon respectively. Here, q is the momentum of the virtual photon⁴ (typically denoted by γ^*) that mediates the interaction. That virtual photon momentum, $q = k' - k$, is the momentum lost by the scattered electron.

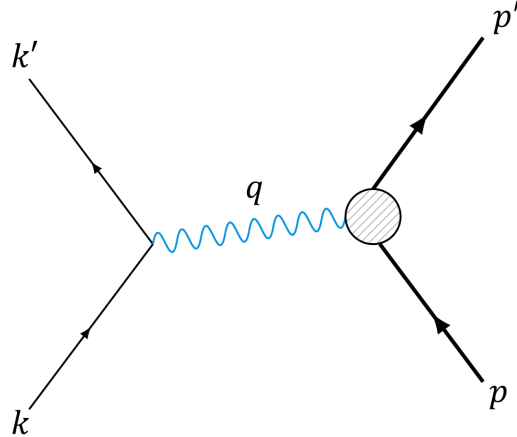


Fig. 3: Feynman diagram of an electron scattering from a nucleon.

There are some other important quantities to consider for electron scattering. The first is the square of that four-momentum transfer

$$q^2 = (k' - k)^2 = 2m_e^2 - 2(EE' - |\mathbf{p}||\mathbf{p}'| \cos \theta), \quad (11)$$

where m_e is the mass of the electron, E is the energy of the incident electron, E' is the energy of the scattered electron, $|\mathbf{p}|$ is the magnitude of the three-momentum of the incident nucleon, $|\mathbf{p}'|$ is the magnitude of the scattered nucleon's three-momentum, and θ is the scattering angle of the electron. When we use the trigonometric identity $1 - \cos \theta = 2 \sin^2 \frac{\theta}{2}$ and take the electron mass to be zero (*i.e.* $|\mathbf{p}| = E$), we get

$$q^2 \approx -4EE' \sin^2 \frac{\theta}{2}. \quad (12)$$

As a convention to make the quantity positive, we use $Q^2 = -q^2$, which will be used throughout the rest of this work. Another variable we need in order to analyze these electron scattering kinematics is the variable ν , which is the energy transfer of the electron to the nucleon via γ^* (*i.e.* the virtual photon) and is defined by

$$\nu = \frac{\mathbf{p} \cdot \mathbf{q}}{M}. \quad (13)$$

⁴The term “virtual” here may be misleading. It does not imply that the photon does not really exist. It refers to the short-lived exchange of the electromagnetic force.

Here, p is the four-momentum of the incident nucleon and M is the nucleon mass. In the laboratory frame, the nucleon is at rest (*i.e.* $p = (M, \mathbf{0})$),⁵ and $q = (E - E', \mathbf{q})$, so the energy transferred by the virtual photon to the nucleon in the laboratory frame would be

$$\nu = E - E'. \quad (14)$$

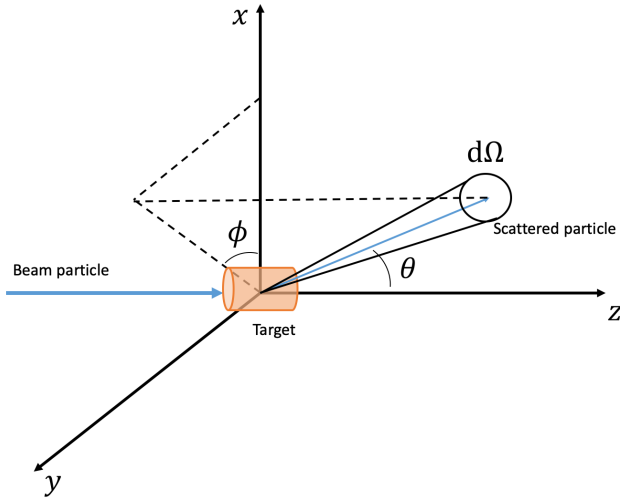


Fig. 4: Scattering process on a quasi-static differential cross section.

Whenever we deal with collisions of particles, there is a probability associated with the reaction between that projectile and target depicted in Fig. 4. That probability is called the *cross section* and with it often comes a wealth of knowledge about the dynamics of the interaction itself. In many reactions we deal with what is known as the *differential cross section*, which reflects the fact that the probability of a reaction depends on the spatial or kinematic quantities. This differential cross section is the probability of particles scattered into a bit of the solid angle $d\Omega$. Mathematically, the differential cross section for a spinless particle scattered from a static point charge can be written [7] as

$$\frac{d\sigma}{d\Omega} = \frac{\alpha^2}{4E^2 \sin^4 \frac{\theta}{2}}, \quad (15)$$

where α is known as the fine-structure constant equal to $e^2/4\pi \approx 1/137$, E is the energy of the incident electron, and θ is the scattering angle of the electron in the laboratory frame. Eq. 15 is known as the Rutherford Formula and is the simplest

⁵Just like other three-dimensional vectors, when bolded, $\mathbf{0}$ represents $(0,0,0)$.

theoretical scattering case. If we include the electron spin, we get

$$\frac{d\sigma}{d\Omega} = \frac{\alpha^2 \cos^2 \frac{\theta}{2}}{4E^2 \sin^4 \frac{\theta}{2}}, \quad (16)$$

which is known at the *Mott* cross section (we will from now on denote this particular cross section by $(\frac{d\sigma}{d\Omega})_{\text{Mott}}$). If we next introduce the mass of the point-like target M , that target particle will recoil, and so we get a scattered electron energy of

$$E' = \frac{E}{1 + \frac{2E}{M} \sin^2 \frac{\theta}{2}}, \quad (17)$$

and the cross section becomes

$$\begin{aligned} \frac{d\sigma}{d\Omega} &= \frac{\alpha^2 \cos^2 \frac{\theta}{2}}{4E^2 \sin^4 \frac{\theta}{2}} \cdot \frac{E'}{E} \left[1 - \frac{q^2}{2M^2} \tan^2 \frac{\theta}{2} \right] \\ &= (\frac{d\sigma}{d\Omega})_{\text{Mott}} \cdot \frac{E'}{E} \left[1 - \frac{q^2}{2M^2} \tan^2 \frac{\theta}{2} \right]. \end{aligned} \quad (18)$$

As that target mass M increases, this equation reduces to the Mott cross section.

We are beginning to approach a more realistic mathematical description of scattering, so we must discuss the various types that exist. In Fig. 3 if both particles remain intact in their ground state after the collision, it is called *elastic scattering*. Like pool balls, they essentially bounce off each other, of course through the exchange of that virtual photon. Inelastic scattering is when an internal excitation occurs in one or both particles. We need to understand these types of scattering in more depth to understand the BONuS12 experiment.

2.3 ELASTIC SCATTERING

When the momentum transfer, or more specifically Q^2 , is low, there is a higher probability that the lepton (at JLab, that lepton is an electron) essentially bounces off of the target particle (typically a nucleon) in what is known as elastic scattering. Whatever momentum is transferred does not force the nucleon into excited states (called resonances) or break it apart entirely (deep inelastic scattering). In a situation like Fig. 3 when scattering elastically

$$k + p \longrightarrow k' + p'. \quad (19)$$

Here k and p are the incident electron and nucleon four-momenta respectively, and k' and p' are the scattered electron and nucleon respectively. In this elastic case,

$$M_N = M'_N \quad \text{and} \quad m_e = m'_e \quad (20)$$

where M_N is the mass of the nucleon and m_e is the mass of the electron.

Because the nucleon target not point-like, we cannot simply use the Mott Equation (Eq. 16) to calculate the cross section of this elastic-scattering process. If we scatter electrons from some particle with a charge distribution $\rho(r)$ (r distance away from the charge source), like a proton, the scattering amplitude (following [8]) is modified by a form factor

$$F(q^2) = \int d^3r e^{i\mathbf{q}\cdot\mathbf{r}} \rho(r). \quad (21)$$

This particular form factor in Eq. 21 is an integral over volume of that charge distribution times the plane-wave representation of the particle. $F(q^2)$ is the Fourier transform of the charge distribution. As the name suggests this form factor provides insight into the composite structure of that particle. When this form factor is squared, it serves as a multiplier to the Mott cross section, giving us an expression for the elastic scattering cross section

$$\frac{d\sigma}{d\Omega} = \left(\frac{d\sigma}{d\Omega} \right)_{\text{Mott}} [F(q^2)]^2. \quad (22)$$

This gives us a useful description of elastic electron-proton scattering.

The last thing to do regarding the elastic scattering cross section is to expand the expression into the kinematic variables we can measure. We accomplish this by defining a scattering probability amplitude \mathcal{M} such that in the lab frame

$$\frac{d\sigma}{d\Omega} = \frac{1}{64\pi^2} \left(\frac{1}{M_p + 2E \sin^2 \frac{\theta}{2}} \right)^2 |\mathcal{M}_{fi}|^2, \quad (23)$$

where we neglect the small electron mass, M_p is the mass of the proton, E is the incident electron energy, and θ is the scattering angle of the electron in the lab frame. The term $|\mathcal{M}_{fi}|^2$ is shorthand for

$$|\mathcal{M}_{fi}|^2 = |\langle f | \mathcal{M} | i \rangle|^2, \quad (24)$$

where \mathcal{M} is the scattering probability amplitude. If the polarizations are not observed, this must be averaged over initial spin states and summed over the final spin states of $|\mathcal{M}|^2$. Mathematically, using s and S for initial spin states of the electron and proton respectively and s' and S' for final spin states, it can be expressed as

$$|\mathcal{M}_{fi}|^2 = \frac{1}{2} \frac{1}{2} \sum_{s,S} \sum_{s',S'} |\mathcal{M}|^2. \quad (25)$$

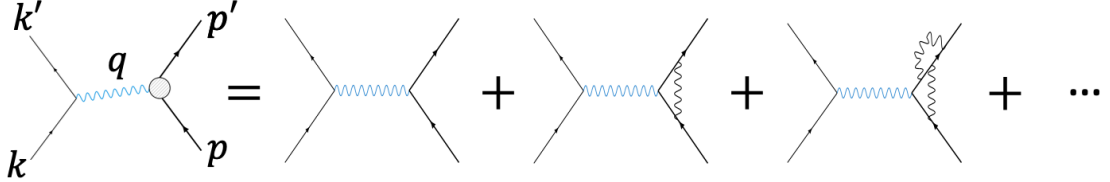


Fig. 5: The contributions of higher order diagrams.

The scattering probability amplitude cannot be known exactly because of the processes beyond the first order (tree level) that could occur in Fig. 3 at the proton- γ^* vertex blob (these contributions can be seen in Fig. 5). However, we can handle the mathematical description of these processes by expressing the scattering probability amplitude matrix in terms of the leptonic and hadronic tensors

$$|\mathcal{M}|^2 = \frac{e^4}{Q^4} \ell_{\mu\nu} W^{\mu\nu}. \quad (26)$$

The leptonic tensor $\ell_{\mu\nu}$ is associated with the coupling of the virtual photon to the electron (more generally the coupling of the exchange boson to the lepton), and for unpolarized scattering can be expressed as

$$\ell_{\mu\nu} = \bar{u}(k', s') \gamma^\mu u(k, s) \bar{u}(k, s) \gamma^\nu u(k', s'). \quad (27)$$

The term $u(k)$ is the Dirac spinor. For the electron (a spin-1/2 fermion), there are two spin states (*i.e.* up or down) so there are two associated spinors that could exist here

$$u_\uparrow(k) = \begin{pmatrix} 1 \\ 0 \\ \frac{k_z}{E+m} \\ \frac{k_x+ik_y}{E+m} \end{pmatrix} \text{ and } u_\downarrow(k) = \begin{pmatrix} 0 \\ 1 \\ \frac{k_x-ik_y}{E+m} \\ \frac{-k_z}{E+m} \end{pmatrix}, \quad (28)$$

where m is the lepton mass, $k_{x,y,z}$ are the momentum components of the initial lepton. In Eq. 27, γ^μ are the gamma matrices. When summed and averaged over spins, the leptonic tensor (following [9]) becomes

$$\begin{aligned} \ell_{\mu\nu} &= \text{Tr} \left[\frac{\not{k}' + m}{2m} \gamma^\mu \frac{\not{k} + m}{2m} \gamma^\nu \right] \\ &= \frac{1}{m^2} \text{Tr}(\not{k}' \gamma^\mu \not{k} \gamma^\nu + m^2 \gamma^\mu \gamma^\nu) \\ &= 2(k'^\mu k^\nu + k^\mu k'^\nu - g^{\mu\nu} k' \cdot k). \end{aligned} \quad (29)$$

Thus far we have from Eq. 26

$$|\mathcal{M}|^2 = \frac{e^4}{Q^4} 2(k'^\mu k^\nu + k^\mu k'^\nu - g^{\mu\nu} k' \cdot k) W^{\mu\nu}, \quad (30)$$

where $g^{\mu\nu}$ is the metric tensor.

We must now take a look at the hadronic tensor $W^{\mu\nu}$, which is more complicated because we must take into account the proton's structure. In fact, the hadronic tensor cannot be known exactly. It can, however, be expanded to the second order as

$$W^{\mu\nu} = \langle p | J^\nu | p' \rangle \langle p' | J^\mu | p \rangle, \quad (31)$$

which depends on the J^μ current matrix elements. That current between two nucleon states (following [8])

$$\langle p | J^\mu(0) | p' \rangle = \bar{U}(p') \left[F_1(Q^2) \gamma^\mu + F_2(Q^2) \frac{i\sigma^{\mu\nu}}{2M_N} \right] U(p) \quad (32)$$

gives rise to two form factors, $F_1(Q^2)$ which is called the Dirac form factor and $F_2(Q^2)$ called the Pauli form factor. Here $\sigma^{\mu\nu} = \frac{i}{2}[\gamma^\mu, \gamma^\nu]$ and we denote the difference between the lower-case $u(k, s)$ electron spinors from Eq. 27 and upper-case $U(p)$ nucleon spinors. If we introduce the more physically interesting Sach's electric and magnetic form factors respectively

$$G_E(Q^2) = F_1(Q^2) + \frac{Q^2}{4M_N^2} F_2(Q^2),$$

$$G_M(Q^2) = F_1(Q^2) + F_2(Q^2),$$

then the hadronic tensor can be written as

$$\begin{aligned} W^{\mu\nu} &= 2(p'^\mu p^\nu + p'^\nu p^\mu - g^{\mu\nu}(pp' - M_N^2)) G_M^2 \\ &\quad - 2F_2 G_M (p + p')^\mu (p + p')^\nu + F_2^2 \frac{M_N^2 + p \cdot p'}{2M_N^2} (p + p')^\mu (p + p')^\nu \\ &= (-q^\mu q^\nu + g^{\mu\nu} q^2) G_M^2 + (p + p')^\mu (p + p')^\nu \frac{G_E^2 + \tau G_M^2}{1 + \tau} \\ &= g^{\mu\nu} q^2 G_M^2 + 4p^\mu p^\nu \frac{G_E^2 + \tau G_M^2}{1 + \tau} + \dots, \end{aligned} \quad (33)$$

where we define $\tau = Q^2/4M_N^2$ to simplify the expression. Because of current conservation, the terms containing factors of q^μ are replaced with the ellipses, since they do not contribute to the cross section.

Substituting our expressions for the leptonic and hadronic tensors for elastic scattering in the lab frame and contracting them, we arrive at

$$\frac{d\sigma}{d\Omega} = \left(\frac{d\sigma}{d\Omega} \right)_{\text{Mott}} f_{\text{rec}} \left[\frac{G_E^2(Q^2) + \tau G_M^2(Q^2)}{1 + \tau} + 2\tau G_M^2 \tan \frac{\theta}{2} \right], \quad (34)$$

where $\left(\frac{d\sigma}{d\Omega} \right)_{\text{Mott}}$ comes from Eq. 16 (*i.e.* the Mott cross section) and f_{rec} is the recoil factor equal here to E'/E . As Q^2 gets very high, τ increases and the magnetic form factor $G_M(Q^2)$ dominates. Eq. 34 gives a more physical description of the elastic scattering cross section in terms of kinematic variables that can be measured through scattering experiments.

One more kinematic variable that needs to be introduced offers insight into cases when scattering enters into inelastic regimes. The invariant mass squared W^2 (not to be confused with the hadronic tensor $W^{\mu\nu}$) of the photon-nucleon system, is defined mathematically as

$$W^2 = (q + p)^2 = M_N^2 + 2M_N\nu - Q^2, \quad (35)$$

where $\nu = E - E'$ is the energy transferred from the electron to the nucleon via virtual photon (γ^*). In the elastic scattering case, $W^2 = M_N^2$, because Q^2 and thus ν are small (*i.e.* $E \ll M_N$). As Q^2 increases, instead of simply bouncing off of the nucleon, the energy transferred to the nucleon begins changing the state of the quarks within the nucleon.

2.4 RESONANCE REGION

Changing the state of a quark within the nucleon results in excited states of that nucleon, called *resonances*. The region where resonances occur is $M_N^2 < W^2 < 4 \text{ GeV}^2$, and is called the *resonance region*. There are 6 families of resonances that depend on the characteristics of the resonant particles. Particles containing only u and d quarks, whose isospin $I = \frac{1}{2}$, are denoted by N . The Δ family of resonances also have only u and d quarks, but have $\frac{3}{2}$ isospin. When $I = 0$ and the particle contains u , d and one c , s , or b quark, it is called a Λ resonance. The Σ resonance also has u , d plus one c , s , or b quark, but with $I = 1$. When only one u or d quark exists with two c , s , or b quarks with $I = \frac{1}{2}$, it is a Ξ resonance. Finally, when $I = 0$ and only c , s , or b quarks are present, it is known as an Ω resonance. [10]

Unlike the ground state of nucleons, these excited states are extremely short lived (on the order of 10^{-23} seconds). After their short life, these resonances decay into

more stable hadrons. Detection of these hadrons is what provides proof of the existence of resonant states. For example, a common resonance $\Delta^0(1232)$, which is the lowest lying resonance with a mass of 1.232 GeV [10], predominately decays via the strong interaction into a pion (π^0) and a neutron (n) or to $\pi^- p$. The entire interaction begins at the first step of creating an excited state

$$p + e^- \longrightarrow \Delta^0 + e' \quad (36)$$

then decays into

$$\Delta^0 \longrightarrow \pi^0 + n,$$

or

$$\Delta^0 \longrightarrow \pi^- + p. \quad (37)$$

However, because these resonances are so short-lived, it is convention to express the entire interaction as

$$p + e^- \longrightarrow e'^- + \pi^0 + n,$$

or

$$p + e^- \longrightarrow e'^- + \pi^- + p. \quad (38)$$

One reason for this convention is that there are many resonances that can produce the same final state (*i.e.* π^0 and n or π^- and p in our example). Knowing exactly what resonance produced a particular final state can be difficult. In the example of Eq. 38, the Δ^0 has the same quark makeup as the neutron (*i.e.* udd), but is much heavier. Measuring the invariant mass of the resulting particles is one of the few ways to understand what resonance occurred.

Similar to elastic scattering, interactions with resonances can be described using form factors. The analogous differential cross section (following the treatment of [11]) is

$$\frac{d\sigma}{d\Omega} = \left(\frac{d\sigma}{d\Omega} \right)_{\text{Mott}} f_{\text{rec}} \left(\frac{|G_E|^2 + \tau^* |G_T|^2}{1 + \tau^*} + 2\tau^* |G_T|^2 \tan^2 \frac{\theta}{2} \right) R(W), \quad (39)$$

where f_{rec} is the recoil factor of the proton, τ^* is the analogous kinematic quantity of τ from elastic scattering, G_E and G_T are the resonance longitudinal and transverse form-factors respectively, and $R(W)$ is called the resonance line shape. In inelastic scattering of resonances

$$f_{\text{rec}} = \frac{E'}{E} \left[\frac{1}{1 - \frac{(W_R^2 - M_N^2)}{2M_N E}} \right], \quad (40)$$

and

$$R(W) = \frac{2\pi^{-1}W_R M_N \Gamma_R}{(W^2 - W_R^2)^2 + W_R^2 \Gamma_R^2}. \quad (41)$$

The quantities W_R and Γ_R refer to the resonance mass and width respectively. If the resonance width is small enough (*i.e.* when $W_R = M_N$ and $W_R \Gamma_R \rightarrow 0$), $R(W)$ becomes a δ -function and the resonance cross section reduces to that of an elastic cross section.

At low Q^2 , we can describe interactions by constituent quark models. At high Q^2 we enter a region best described with perturbative quantum chromodynamics (pQCD). We will discuss more about pQCD in a later section. The resonance region is an important bridge between elastic and deep inelastic scattering regimes. Determining resonance form factors allows us to describe the resonance transition the same way elastic form factors describe elastic interactions.

2.5 DEEP INELASTIC SCATTERING

Once the energy transferred to the nucleon (Q^2) becomes large enough, the probability of the virtual photon “elastically” scattering off a quark inside the nucleon increases. This is known as *deep* inelastic scattering. This happens at roughly $W > 2$ GeV and $Q^2 > 1$ GeV 2 . In this regime we can probe the inner structure of the nucleon.

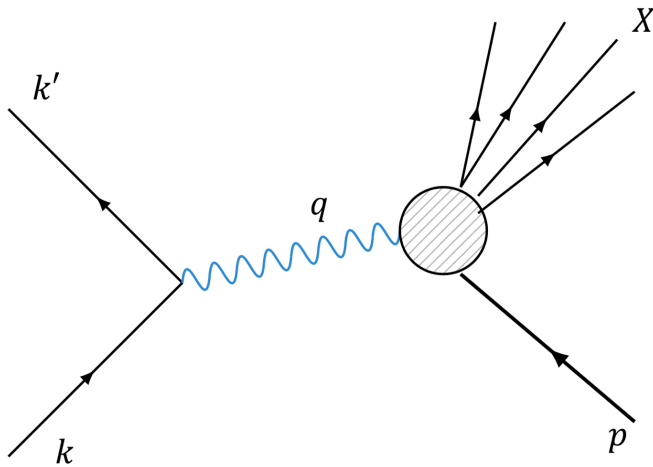


Fig. 6: Feynman diagram of deep inelastic electron scattering from a proton.

However, because the energy transfer is so high, the proton often breaks apart in the interaction

$$ep \longrightarrow e'X, \quad (42)$$

where X denotes all possible particles that might emerge from the proton-electron collision. The Feynman diagram must also be altered from Fig. 3 to Fig. 6, where X again represents all possible emerging particles. The deep-inelastic scattering cross section can be written (following [8]) as

$$\frac{d^2\sigma}{dE'\Omega} = \frac{4\alpha^2 E'^2}{q^4} \left[W_2(\nu, Q^2) \cos^2 \frac{\theta}{2} + 2W_1(\nu, Q^2) \sin^2 \frac{\theta}{2} \right], \quad (43)$$

where W_1 and W_2 are called inelastic structure functions. These structure functions are the analogs to the form factors in Eq. 34 for elastic scattering. There is much more to discuss about deep-inelastic scattering, but first we must discuss how to treat scattering off quarks (or more broadly, partons) within a nucleon with an approach called *scaling*.

2.6 PARTONS AND BJORKEN-SCALING

The way we probe inside nucleons is with the exchange of small wavelength (large Q^2) virtual photons, which interacts with partons inside the nucleon. This can be handled using the inelastic structure functions W_1 and W_2 , which are functions of the energy lost by the electron due to nucleon recoil (*i.e.* ν) and the negative four-momentum squared of the virtual photon (*i.e.* Q^2). When the virtual photon has a small enough wavelength (large enough Q^2), the nucleon that was once described by Eq. 34 starts to look more like a free Dirac particle and the cross section (following [8]) becomes

$$\frac{d\sigma}{dE'd\Omega} = \frac{4\alpha^2 e_q^2 E'^2}{q^4} \left(\cos^2 \frac{\theta}{2} - \frac{q^2}{2m^2} \sin^2 \frac{\theta}{2} \right) \delta \left(\nu + \frac{q^2}{2m} \right). \quad (44)$$

Remarkably, this is the equation for the electron elastic scattering cross section from a structureless particle.[8] Here e_q is the fractional charge of that structureless parton and m is that parton's mass. This parton inside the nucleon of concern here is the quark.

In this case, where the virtual photon elastically scatters off of a quark within the nucleon described by Eq. 44, the nucleon structure functions become

$$2W_1^{\text{point}} = \frac{Q^2}{2m^2} \delta \left(\nu - \frac{Q^2}{2m} \right) \quad (45)$$

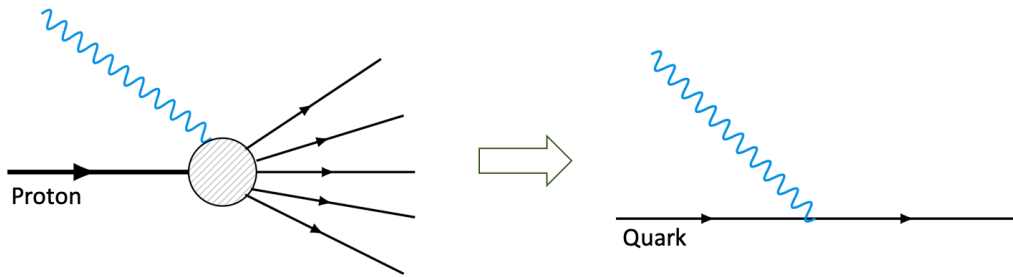


Fig. 7: The transition from inelastic scattering to deep inelastic scattering of a virtual photon and the quark within a nucleon.

and

$$W_2^{\text{point}} = \delta \left(\nu - \frac{Q^2}{2m} \right). \quad (46)$$

Here, thus in Eq. 44, there exists the delta function that conserves energy in the interaction. Fig. 7 shows the resulting diagram when we take the right side of Fig. 6 (the left side of Fig. 7) and begin to probe a single quark inside the nucleon (the right side of Fig. 7). This reduction is representative of the electron elastically scattering off a quark in the nucleon.

If we take Eq. 45 and 46, using the identity $\delta(x/a) = a\delta(x)$, we can write

$$\begin{aligned} 2mW_1^{\text{point}}(\nu, Q^2) &= \frac{Q^2}{2m\nu} \delta \left(1 - \frac{Q^2}{2m\nu} \right) \\ \nu W_2^{\text{point}}(\nu, Q^2) &= \delta \left(1 - \frac{Q^2}{2m\nu} \right). \end{aligned} \quad (47)$$

These equations for the structure functions are now dimensionless and depend on only the ratio $Q^2/2m\nu$, which is both important and useful. That usefulness is as follows: when Q^2 is high enough, the virtual photon begins to elastically scatter off of structureless (point) particles within the nucleon and can be described using the dimensionless structure functions

$$MW_1(\nu, Q^2) \xrightarrow[\text{large } Q^2]{} F_1(x_B)$$

$$\nu W_2(\nu, Q^2) \xrightarrow[\text{large } Q^2]{} F_2(x_B). \quad (48)$$

Here x_B is introduced as the Bjorken- x scaling variable defined as

$$x_B = \frac{Q^2}{2M\nu}, \quad (49)$$

which describes the momentum fraction of a quark or gluon within a nucleon. M is the nucleons mass. Up to this point, we have only discussed interactions between the virtual photon and the quarks within the nucleon, but that virtual photon can also interact with gluons that exists in the nucleon. Collectively, these quarks and gluons in the nucleon are known as partons. The Bjorken- x scaling variable can describe the momentum fraction of any parton within a nucleon.

The relationship between the structure functions $F_1(x_B)$ and $F_2(x_B)$ (known as the Callan-Gross relation) is

$$2x_B F_1(x_B) = F_2(x_B) = \sum_i e_i^2 f_i(x_B). \quad (50)$$

In the right side of this expression we have a sum over partons (the parton index is i) of the square of that parton's charge (e_i^2) times $f_i(x_B)$, known at the parton distribution function. The parton distribution function (or PDF)

$$f_i(x_B) = \frac{dP_i}{dx_B}, \quad (51)$$

describes the probability P_i that a struck parton i carries a fraction (x_B) of the nucleon's momentum.

Because $F_2(x_B)$ offers a straightforward interpretation in terms of quarks, the F_2 structure function is the more important term here to examine experimentally and is of interest in the BONuS12 experiment. For deep-inelastic electron-proton scattering, the $F_2^p(x_B)$ structure function is

$$\frac{1}{x_B} F_2^p(x_B) = \left(\frac{2}{3}\right)^2 [u^p(x_B) + \bar{u}^p(x_B)] + \left(\frac{1}{3}\right)^2 [d^p(x_B) + \bar{d}^p(x_B)] \quad (52)$$

$$+ \left(\frac{1}{3}\right)^2 [s^p(x_B) + \bar{s}^p(x_B)], \quad (53)$$

where p superscript denotes that we are dealing with the proton structure, and the PDF $f_i(x_B)$ is replaced with the first letter of the parton name (*e.g.* the up quark and antiquark PDF's are denoted as $u^p(x_B)$ and $\bar{u}^p(x_B)$ respectively). The contributions of quarks heavier than the strange quark have been assumed to be negligible here.

The neutron structure function $F_2^n(x)$, where we have dropped the B in x_B , is

$$\frac{1}{x} F_2^n(x) = \left(\frac{2}{3}\right)^2 [u^n(x) + \bar{u}^n(x)] + \left(\frac{1}{3}\right)^2 [d^n(x) + \bar{d}^n(x)] \quad (54)$$

$$+ \left(\frac{1}{3}\right)^2 [s^n(x) + \bar{s}^n(x)]. \quad (55)$$

This looks similar to the F_2^p structure function because the proton and neutron are together part of an isospin doublet. When particles are members of an isospin doublet, they can transform into each other under an $SU(2)$ transformation

$$\binom{p}{n} \xrightarrow{SU(2)} \exp\left(-\frac{i}{2}\theta_a \sigma_a\right) \binom{n}{p},$$

where p and n are proton and neutron states, and σ_a are the Pauli matrices. This transformation means that the quark contents of the proton and neutron are related.

2.7 NUCLEON STRUCTURE-FUNCTION RATIO F_N^2/F_P^2

We can exploit this relation between quark contents of protons and neutrons to study the structure of nucleons, in particular the neutron structure. That relationship between quark contents means

$$\begin{aligned} u^p(x) &= d^n(x) \equiv u(x), \\ d^p(x) &= u^n(x) \equiv d(x), \\ s^p(x) &= s^n(x) \equiv s(x). \end{aligned} \quad (56)$$

The probability of finding a u quark in a proton is the same as the probability of finding a d quark in a neutron. Each nucleon consists not only of u_v and d_v quarks that determine the quantum numbers of the nucleon (called *valence* quarks, hence the subscript v), but many quark-antiquark pairs in a constant state of creation and annihilation (known as *sea* quarks). In the first order approximation, we can assume that the lighter quark-antiquark pairs $u_s\bar{u}_s$, $d_s\bar{d}_s$, and $s_s\bar{s}_s$ contribute to this “sea” and we can neglect contributions from the heavier quark-antiquark pairs $c_s\bar{c}_s$ and so on.

This approximation of the nucleon structure results in adding the sea quarks to the contributions of each quark type. That is

$$\begin{aligned} u(x) &= u_v(x) + u_s(x), \\ d(x) &= d_v(x) + d_s(x), \\ u_s(x) &= \bar{u}_s(x) = d_s(x) = \bar{d}_s(x) = s_s(x) = \bar{s}_s(x) = S(x), \end{aligned} \quad (57)$$

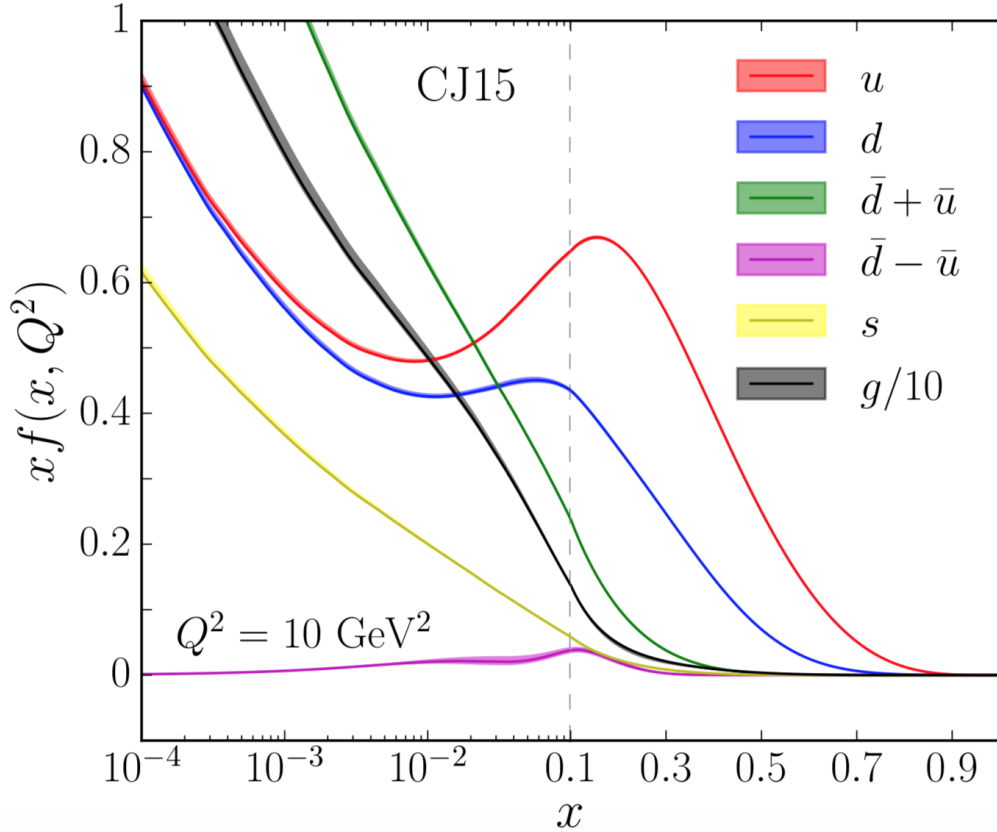


Fig. 8: Comparison of CJ15 PDFs $xf(x, Q^2)$ for different flavors ($f = u, d, \bar{d} + \bar{u}, \bar{d} - \bar{u}, s$ and $g/10$) at a scale $Q^2 = 10 \text{ GeV}^2$, with 90% CL uncertainty bands. Note the combined logarithmic/linear scale along the x-axis [12].

where we now use $S(x)$ for all sea quark contributions. If we combine this relationship with our expressions for the proton and neutron structure functions Eqs. 52 and 54, respectively, we get

$$\frac{1}{x} F_2^p = \frac{1}{9}[4u_v + d_v] + \frac{4}{3}S \quad (58)$$

and

$$\frac{1}{x} F_2^n = \frac{1}{9}[u_v + 4d_v] + \frac{4}{3}S, \quad (59)$$

where the $\frac{4}{3}$ comes from summing over all six sea quark distributions. In the low x limit (*i.e.* $x \rightarrow 0$), the ratio of F_n^2/F_2^p goes to unity, or

$$\frac{F_2^n}{F_2^p} \xrightarrow{x \rightarrow 0} 1. \quad (60)$$

However, as we approach $x \rightarrow 1$ that ratio becomes

$$\frac{F_2^n}{F_2^p} \xrightarrow{x \rightarrow 1} \frac{u + 4d}{4u + d}, \quad (61)$$

where u and d are the valance *up* and *down* quarks and $S \rightarrow 0$. We can see in Fig. 8 that as $x > 0.3$, the u and d quarks dominate, so Eq. 61 neglects the sea-quark contributions as well as *strange* and larger mass sea-quark contributions. We can rearrange Eq. 61 to get the d/u ratio

$$\frac{d}{u} \approx \frac{4F_2^n/F_2^p - 1}{4 - F_2^n/F_2^p}, \quad (62)$$

which provides important insight into the parameterizations of PDFs at large x .

2.8 MODELS AND PREDICTIONS

If SU(6) symmetry were exact, then the u and d quarks within the proton would be identical with the exceptions of charge and flavor. The wave function of a proton polarized in the $+z$ direction [13] would be

$$\begin{aligned} p \uparrow = & \frac{1}{2}u \uparrow (ud)_{S=0} + \frac{1}{\sqrt{18}}u \uparrow (ud)_{S=1} - \frac{1}{3}u \downarrow (ud)_{S=1} \\ & - \frac{1}{3}d \uparrow (uu)_{S=1} - \frac{\sqrt{2}}{3}d \downarrow (uu)_{S=1}, \end{aligned} \quad (63)$$

where the subscript are the spins of the diquark pairs. The quark distribution in this case would be the same for both u and d quarks, which implies $u = 2d$ for all x . This leads to the F_2 structure function and d/u ratios

$$\frac{F_2^n}{F_2^p} = \frac{2}{3}, \quad \frac{d}{u} = \frac{1}{2}. \quad (64)$$

This is known as the SU(6) quark model. This symmetry, however, is broken in nature as there is a nonzero difference between quark masses as well as a measured value of the F_2^n/F_2^p ratio far below $2/3$.

There are a few explanations out there for SU(6) symmetry breaking. Close [14] and Cartlitz [15] observed the correlation between large- x behavior of F_2^n/F_2^p and the mass splitting of the nucleon and Δ baryons. They assumed that the stuck nucleon breaks into a single quark which interacts with the virtual photon and a diquark pair. When $x \rightarrow 1$, the $S = 1$ state term becomes small compared to the $S = 0$ state term. This suppression of the $S = 1$ diquark state can explain the symmetry

breaking and leads to the first term in Eq. 63 to dominate. Therefore at $x \approx 1$, F_2^p is essentially given by the single u quark distribution and so

$$\frac{F_2^n}{F_2^p} = \frac{1}{4}, \quad \frac{d}{u} = 0. \quad (65)$$

Isgur [16] [17] describes this d -quark suppression by a color hyperfine interaction arising from a one-gluon exchange. In the lowest order, the Hamiltonian of the hyperfine-perturbed quark model for the color-magnetic hyperfine interaction between two quarks is proportional to $S_i \cdot S_j$, where S_i is the spin vector of quark i . This means that if the spins are parallel, the force is repulsive, and if the spins are anti-parallel then the force is attractive. Therefore, $S = 1$ is suppressed and $d/u = 0$ as $x \rightarrow 1$.

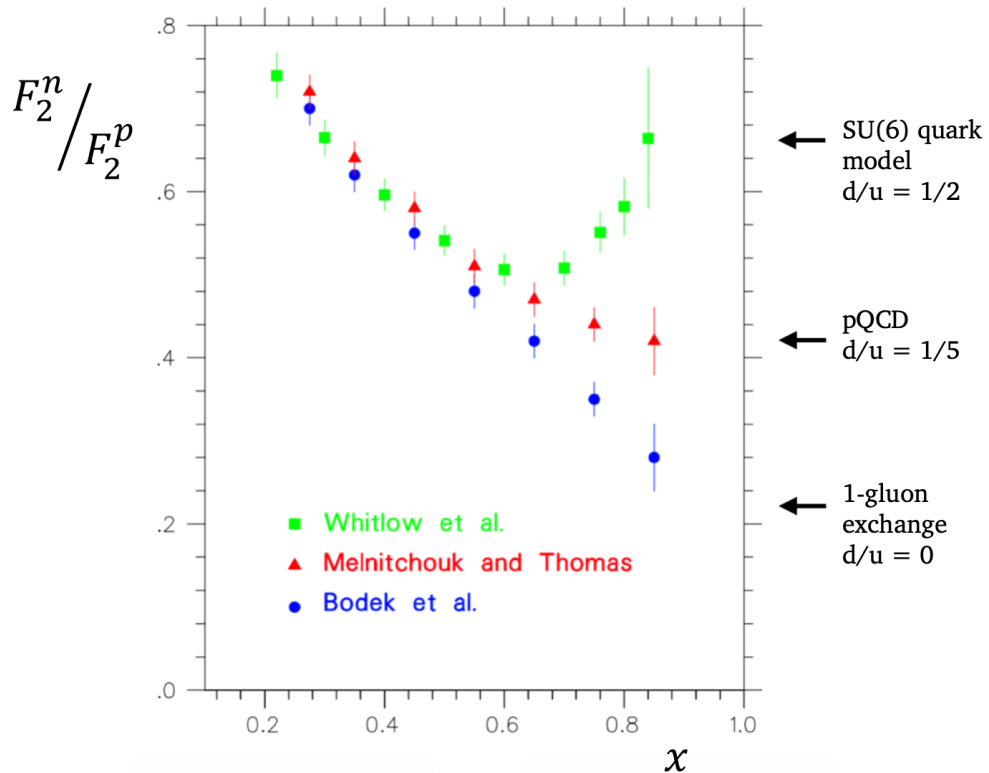


Fig. 9: Model dependence of F_2^n/F_2^p [18].

The last model that will be introduced here that proposed to explain the SU(6) symmetry breaking is based on perturbative QCD first from Farrar and Jackson.[19] They put forward that at $x \approx 1$, the hadronic structure functions could be calculated to the lowest order perturbation theory to $O(m^2/q^2)$, where the incoming quarks could be thought of as “free” partons. The valence quark wave function that

dominates here is the diquark spin projection $S_z = 0$. When the spins of two quarks are aligned, scattering is suppressed by a factor of $(1 - x)$ less than anti-aligned quarks. That is, $S_z = 0$ diquark states dominate when $x \rightarrow 1$. The u quark having the same helicity as the proton is 5 times as likely as the d having the same helicity as the proton. This results in

$$\frac{F_2^n}{F_2^p} = \frac{3}{7}, \quad \frac{d}{u} = \frac{1}{5}. \quad (66)$$

More recently, Brodsky [20] used a hard gluon exchange model based on quark counting rules leading to the same conclusion.

All of these predictions can be summarized in Fig. 9, which makes it obvious that the value of F_2^n/F_2^p is very much model dependent. It is the goal of the BONuS12 experiment to measure this ratio in a model independent way. In order to do this, we need to know the values of both F_2^p and F_2^n to high precision. Much is known about the F_2^p structure function because it can be extracted from electrons scattering from protons in hydrogen targets. Fig. 10 shows the multiple experiments and kinematic ranges where F_2^p has been measured. The trouble with Eq. 61 and Eq. 62 is our knowledge of the F_2^n structure function.

2.9 DIFFICULTIES IN EXTRACTING F_2^N/F_2^P FROM DEUTERIUM

There are no free neutron targets to conduct scattering experiments from like there is for protons in hydrogen targets. Therefore, the F_2^n structure function must be extracted from scattering experiments using targets like Helium-3 (two protons and a neutron), Helium-4 (two protons and two neutrons), and deuterium (one proton and one neutron). The BONuS12 experiment uses a deuterium target.

The trouble with using any nuclear target with two or more nucleons to study the structure of a single nucleon is that those nucleons do not behave as they do when they are free or alone in a nucleus. Early DIS experiments by the Electron Muon Collaboration (EMC) in CERN found that the ratio F_2^A/F_2^D (superscript A denotes the mass number of a nuclear target and D denotes deuterium) was not unity for all values of x . Fig. 11 shows that deviation for experiments done on iron and copper nuclei. This deviation indicates that quark distributions are different for free and bound nucleons.

Because the EMC first discovered this phenomena, the deviation between $0.2 < x < 0.8$ was dubbed the EMC effect. The other contributors are known as shadowing

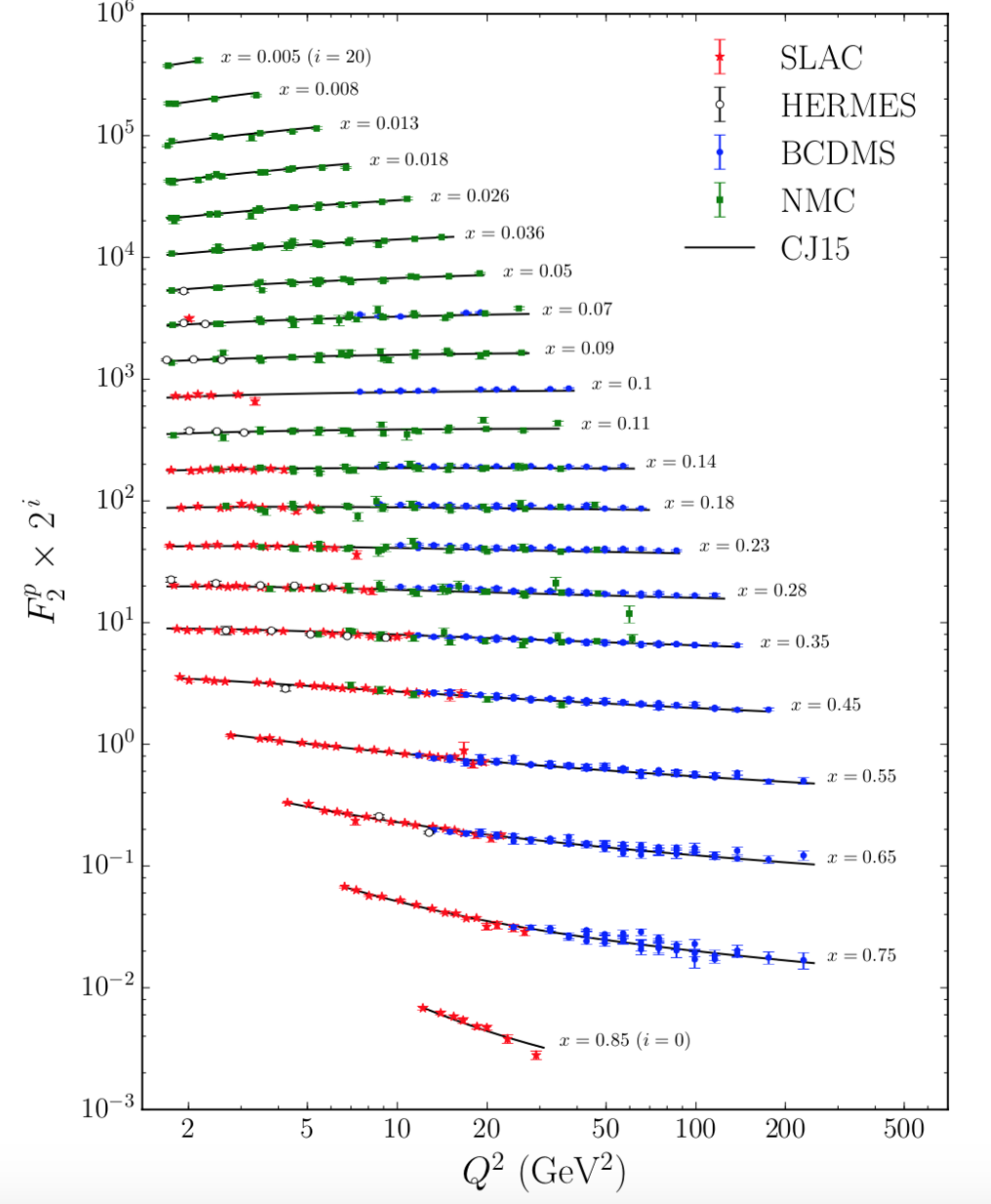


Fig. 10: Measured values of F_2^p vs Q^2 for different values of x [12].

($x < 0.1$), anti-shadowing ($0.1 < x < 0.2$) and $x > 0.8$ is believed to be due to Fermi motion. Just like partons in a nucleon, nucleons in a nucleus are not stationary. Fermi motion refers to the motion of nucleons within a nucleus.

There are many models attempting to explain the EMC effect (for a detailed review, see [23]), but none have been proven experimentally. The EMC effect is

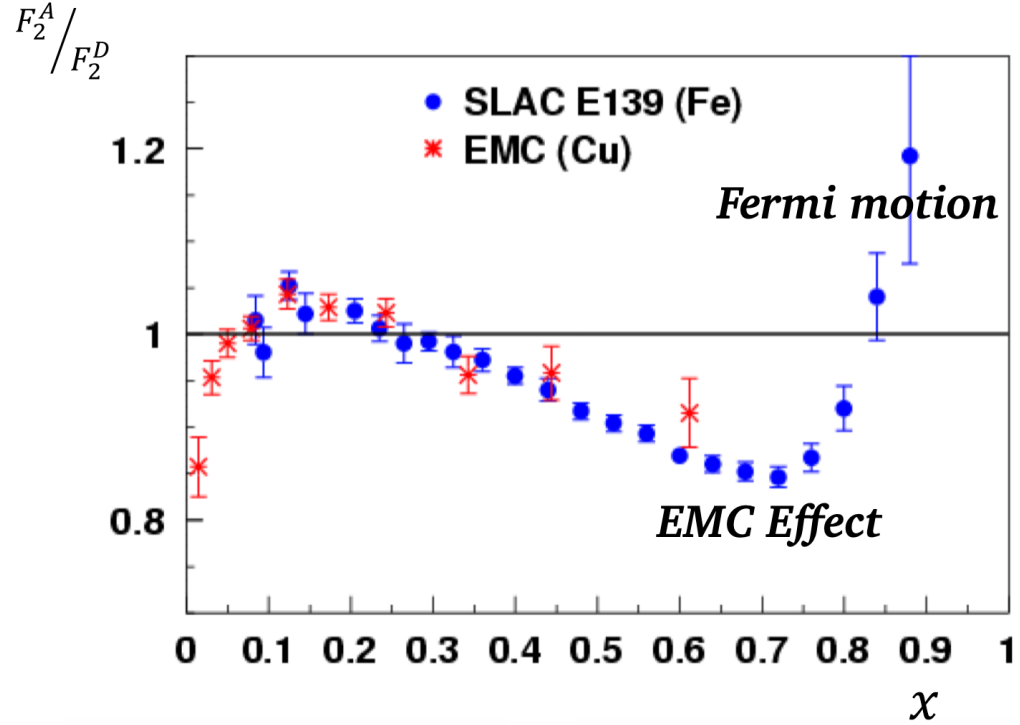


Fig. 11: Variations of the F_2^A/F_2^D ratio from unity indicating various nuclear binding effects [21][22].

not proportional to A (this was proven with scattering from ${}^4\text{He}$) or average nuclear density (ruled out by scattering from ${}^9\text{Be}$). However, a model of Q^2 rescaling pointed to increased quark confinement, which could explain the EMC effect.[23]

2.10 SPECTATOR TAGGING

The goal of the BONuS12 experiment and other experiments concerned with measuring the structure of neutrons is to do so without significant model dependence at high- x or involvement of bound-nucleon issues. To do this effectively, since the neutron of interest is bound within a nucleus, BONuS12 uses a method called spectator tagging. In particular, since the electron (e) is meant to scatter from the neutron within deuterium (D) in the interaction

$$eD \longrightarrow e' p_s X, \quad (67)$$

the proton (p_s) needs to be a spectator to the reaction. That is, the proton plays

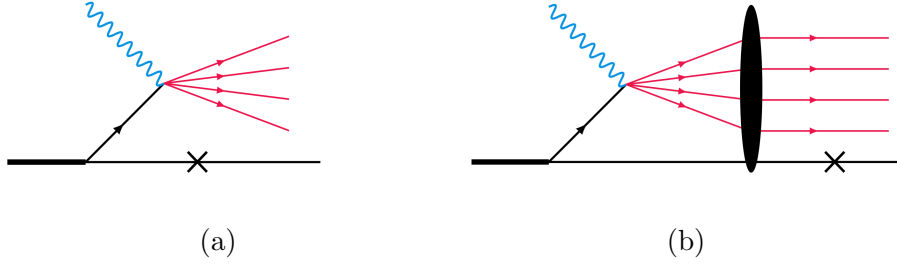


Fig. 12: Impulse approximation (a) and final state interaction diagrams (b).

no role in the interaction, thereby not interacting with any of the debris (X) coming from the struck neutron.

The differential cross section of the reaction given in Eq. 67 [24] is

$$\frac{d\sigma}{dx dQ^2 d^3 p_s / E_s} = \frac{4\pi\alpha_{em}^2}{x Q^4} \left(1 - y - \frac{x^2 y^2 M_N^2}{Q^2} \right) \times \left[F_L^D + \left(\frac{Q^2}{2q^2} + \tan^2 \frac{\theta}{2} \right) \frac{\nu}{M_N} F_T^D + \left(\frac{Q^2}{2q^2} + \tan^2 \frac{\theta}{2} \right)^{1/2} F_{TL}^D \cos \phi + F_{TT}^D \cos(2\phi) \right], \quad (68)$$

where α_{em} is the electromagnetic coupling constant, $y = \nu/E_e$, $\nu = E_e - E'_e$, M_N is the mass of the nucleon, ϕ is the azimuthal angle of the recoiling nucleon, and $F_{L,T,LT,TT}$ are nuclear structure functions. These structure functions depend on Q^2 , x , p_s^\perp , and $\alpha_s = \frac{E_s - p_s^z}{M_D}$, which is the light-cone momentum fraction of the deuteron carried by the spectator.

For practical considerations, one must integrate over ϕ to get (following [24])

$$\frac{d\sigma}{dx dQ^2 d^3 p_s / E_s} = \frac{4\pi\alpha_{em}^2}{x Q^4} \left(1 - y - \frac{x^2 y^2 M_N^2}{Q^2} \right) \left[F_{2D}^{SI} + 2 \tan^2 \left(\frac{\theta}{2} \right) \frac{\nu}{M_N} F_{1D}^{SI} \right], \quad (69)$$

where

$$F_{2D}^{SI}(x, Q^2, \alpha_s, p_s^\perp) = F_L^D + \frac{Q^2}{2q^2} \frac{\nu}{M_N} F_T^D \quad (70)$$

and

$$F_{1D}^{SI}(x, Q^2, \alpha_s, p_s^\perp) = \frac{F_T^D}{2}. \quad (71)$$

The assumption in Eq. 67 is that the reaction occurs when the momentum of the spectator proton is less than 700 MeV/c [24], where the virtual photon interacts with only one of the bound nucleons. Particles produced from the reaction can interact in the final state with the spectator nucleon. Two diagrams contribute to the cross

section: the impulse approximation when the particle debris from the struck nucleon does not interact with the other nucleon (Fig. 12a), and the case where rescattering occurs of the recoil nucleon with the other products of the deep inelastic scattering (DIS) interaction (Fig. 12b), called final-state interactions.

2.10.1 IMPULSE APPROXIMATION

The ideal interaction for studying the structure of the neutron in deuterium from DIS is the impulse approximation (IA). In the IA, the recoil nucleon is a spectator of the virtual photon γ^* scattering off the bound nucleon N . Using the Feynman rules, the IA amplitude is

$$A_{IA}^\mu = \langle X | J_{em}^\mu(Q^2, \nu, p_s) \frac{\not{p}_D - \not{p}_s + m}{M_N^2 - t} \bar{u}(p_s) \Gamma_D, \quad (72)$$

where $J_{em}^\mu(Q^2, \nu, p_s)$ represents the electromagnetic DIS operator of the electron scattering off the bound nucleon, $t = (p_D - p_s)^2$, and Γ_D is the covariant $D \rightarrow pn$ transition vertex.

If we take the recoil nucleon in Fig. 12a on the mass shell and using [24]

$$\not{p}_D - \not{p}_s + m \approx \sum_{\text{spins}} u(p_D - p_s) \bar{u}(p_D - p_s), \quad (73)$$

we can factorize Eq. 72 into two parts: (1) the DIS current of the bound nucleon $J_{X,N}^\mu = \langle X | J_{em}^\mu(Q^2, \nu, p_s) u(p_D - p_s)$, and (2) the wave function of the deuteron. This factorization provides us with nuclear DIS structure functions through convolution of bound nucleon structure functions (F_{1D}^{eff} and F_{2D}^{eff}) and the nuclear spectral function S , which (following [24]) are

$$\begin{aligned} F_{2D}^{SI}(x, Q^2, \alpha_s, p_s^\perp) &= \frac{S(\alpha_s, p_s^\perp)}{n} \frac{M_N \nu}{pq} \\ &\times \left[(1 + \cos \delta)^2 \left(\alpha + \frac{pq}{Q^2} \alpha_q \right)^2 + \frac{1}{2} \frac{(p_s^\perp)^2}{M_N^2} \sin^2 \delta \right] F_{2D}^{\text{eff}}(\tilde{x}, Q^2, \alpha_s, p_s^\perp), \\ F_{1D}^{SI}(x, Q^2, \alpha_s, p_s^\perp) &= \frac{S(\alpha_s, p_s^\perp)}{n} \left[F_{1D}^{\text{eff}}(\tilde{x}, Q^2, \alpha_s, p_s^\perp) + \frac{(p_s^\perp)^2}{2pq} F_{2D}^{\text{eff}}(\tilde{x}, Q^2, \alpha_s, p_s^\perp) \right], \end{aligned} \quad (74)$$

where $\sin^2 \delta = Q^2 / \mathbf{q}^2$. In the virtual-nucleon (VN) approximation $n = M_D / 2(M_D - E_s)$ and in the light-cone (LC) approximation $n = 2 - \alpha_s$. The modified Bjorken- x is given in the lab frame by

$$\tilde{x} \approx \frac{Q^2}{2M\nu(2 - \alpha)}. \quad (75)$$

The nuclear spectral function S gives us the probability of finding an interacting nucleon with momentum (α, p^\perp) in the target and a recoil nucleon with momentum (α_s, p_s^\perp) in the final state of the reaction. In the IA, $\alpha + \alpha_s = 2$ and $\mathbf{p}^\perp = -\mathbf{p}_s^\perp$. Putting this all together, we can use Eq. 74 in 68 to get

$$\begin{aligned} \frac{d\sigma}{dx dQ^2 d^3 p_s / E_s} = & \frac{4\pi\alpha_{em}^2}{x Q^4} \left(1 - y - \frac{x^2 y^2 M_N^2}{Q^2}\right) \frac{S(\alpha_s, p_s^\perp)}{n} \\ & \times \left(\frac{M_N \nu}{pq} \left[(1 + \cos \delta)^2 \left(\alpha + \frac{pq}{Q^2} \alpha_q \right)^2 + \frac{1}{2} \frac{(p_s^\perp)^2}{M_N^2} \sin^2 \delta \right] \right. \\ & \times F_{2D}^{\text{eff}}(\tilde{x}, Q^2, \alpha_s, p_s^\perp) + 2 \tan^2 \left(\frac{\theta}{2} \right) \frac{\nu}{M_N} \\ & \left. \times \left[F_{1D}^{\text{eff}}(\tilde{x}, Q^2, \alpha_s, p_s^\perp) + \frac{(p_s^\perp)^2}{2pq} F_{2D}^{\text{eff}}(\tilde{x}, Q^2, \alpha_s, p_s^\perp) \right] \right), \end{aligned} \quad (76)$$

where $\alpha_q = (\nu - |\mathbf{q}|)/M_N$.

2.10.2 MINIMIZING FINAL STATE INTERACTIONS

The IA is an ideal case, particularly for the BONuS12 experiment, where we desire no interaction between the spectator proton and the hadronic debris created from the γ^* -neutron interaction within the deuteron. We want to minimize any possibility of final state interactions to ensure that the proton we measure has not participated in the reaction.

For any process where final state interactions (FSI) may occur, like the BONuS12 experiment, it is important to understand and describe quantities relevant to the process. The central quantity describing FSI processes is the distorted momentum distribution [25]

$$n_D^{FSI}(\mathbf{p}_s, \mathbf{q}) = \frac{1}{3} \frac{1}{(2\pi)^3} \sum_{\mathcal{M}_D} \left| \int d\mathbf{r} \Psi_{1,\mathcal{M}_D}(\mathbf{r}) S(\mathbf{r}, \mathbf{q}) \chi_f^+ \exp(-i\mathbf{P}_s \mathbf{r}) \right|^2, \quad (77)$$

where ξ_f is the spin function of the spectator nucleon and $S(\mathbf{r}, \mathbf{q})$ is the S -matrix describing the FSI between the hadronic debris and the spectator. This S -matrix is

$$S(\mathbf{r}, \mathbf{q}) = 1 - \theta(z) \frac{\sigma_{\text{eff}}(z, Q^2, x)(1 - i\alpha)}{4\pi b_0^2} \exp\left(-\frac{b^2}{2b_0^2}\right), \quad (78)$$

where σ_{eff} is the time-dependent cross section and α is the ratio of real to imaginary part of the forward amplitude. When FSI do not occur $\sigma_{\text{eff}} = 0$, and the usual

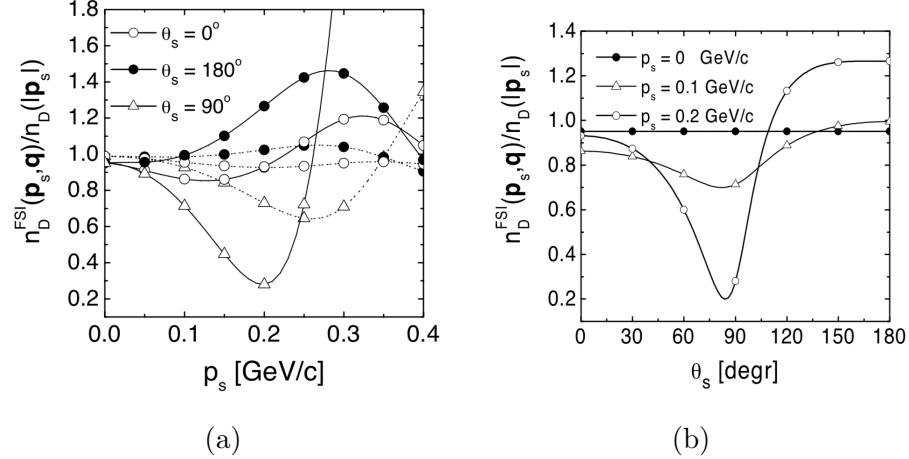


Fig. 13: (a) The Deep Inelastic Scattering ratio n_D^{FSI}/n_D (with n_D^{FSI} and n_D given by Eqs. 77 and 79, respectively), calculated *vs.* the momentum $p_s \equiv |\mathbf{p}_s|$ of the spectator nucleon emitted at different angles θ_s . The full lines correspond to the Q^2 - and z -dependent debris-nucleon effective cross section σ_{eff} , whereas the dashed lines correspond to a constant cross section $\sigma_{\text{eff}} = 20$ mb. (b) The Deep Inelastic Scattering ratio n_D^{FSI}/n_D (with n_D^{FSI} and n_D given by Eqs. 77 and 79, respectively) calculated *vs.* the emission angle θ_s of the spectator, for different values of the spectator momentum. Calculations were performed at $Q^2 = 5$ (GeV/c) 2 and $x = 0.2$ for the both graphs.

deuteron momentum distribution is recovered

$$n_D(|\mathbf{p}_s|) = \frac{1}{3(2\pi)^3} \sum_{\mathcal{M}_D} \left| \int d\mathbf{r} \Psi_{1,\mathcal{M}_D}(\mathbf{r}) \chi_f^+ \exp(-i\mathbf{P}_s \mathbf{r}) \right|^2. \quad (79)$$

To minimize any FSI that may occur in a process like Eq. 67, we look toward the ratio of the distorted n_D^{FSI} to deuteron n_D momentum distributions. When that ratio goes to unity, final state interactions do not exist. Fig. 13a shows that ratio as a function of the spectator proton momentum (p_s) for various angles (*i.e.* $\theta_s = 0^\circ$, 90° , and 180°). The solid lines correspond to Q^2 and z -dependent debris-nucleon effective cross section σ_{eff} , whereas the dashed lines are for the constant cross section $\sigma_{\text{eff}} = 20$ mb. From this we see that for momenta below 100 MeV/c, all lines begin to converge to unity.

The plot of the n_D^{FSI}/n_D ratio versus spectator proton scattering angle (θ_s) in Fig. 13b contains lines for three different values of spectator momenta (*i.e.* $p_s = 0$, 100,

200 MeV/c). This plot shows us that for momenta below 100 MeV/c, angles above 100° minimize FSI. Therefore, in order to minimize FSI in the semi-inclusive (*i.e.* detecting some, but not all, particles after the interaction) DIS reaction desired for the BONuS12 experiment, spectators protons with momenta below 100 MeV/c at angles above 100° are detected in coincidence with the scattered electron: $D(e, e', p_s)X$. This allows us to utilize the IA to extract the F_2^n structure function and thus the F_2^n/F_2^p structure function ratio.

CHAPTER 3

THE BONUS12 EXPERIMENT

The Barely Off-shell Nucleon Structure experiment at 12 GeV energy (BONuS12) used a electron scattering off a neutron in a deuterium target to detect low momentum (less than 100 MeV/c) backward-going (angles above 100°) spectator protons in a Radial Time Projection Chamber (RTPC). The spectator proton was detected in coincidence with the scattered electron in order to establish the semi-inclusive DIS interaction $D(e, e', p_s)X$ that BONuS12 will use to extract the structure function ratio F_2^n/F_2^p .

BONuS12 was conducted at the Thomas Jefferson National Laboratory (JLab) in Newport News, Virginia. JLab was founded in 1984 with the intent of studying the structure of nuclear matter. The unique accelerator that was built at JLab, called the Continuous Electron Beam Accelerator Facility (CEBAF), allowed for the realization of that intent by providing the ability to probe atomic nuclei at the quark level. In order to understand the BONuS12 experiment, we must first understand CEBAF and the Hall B spectrometer where the BONuS12 RTPC was installed. Then we will discuss the RTPC design, components, and construction.

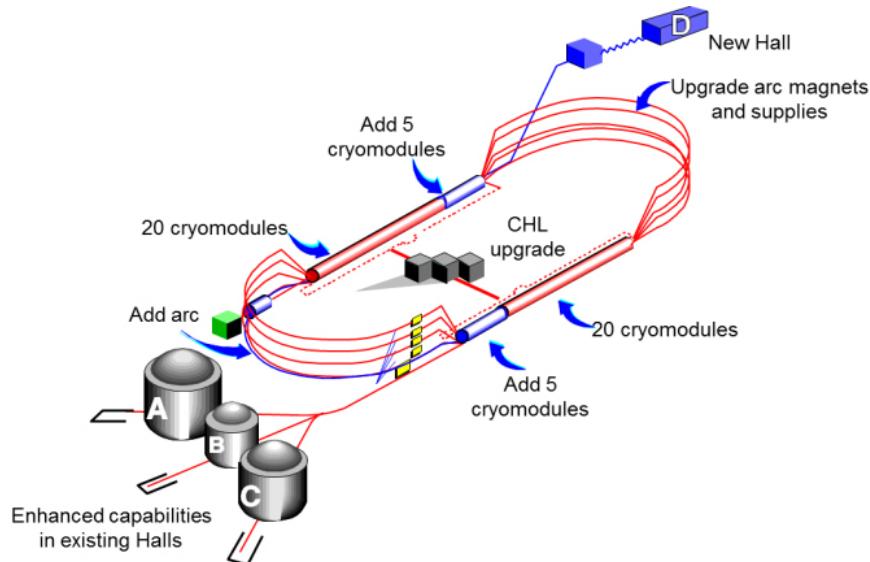


Fig. 14: CEBAF upgraded for the 12 GeV era [26].

3.1 CONTINUOUS ELECTRON BEAM ACCELERATOR FACILITY

The construction of the Continuous Electron Beam Accelerator Facility (CEBAF) was completed in 1994. It originally consisted of two antiparallel linear accelerators (LINACs) connected by nine recirculation arcs that accelerated electrons to an energy of 6 GeV at a current of up to 300 μ A. In 2004, JLab began an energy upgrade that would allow CEBAF to supply electrons up to 12 GeV. The same framework used for the 6 GeV accelerator was used for the 12 GeV era. That is, each pass around the accelerator increased the electron energy, which was 1-1.2 GeV/pass during the 6 GeV era [27] and 2.2 GeV/pass after the 12 GeV upgrade. Originally, that meant 5 passes would produce 6 GeV electrons before they were fed into the three existing experimental halls (*i.e.* Hall A, Hall B, and Hall C). In addition to the energy upgrade, a new experimental hall was built (*i.e.* Hall D). Now, 5 passes creates a 10.5 GeV electron beam to Halls A, B and C. Hall D received electrons from 5.5 passes around the accelerator creating the 12 GeV electron beam energy. As Fig. 14 shows, the upgrade consisted of 5 additional cryomodules in each LINAC, an additional recirculation arc, increased capacity of the Central Helium Liquefier (CHL), and improvements in the curving magnets.[26]

The electrons are accelerated in CEBAF by way of the LINACs. These LINACs contain a set of superconducting Niobium accelerating cavities with electromagnetic fields that oscillate at a frequency of 1.5 GHz. Electrons are injected in bunches into the accelerator with an energy of 45 MeV at the same frequency as the cavities every 0.7 ns.[27] These electrons then circulate around, increasing in energy each pass through the LINACs. Once the desired energy for a given hall is reached, every 2.1 ns magnetic fields inside the arcs force the electrons into specific central trajectories that guides them into that hall. The beam is considered “continuous” because the high operating frequency has a maximum current of 200 μ A. Each hall contains a device called a Faraday Cup (FC) located at the end of the beam line that measures the total amount of charge accumulated, which allows for monitoring of the number of electrons impacting its target during the taking of data.

3.2 CEBAF LARGE ACCEPTANCE SPECTROMETER

Once the electrons are accelerated to a desired energy, they are received by the halls, where they are directed towards a target. The scattered particles enter each

hall's spectrometer, while beam electrons that do not scatter off the target hit the FC. A spectrometer is an instrument (or collection of instruments) that measures and analyzes a range (or spectrum) of processes or reactions. In scattering experiments, a spectrometer separates particles in space via some physical property, and the magnets in the spectrometer separates particles based on momentum. Because BONuS12 will operate in Hall B, here we will focus on the components and operation of Hall B's spectrometer, called the CEBAF Large Acceptance Spectrometer at 12 GeV energy (or CLAS12). As the name suggests, CLAS12 is an evolution of CLAS6 (or just CLAS as it was known before talk of the energy upgrade), which was the original spectrometer built for Hall B.

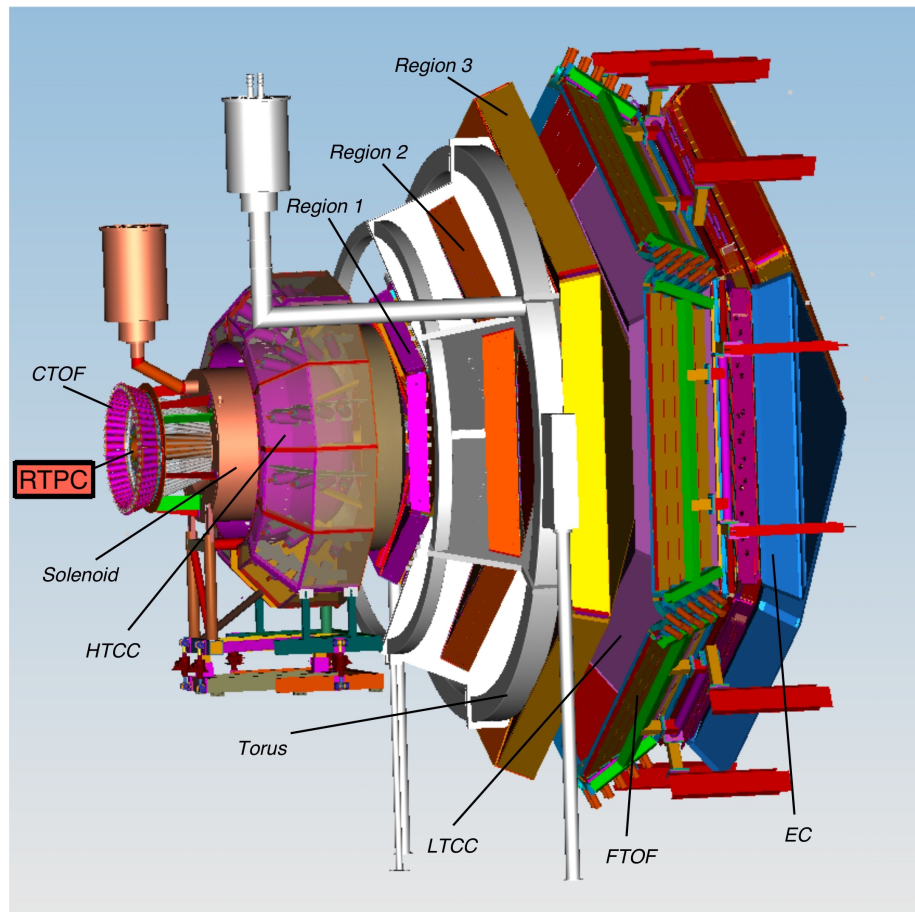


Fig. 15: The CEBAF Large Acceptance Spectrometer at 12 GeV (CLAS12) [26].

CLAS12 (see Fig. 15) consists of two major groups of detectors, which together allow for detection and identification of particles over a large scattering angle, thus

the “Large Acceptance” in the name CLAS12. The Forward Detector (FD) covers scattering angles of between 5 and 40 degrees, and consists of a torus magnet, Cherenkov counters, a time of flight detector, drift chambers and electromagnetic calorimeter. The other group of detectors is known as the Central Detector (CD), and covers scattering angles between 40 and 125 degrees.[35] The CD consists of a solenoid magnet, time of flight detector and finally, the BONuS12 RTPC. We will discuss each of these detectors, with a bit more focus on the RTPC.

3.2.1 TORUS MAGNET

The torus magnet is comprised of six superconducting coils arranged symmetrically around the beamline to create an azimuthally-symmetric magnetic field up to 3.5 T. The coils are cooled to an operating temperature of 4.5 K by liquid helium.[28] The shape of the coils was designed to create a field that increases near the center, which provides the desired resolution as a function of θ .

The purpose of the magnetic field is to curve the tracks of charged particles without changing their azimuthal (ϕ) angle. This curvature allows for the increased capability of particle identification by separating particles by their momentum. Its open structure allows for long path lengths for both charged and neutral particles, which also contributes to particle identification through time-of-flight measurements.

3.2.2 CHERENKOV COUNTERS

When a charged particle moves through a dielectric¹ with a speed greater than the phase velocity of light in that medium, electromagnetic radiation (*i.e.* light) is emitted. This is known as Cherenkov radiation. By changing the refractive index of that medium, the threshold for emission of that light is modified. The threshold of the particle energy is given by [29]

$$E = \frac{m}{\sqrt{1 - \beta^2}} = m \frac{n^2}{n^2 - 1}, \quad (80)$$

where m is the mass of the particle, β is its speed in units of the speed of light, and n is the index of refraction of the medium. This effect allows for the distinction of particles having the same momentum but different mass. By using a material with a specific refractive index, a heavier particle may not produce Cherenkov light, but a lighter particle may.

¹A dielectric is any insulator that can be polarized when an electric field is applied.

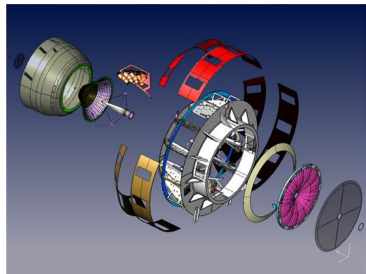


Fig. 16: The High Threshold Cerenkov Counter [29].

CLAS12 contains two detectors that exploit this Cherenkov effect. The High Threshold Cherenkov Counter (HTCC seen exploded in Fig. 16) is between the target and the first region of the Drift Chambers. It discriminates electrons from charged pions, kaons, and protons by being filled with CO₂.[29] This gas has an index of refraction $n = 1.00041$, which forces pions above 4.9 GeV to produce light. If the particle has an energy below this threshold and it produces light, it is an electron. The other Cherenkov detector is the Low Threshold Cerenkov Counter (LTCC), which sits between Region 3 of the Drift Chambers and the Forward Time of Flight detector. It is filled with C₄F₁₂, which allows for the detection of pions above a momentum of 3.5 GeV where only pions produce Cherenkov light.[30]

3.2.3 DRIFT CHAMBERS

There are three regions of Drift Chambers (DC) that collectively allow for the reconstruction of charged particle trajectories. The first region is located in front of the Torus Magnet outside of the field. Region 2 is between the coils in the high field region. The third region is after the torus, but feels a small magnetic field from the coils. Each region is made of six triangular sectors, which consists of small wires under tension and at high voltage.

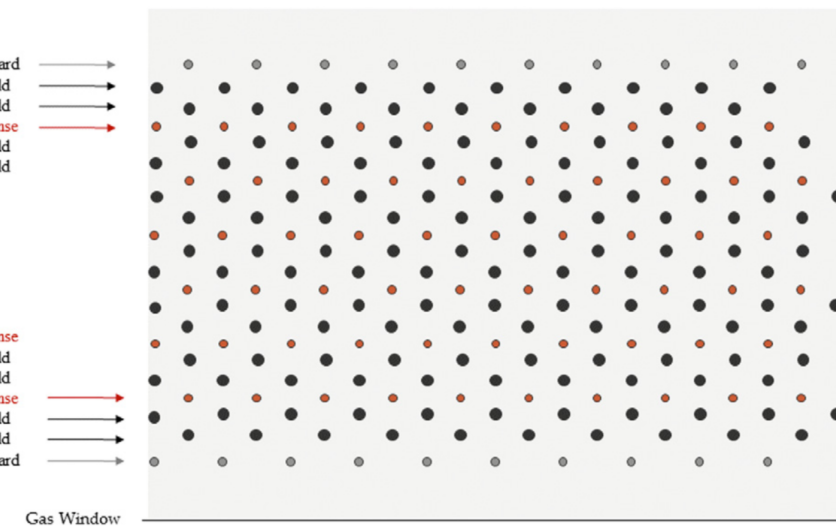


Fig. 17: Hexagonal wire layout for the drift chamber [31].

Within the sectors of the DC there are hundreds of wires. Sense wires are located in between field wires all in a hexagonal pattern (see Fig. 17). When a charged particle travels through the DC gas mixture of 90% Argon 10% CO₂[31], it ionizes the gas molecules as it passes. In the DC, these ionization electrons are accelerated to the nearest sense wire by the electric field. The accelerating electron creates an electron avalanche as it approaches the sense wire. That avalanche makes for a detectable signal on that wire.

Using the signals created by the ionization electron-ion pairs as the primary charged particle travels through the regions of the DC allows for the reconstruction of that particle's path. This information lends itself to the reconstruction of the particle momentum as well as its vertex in the target (*i.e.* where the particle originated). This information will be vital in BONuS12 for identifying the electron created in the $eD \rightarrow e'p_sX$ process.

3.2.4 FORWARD TIME OF FLIGHT

Two charged particles having the same momentum will travel at different speeds depending on their mass. The Forward Time of Flight detector (FTOF) measures the time of arrival of those charged particles emerging from the target. Primarily, the FTOF will help separate pions and kaons for energies below 3 GeV. Higher energies are handled by the Cherenkov counters. Because higher momentum particles scatter at lower angles, the FTOF was constructed to have better timing resolution at lower angles. That resolution can be as small as 80 ps at the more forward angles and 150 ps at larger angles (*i.e.* over 35 degrees).[32]

The FTOF is made of six sectors of plastic scintillators coupled to double-sided PMT readout. Within each sector, there are three arrays of counters. Panel 1a, which covers 5 to 35 degrees in θ contains 23 counters. Panel 1b also covers angles between 5 and 35 degrees and contains 62 counters. Finally, Panel 2 has 5 counters covering only angles between 35 and 45 degrees.

3.2.5 ELECTROMAGNETIC CALORIMETER

Electromagnetic calorimeters measure the energy of particles traveling through it that interact via the electromagnetic interaction. The EC in CLAS12 contains three layers. The preshower calorimeter (PCAL) is the first layer and is used to identify two close gammas, which will help discriminate between neutral pions and single

gammas. The next two layers are the inner and outer electromagnetic calorimeters (EC_{in} and EC_{out} , respectively). Both are used collectively with the PCAL to identify electrons, photons, $\pi^0 \rightarrow \gamma\gamma$, and neutrons.

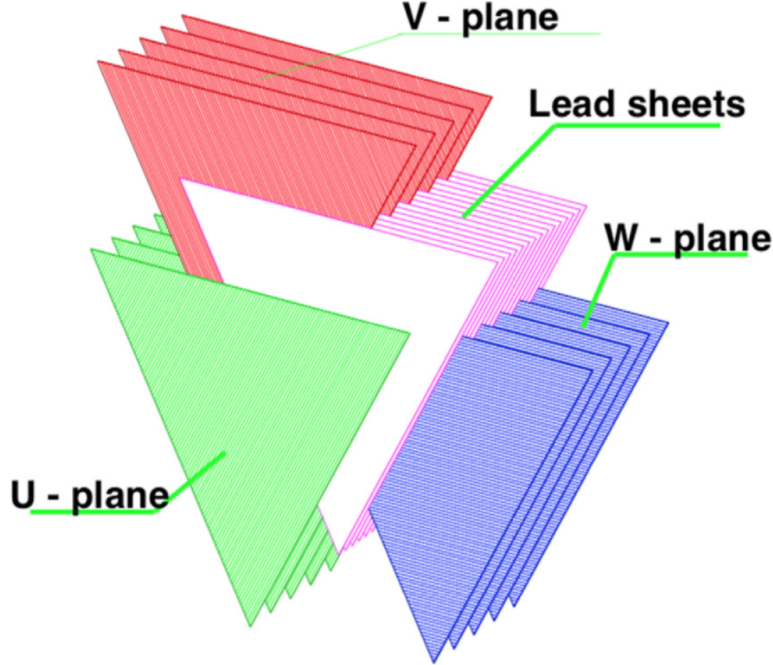


Fig. 18: Exploded view of a sector of the Electromagnetic Calorimeter (EC) for CLAS12 [33].

The requirements of the EC are to identify electrons with energies above 0.5 GeV, and photons above 0.2 GeV, helping to reconstruct π^0 and η particles through their neutral decays. The EC can also provide photon/neutron separation by utilizing TOF information available.

Each layer of the EC is comprised of six triangular sectors. Each sector is made of alternating layers of scintillators strips and lead sheets. The spatial-coordinate readout comes from the three planes (U, V, and W) seen in the exploded view of one sector in Fig. 18, which each contain 36 scintillator strips that run parallel to one side of the nearly equilateral triangular sectors. Strips are rotated by 120° in each successive layer, which allows for effective translation to x, y, and z coordinates.[34]

3.2.6 FARADAY CUP

The Faraday Cup (FC) is a detector that measures the amount of charge deposited in it by particles. The Faraday Cup in CLAS12 sits 29.0 m downstream of the CLAS12 target and is composed of 4000 kg of lead supported on ceramic standoffs inside a vacuum chamber.[35] An electrical feed-through provides a way to draw the deposited charge from the FC. The FC not only measures the integrated charge, but can also measure of the variation in charge with helicity for experiments using polarized electrons.

3.2.7 SOLENOID MAGNET

The solenoid magnet and the remaining two detectors to follow (*i.e.* the Central Time of Flight and Radial Time Projection Chamber) are all members of the group known as the Central Detector. The Solenoid is a super-conducting magnet cylindrical in shape that surrounds the beam line. It is capable of producing a field of up to 5T along the beam line.[28] Charged particles experiencing this field curve in a helical trajectory, which allows for reconstruction of those trajectories and discrimination between charged and neutral particles.

The other purpose of the solenoid is to shield the Forward Detector from electron-electron collisions, called Møller electrons. Because the field is strongest closest to the target, most Møller electrons originating from the beam line are isolated by the solenoid's field to small polar angles (θ) where none of the FD materials exist. The other means of protection from these Møllers comes from a shield around the beam line located outside the Central Detector as well as a shield just in front of a small detector called the Forward Tracker, which for the BONuS12 experiment will be turned off.

3.2.8 CENTRAL TIME OF FLIGHT

The Central Time of Flight (Fig. 19), or CTOF, is located inside the solenoid. Just as the FTOF, the CTOF measures the time of flight of particles originating at the reaction vertex. It is made of 48 scintillator bars that form a barrel and spans polar angles of 35° to 125° that surround the target with full azimuthal coverage. The scintillators are coupled on each end by magnetic-field-sensitive PMTs, which are positioned out of the solenoid field by long light guides. The resulting CTOF

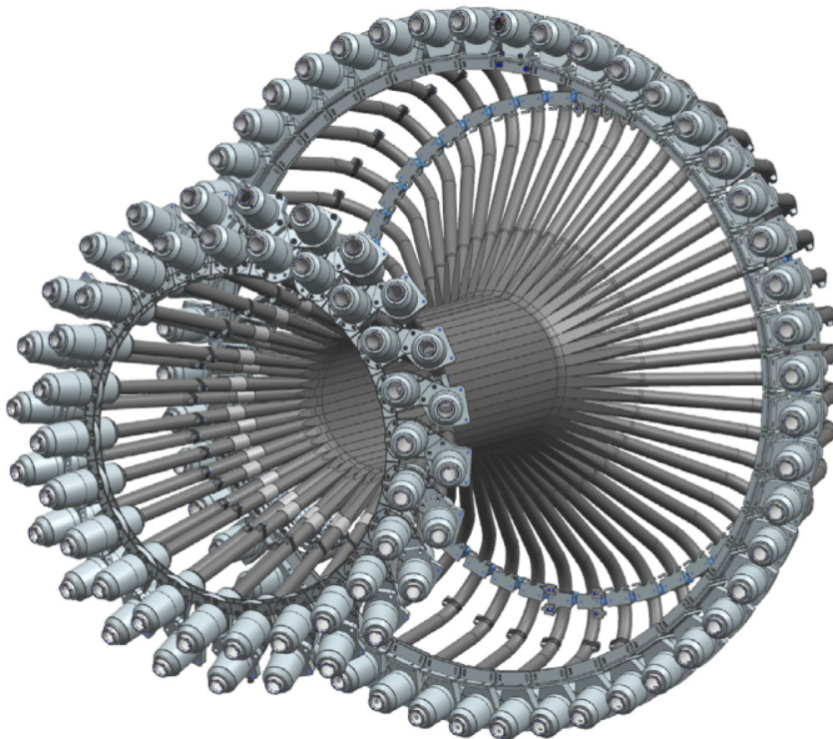


Fig. 19: The Central Time of Flight Detector[36].

operates with a time resolution of 60 ps [36], which was the requirement for particle identification.

3.3 BONUS12 RTPC

During Run Group F (RGF) in Hall B at JLab, all of the detectors just described will be present in addition to one more that will be located inside the solenoid magnet and CTOF. That detector is the BONuS12 Radial Time Projection Chamber (RTPC). Its purpose is to detect backward going low momentum protons by way of ionization electrons created as protons pass through the RTPC.

3.3.1 COMPONENTS AND THEIR PURPOSE

Accelerated electrons that enter Hall B meet the 40 cm RGF target. That target measures 3 mm radially and is filled with gaseous deuterium at 7 atm pressure surrounded by a 63 μm thick Kapton wall. When an electron collides with the

neutron in a deuteron atom, it continues in the forward direction into the Forward Detector of CLAS12. That collision also results in the ejection of a proton that drifts radially outward into the RTPC.

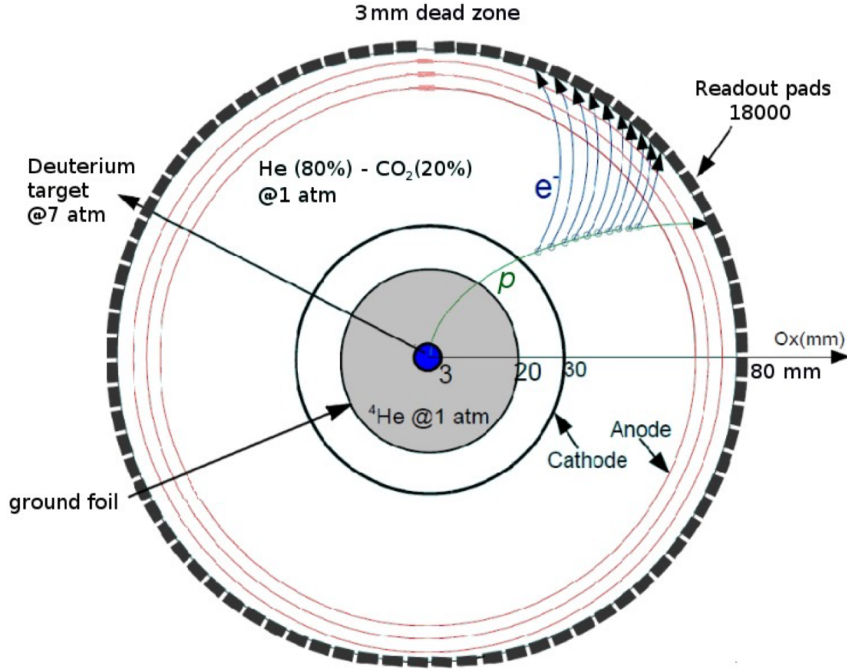


Fig. 20: Cross section of the RTPC showing a proton traversing the detector with ionization electrons drifting toward the readout pad board.

That proton is guided toward the outer edge of the RTPC by way of an electric field created within it. That field is established with a ground foil at 2 cm and a cathode foil at 3 cm (see Fig. 20). The cathode foil is given a high negative potential and the ground foil is at zero potential to protect the target from charging up. Then the potential difference between the cathode and first Gaseous Electron Multiplier (GEM) foil at 7 cm creates an electric field through the active region of the RTPC.

This active region between 3 and 7 cm is where the proton creates ionizations along its path outward. The region is filled with a gas mixture of 80% Helium and 20% CO₂, which was chosen for its fast drift times and minimal drift angle (more about this in Section 4.3.4). Because of the magnetic field created by the solenoid, the proton curves in one direction as it moves outward while the ionization electrons it creates curve in the opposite direction due to their opposite charge.

Every time an ionization electron is created, it is also driven by the electric field toward the outer edge of the RTPC where there are three layers of GEM foils. That

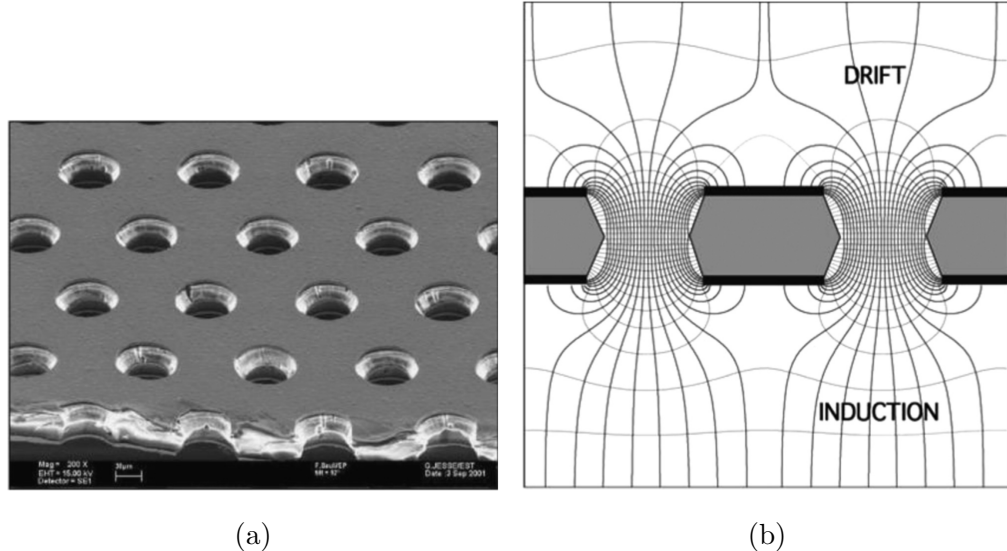


Fig. 21: (a) Electron microscope picture of a section of typical GEM electrode, 50 μm thick. The holes pitch and diameter are 140 and 70 μm , respectively[37]. (b) Electric field in the region of the holes of a GEM electrode [37].

pad board provides full coverage in ϕ with the exception of one 3 mm dead zone down the length of the RTPC. However, because a single electron cannot be easily readout, that electron will encounter three layers of GEM foils at radii of 7 cm, 7.3 cm and 7.6 cm. Fig. 21(a) shows the surface of a GEM foil under an electron microscope. As the electron approaches the GEM foil, it is directed through one of the holes in the GEM foil by the electric field around the hole.[37] That electric field shown in Fig. 21(b) creates an electron avalanche that multiplies the number of electrons. The GEM foils are used to amplify the number of electrons from one to something significant enough to register on the electronics. Each GEM has a gain of about 100, which means that through three GEM layers, one electron could become 1,000,000 after exiting the last layer.

Once this avalanche of electrons has been created by the GEMs, their final destination is the read out pad board at 8 cm. The pad board has 180 pads around ϕ by 96 pads in z totaling 17,280 readout pads. These pads, coupled to translation boards that act as current-limiting adapter boards, read the signal that the electron avalanche makes.

The signals from the readout pad board are driven from the translation boards to

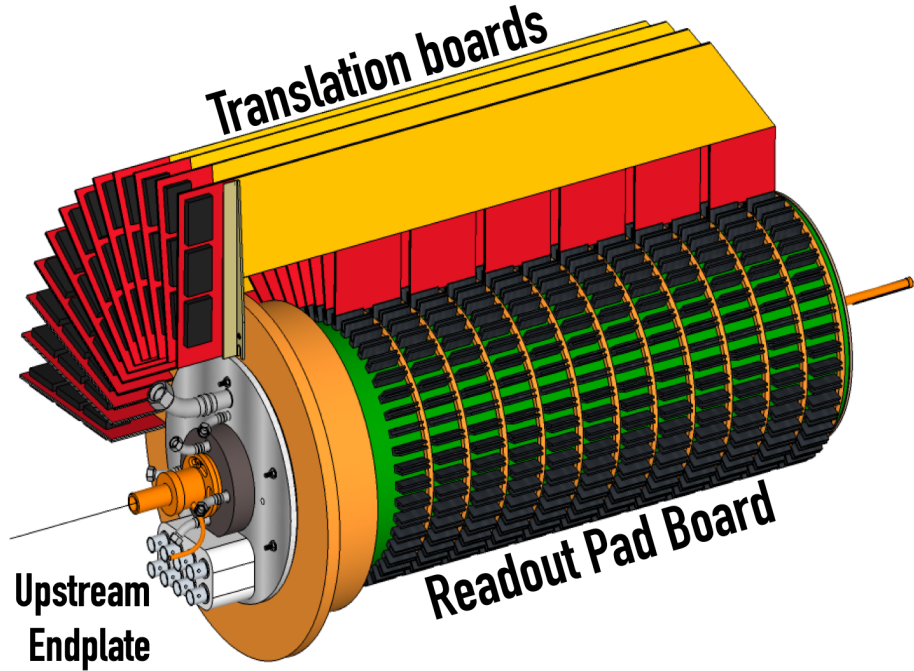


Fig. 22: Design of the RTPC with only one-quarter of the translation boards attached.

the data acquisition system (DAQ) on the front-end electrical units. The BONuS12 DAQ begins with the Dead-timeless Readout Electronics ASIC for Micromegas (DREAM) chips. Each DREAM chip contains 64 channels. Each channel has amplifier, shaper, analog buffer, and discriminator integrated within it. The chip has a readout rate up to 20 MHz and a dead-timeless operation of up to 20 kHz. Fig. 23 shows the layout of the DREAM chip.

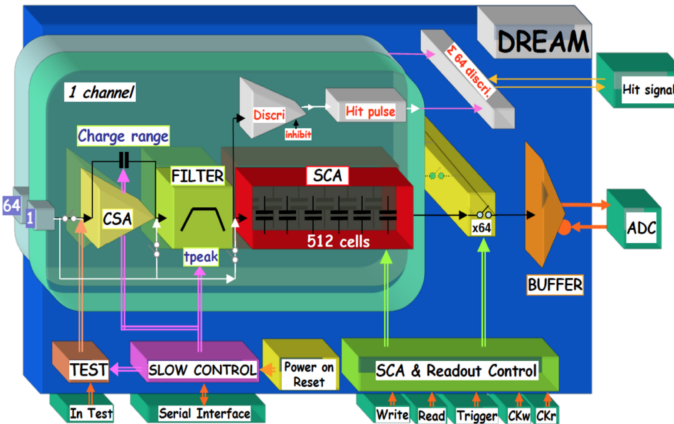


Fig. 23: Map of the DREAM chip [38].

The BONuS12 front-end unit (FEU) utilized the same electronics as the Microgeomas Vertex Tracker, which was a detector removed to make room for the BONuS12 RTPC. The FEU contains 8 DREAMs (512 channels), 12-bit 8-channel Analog to Digital Converters (ADCs), Xilinx Virtex-6 FPGA connectivity kits, 2 Mb static RAM, SFP optical transceiver, and a trigger interface. The FEU electronics then drives the signal to the CLAS12 data acquisition system [39], which stores the data for analysis. Fig. 24 shows the RTPC DAQ map from signal to back end unit data storage.

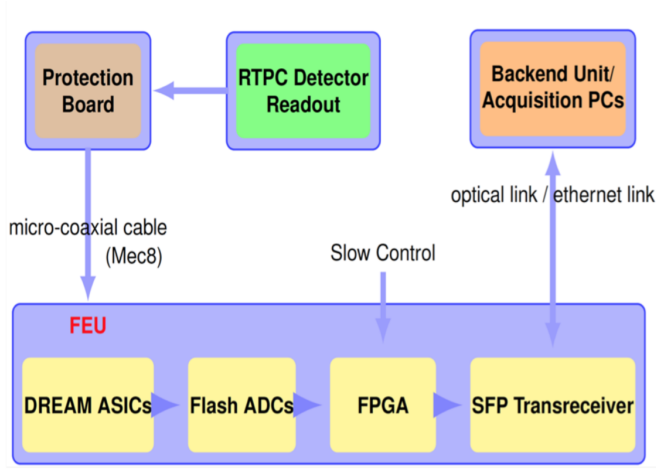


Fig. 24: The BONuS12 data acquisition map. Signals from the readout pad board go through the translation boards to the front-end unit electronics. The raw events get read into the slow controls and gets uploaded to the back end unit computer systems.

3.3.2 RTPC CONSTRUCTION AND INTEGRATION

The construction of the BONuS12 RTPC began at Hampton University in Hampton, Virginia around 2017. Because of the cylindrical shape of the detector, mandrels were used widely in the shaping of the detector components. The ground foil, cathode foil, the three layers of GEM foils, and pad board were all assembled using mandrels. Fig. 25 is a drawing of the assembly station for the RTPC, which includes an actuator that removes wrapped foils from the mandrel and places into the detector on the assembly station.

The first assembled detector (RTPC1) was delivered to JLab in November 2019. The RTPC underwent testing with cosmic rays in the Experimental Equipment Lab

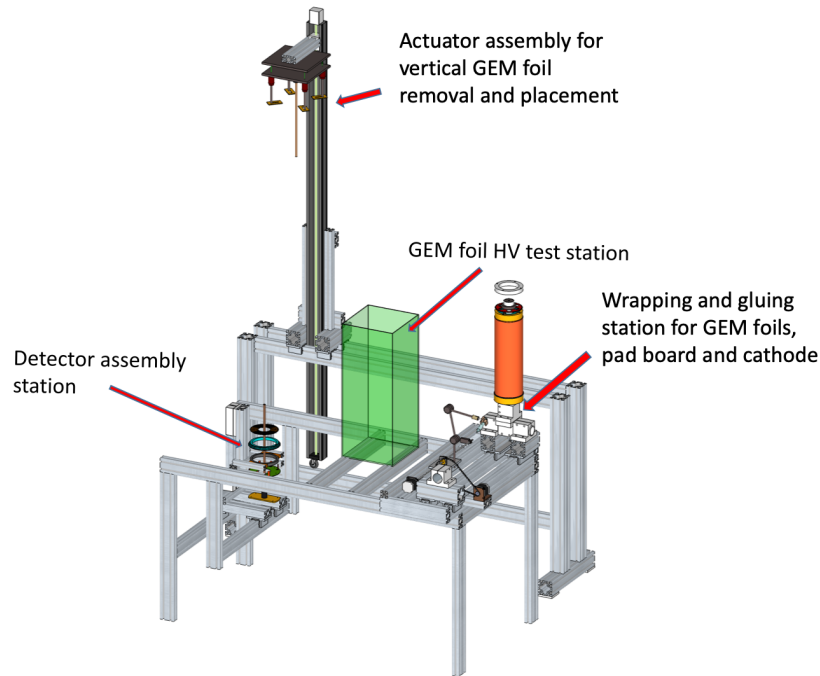


Fig. 25: Assembly station for the RTPC.

(EEL) at JLab with the full array of components that were eventually installed in the Experimental Hall (*i.e.* RTPC, gas panel including the Drift-gas Monitoring System, DAQ, etc).

Once that testing was complete, in late January 2020 the BONuS12 RTPC was installed in Hall B. Run Group F, of which the BONuS12 experiment is a part, required installation of three layers of the Forward Micromegas Tracker (FMT).² The support shell and FEUs of the Micromegas were utilized since it allows all electronics to sit outside of the strong solenoid magnetic field.[40] The Forward Tagger required switching to the FTOff condition, which included placing a Møller shield in front of the FT.[41] After all detector installation was complete in Hall B, cosmic tests were done again. This data stream, for the first time, allowed for the RTPC from within the CLAS12 to be utilized in the full Data Acquisition System [39] while inside the hall.

²The FMT was originally a part of the Micromegas Vertex Tracker (MVT), which consisted of the FMT and Barrel Micromegas Tracker(BMT). Together the FMT and BMT were designed to improve upon the baseline CLAS12 tracking capabilities.[40] Originally, the FMT contained 6 disks placed 30 cm downstream of the target. For the RGF setup, 3 of those FMT disks were used and the BMT was completely removed to make room for the RTPC.



Fig. 26: The fully assembled BONuS12 RTPC with the FEUs attached, but not yet with the 3-layer FMTs attached.

3.3.3 BONUS12 DRIFT-GAS MONITORING SYSTEM

The gas system for BONuS12 provides gases for the target (deuterium), the buffer regions (helium), and drift region (He:CO₂). The gases begin in the gas bottles. The gases travel through the panel seen in Fig. 27, where the target gas flows through the top, the buffer gas through the middle, and the drift gas through the bottom of the panel. The flow rate is set by Mass Flow Controllers (MFCs) controlled through the CLAS12 slow-control interface Experimental Physics Industrial Control System (EPICS). Once the gas goes through gas-relief bubblers, it enters the RTPC. After flowing through the RTPC, the target and buffer gases goes back through the gas panel and out through exhaust ports. The drift gas exits the RTPC and enters the gas panel into the RTPC Drift-gas Monitoring System (DMS).

The drift velocity of electrons in the RTPC are very sensitive to fluctuations in the gas-mixture and electric field, as well as the temperature and pressure of the gas in the drift region (see 4.3.4). Therefore, a system was designed that monitors the drift velocity of electrons. A small drift chamber was built that sat downstream of the RTPC and was fed by the drift gas coming from the RTPC.

Since the purpose of the DMS was to measure the drift velocity within the gas mixture, the focus of the DMS design was measuring that velocity through a near-constant electric field. The design concept (seen in Fig. 28) is a drift chamber. Two radioactive sources separated by 4 cm emit β electrons that are detected by associated scintillator/photomultiplier tubes (PMTs). When these electrons travel through the gas, they create ionization electrons along their path. Within a sensitive

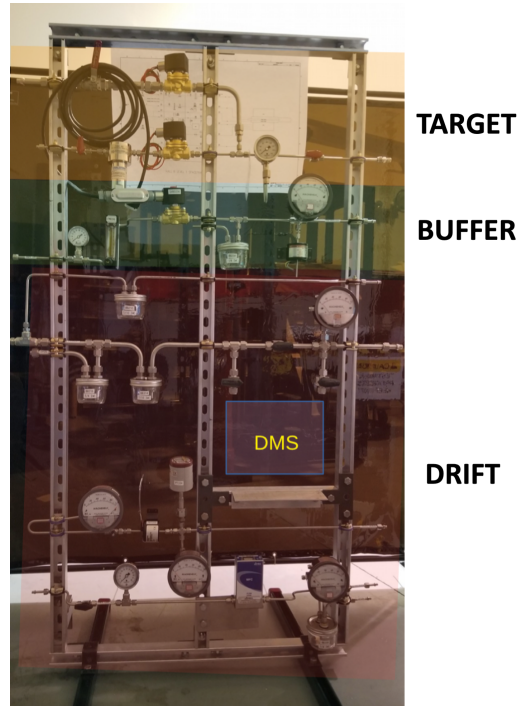


Fig. 27: The RTPC gas panel. The target gas flows through the top part of the panel, the buffer gas flows through the middle region of the panel, and the drift gas flows through the bottom region of the panel.

region in the center of the DMS, those ionization electrons are guided to an anode wire behind a small slit in a grounded plate by an electric field.

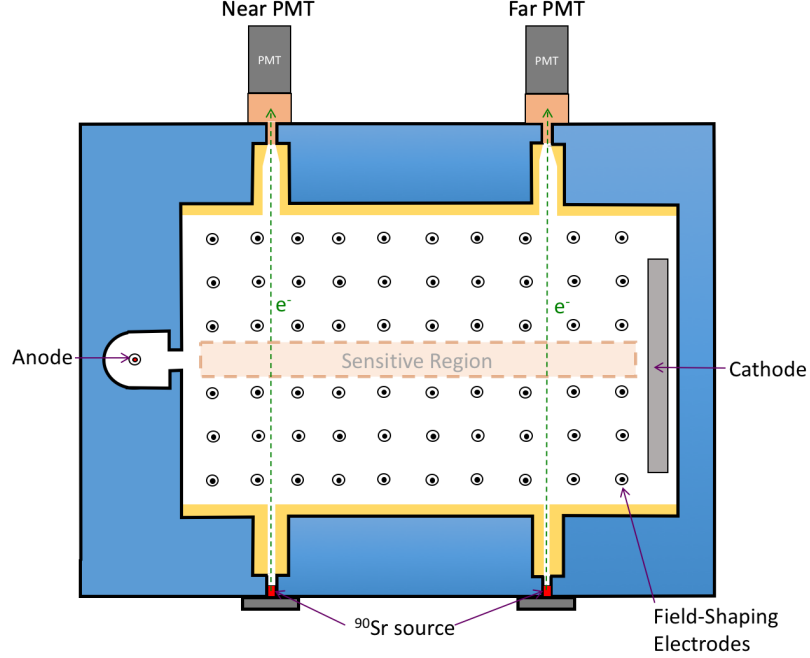


Fig. 28: Design concept of the Drift-gas Monitoring System (DMS) for the BONuS12 experiment.

The electric field that guides the ionization electrons to the anode is created by a cathode with a high negative potential, an anode with a high positive potential, and field-shaping electrodes that have potentials stepped down by equal amounts from a voltage-divider circuit. This ensures the field within that sensitive region is uniform, so the drift velocity is constant between the two sources.

The DMS outer structure was made from the synthetic polymer called Delrin. Each piece was made on a CNC machine to fit the specifications required. Appendix A contains all drawings and specifications of the DMS. The electrodes (specifications also found in Appendix A) were made from steel. Once the parts were machined, they were assembled in such a way as to leave the stringing of the anode wire last. Each side of the DMS was held together by plastic screws. Fig. 29 shows the partial construction of the DMS without the last face attached, so the electrodes and cathode exposed. The Photonis XP 2979 PMTs were held in place using a custom built plastic support system (see in Fig 30 as the black structure with black PMT tubes on the right side). The two $2 \mu\text{Ci}$ sources were held in place using a Delrin plate. The 30

μm anode wire was strung and crimped.

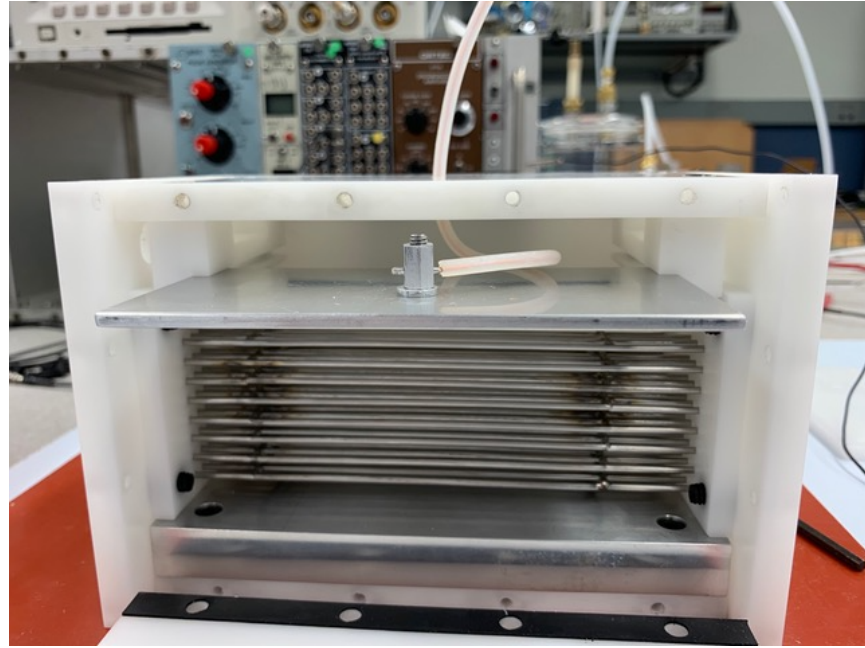


Fig. 29: Partial assembly of the DMS showing the wired cathode at the top and the anode ground plate at the bottom with the field shaping electrodes in between.

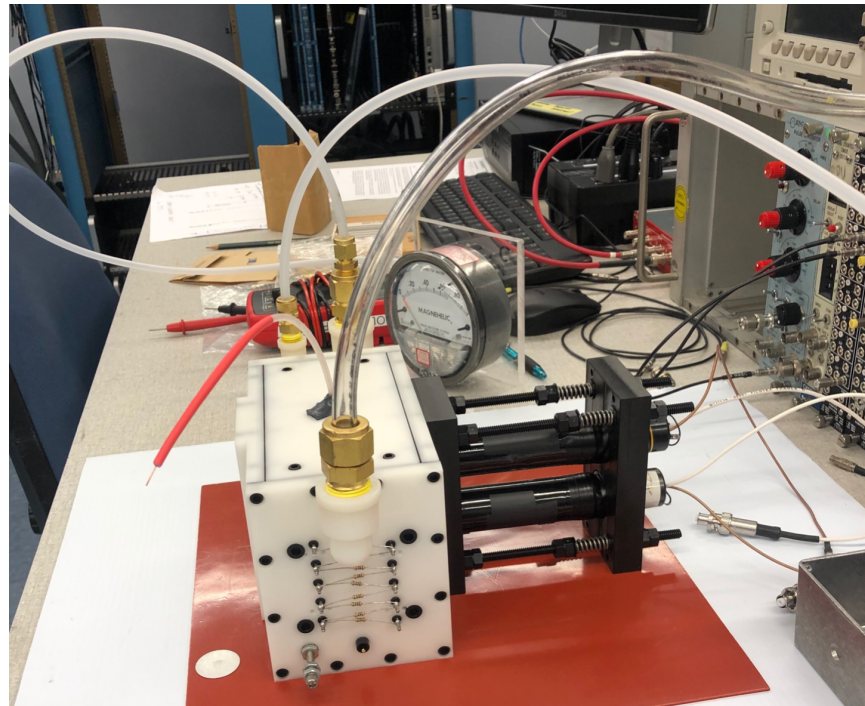


Fig. 30: Assembled DMS with electrode wiring.



Fig. 31: Fully assembled DMS with electronics panel shown in the back.

In order to block any background electromagnetic noise, the entire system was placed in a metal grounded box (see Fig. 31). The high-voltage (HV) supply circuits seen in Figs. 32 and 33 were designed to filter out any fluctuations in the HC supplies. Both circuits were soldered on separate circuit boards and placed on a grounded metal plate along with the preamp/postamp circuit. That grounded plate was screwed to the back of the grounded box and can be seen in the back of the box in Fig. 31 behind the DMS.

When a signal is detected at the anode (the trigger), a Time-to-Digital Converter (TDC) (see Fig. 34 for the DMS DAQ map) looks for an associated signal from a source β electron detected by either PMT (the PMT closest to the anode is channel 1 and the PMT farthest is channel 2) and measures the time difference between the two signals. When a coincidence occurs, the time difference between trigger and the associated PMT signal is then added to a histogram. As enough statistics populate the histogram, two peaks formed representing events from the two sources and a difference in the two times can be calculated. Given the known distance between the sources and the time difference between the two peaks, the drift velocity is calculated:

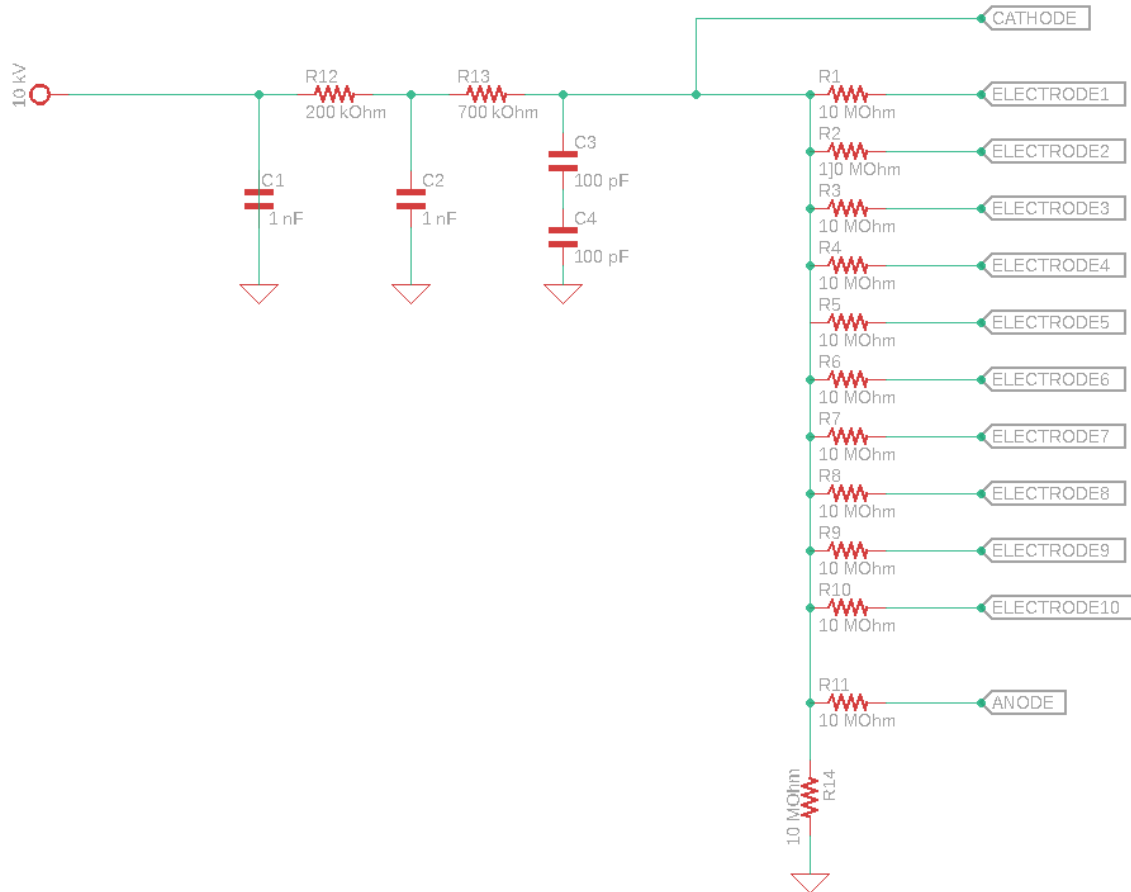


Fig. 32: Cathode and electrode HV supply circuit.

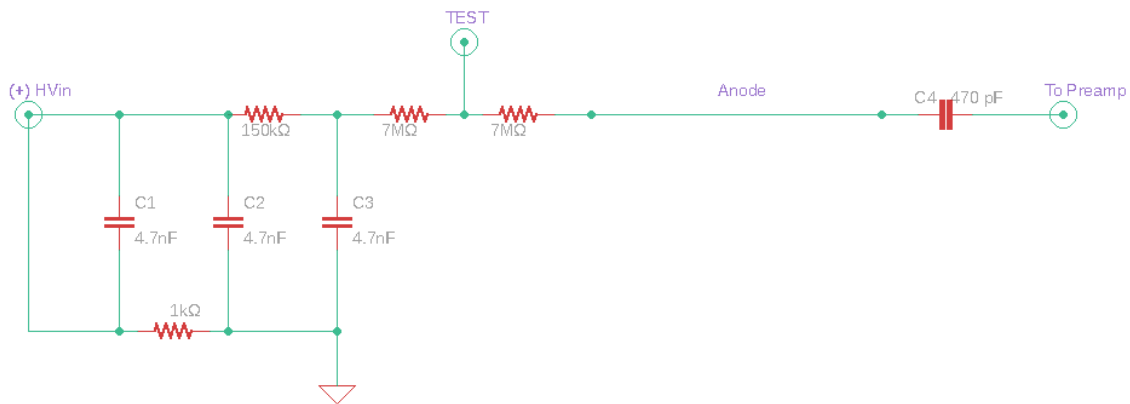


Fig. 33: Anode HV supply circuit.

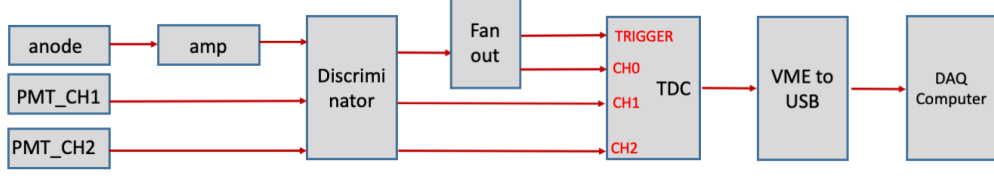


Fig. 34: The DMS DAQ flow from signal to computer.

$$v_{\text{drift}} = \frac{\Delta d}{\Delta t} = \frac{4 \text{ cm}}{t_{\text{CH2}} - t_{\text{CH1}}}, \quad (81)$$

where v_{drift} is the drift velocity, Δd is the distance between sources (equal to 4 cm), t_{CH1} and t_{CH2} are the mean values of the Gaussian fits to the peaks from channel 1 and channel 2 respectively. The error on the drift velocity is calculated by

$$\sigma_v = \frac{\sqrt{\sigma_{t\text{CH1}}^2 + \sigma_{t\text{CH2}}^2}}{t_{\text{CH2}} - t_{\text{CH1}}}, \quad (82)$$

where $\sigma_{t\text{CH1}}$ and $\sigma_{t\text{CH2}}$ are the sigmas on the Gaussian fits for channel 1 and channel 2 respectively. Then the drift velocity is plotted versus elapsed time, giving a means to monitor that velocity.

CHAPTER 4

BONUS12 SIMULATION AND DEVELOPMENT

The simulation and development of the BONuS12 experiment has been ongoing essentially since the original BONuS6 experiment in the early 2000's. The goal of BONuS has always been to detect backward going low momentum spectator protons in coincidence with scattered electrons at high Bjorken- x . The purpose of the simulation and development is to optimize the BONuS12 RTPC that will result in high statistics in the relevant kinematic range.

This chapter will focus on the methods used in the detector optimization in preparation for the BONuS12 experimental run. It will cover simulations done to improve geometry, determine electron drift time, and understand energy loss through detector components. The chapter will also go over the construction of the detector. Finally, the process of reconstruction will be covered, which is the way we ultimately determine the kinematics of each event in order to recover the structure functions we are interested in studying.

4.1 GEANT4 MONTE CARLO (GEMC)

Much of the simulations done in preparation for and during CLAS12 experiments use the Geant4 Monte Carlo (GEMC) software developed by Maurizio Ungaro at Jefferson Labciteclas12:GEMC GEMC, as the name indicates, uses a toolkit called Geant4. Geant4 was developed by CERN. It was released as a successor in the Geant software toolkit series, first released in 1998. Since then Geant4 has involved an international collaboration of contributors and maintainers with applications ranging from nuclear physics to medical physics.

The purpose of the Geant4 toolkit [43] is to simulate the passage of particles through matter. This can mean anything from particles going through biological material (*e.g.* simulating the effects of radiation on human tissue) to simulating particles moving through detectors, which is clearly the reason for its use in this project. In order to understand how the BONuS12 experiment simulations were conducted with GEMC, first we must become a little more familiar with Geant4.

Geant4 uses the object-oriented programming language C++ in various facilities to exploit its features. The first defining characteristic of this toolkit is its ability to define the geometry, or physical layout, of an experiment. This lets us consider how this geometry effects the particles moving through the materials in the experiment. The path that these particles takes as well as the interactions with the materials they pass through is another facility in Geant4 known as tracking.

The Geant4 Monte Carlo (GEMC) is a C++ framework that utilizes Geant4 and the Monte Carlo method of randomized sampling in order to obtain particle behavior through materials. At a very basic level, GEMC can define particle momenta and angles as well as detector geometry and material in order to understand the particle's behavior in that material. One can define a variety of output variables of interest in these simulations like total energy deposited, position, and momentum. There is much more that can be done with this simulation platform that will be discussed through the following sections. First, we must go over one more tool that was used for simulations called Garfield++.

4.2 GARFIELD++

While Geant4 and GEMC both deal well with the simulation of particles' interaction with matter, the particles of interest in the BONuS12 experiment also go through gases and will be under the influence of electric and magnetic fields. For a more specialized simulation of charged particles in such gases with electric and magnetic fields, we use a toolkit called Garfield++, which was developed at CERN. This is an extended version of the original Garfield platform that incorporates MagBoltz in the C++ language. MagBoltz solves the Boltzmann transport equations for electrons in gas mixtures under the influence of electric and magnetic fields. The other programs utilized to create a mesh of the RTPC and solve the electromagnetic equations inside the RTPC are GMSH and ElmerSolver, respectively. These packages and their purpose will be described more in the discussion of drift electrons as well as gas-mixture optimization.

4.3 BONUS12 RTPC SIMULATIONS

Throughout the next section, we will focus on the simulations that shed light on particle behaviors in the detector, drove optimization efforts, and offered insight

about expected results. We will go over all the tools that were used for the simulations and how each one was utilized and implemented. Computer simulations are immensely powerful and tend to be much less expensive than physical exploration and experimentation. We'll discuss how the packages already presented can come together to simulate the entire BONuS12 experiment from the RTPC to its inclusion in the CLAS12 detector.

4.3.1 GEOMETRY & MATERIALS

The first thing to do when simulating the BONuS12 RTPC in GEMC is to define its geometry and materials. This is done via Perl file, where one can use predefined materials from Geant4 (*e.g.* G4_KAPTON for Kapton, G4_Cu for copper, etc. [43]) or define custom materials. Geometries are defined both in Geant4 and GEMC by solid types like “tube”, “box”, “sphere”, etc. Since the BONuS12 RTPC is made of several different cylinders, most of the geometry definitions are of “tube” type. Therefore, we specify the dimensions in terms of r , ϕ and z . For example, the drift volume is defined in the code by

```
$detector{"name"} = "sensitive_drift_volume";
$detector{"mother"} = "rtpc";
$detector{"description"} = "Sensitive drift volume";
$detector{"color"} = "ff88994";
$detector{"type"} = "Tube";
$detector{"dimensions"} = "$rmin*mm $rmax*mm $z_half*mm $phistart*deg
$pspan*deg";
$detector{"material"} = $mate;
$detector{"style"} = 1;
$detector{"sensitivity"} = "rtpc"; ## HitProcess definition
$detector{"hit_type"} = "rtpc"; ## HitProcess definition
print_det(\%configuration, \%detector);
```

where the material (`$mate`) is made of 80% ${}^4\text{He}$ and 20% CO_2 (defined elsewhere) and `$rmin= 30.0`, `$rmax= 70.0`, `$z_half= 192.0`, `$phistart= 0.0`, `$pspan= 360.0` in this case. One defines the units within the declaration of `$detector{"dimensions"}`; `$rmin*mm` would be 30.0 mm, for example. There are other variable names that are seen within the detector attributes above that are important to understand. The

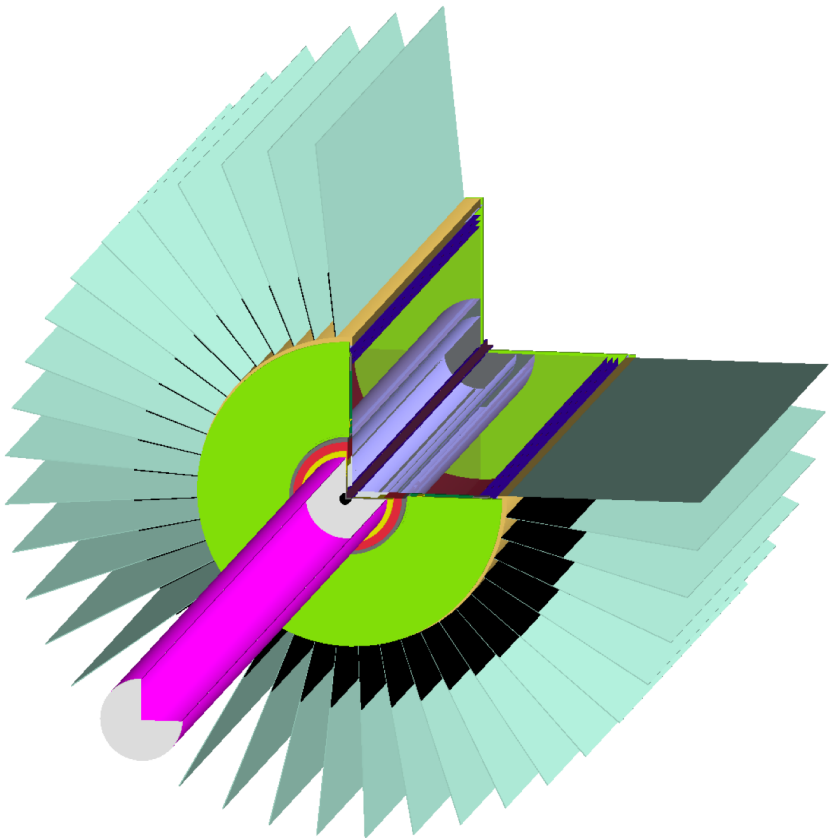


Fig. 35: BONuS12 RTPC geometry implemented in GEMC

variable `style` describes whether the type is a solid (`style = 1`) or wire frame (`style = 0`). The `sensitivity` variable directs GEMC to add the output of this region to the correct bank in the output file. In order to define what particle-interaction output variables appear in the output file for the given volume, we use the `hit_type` variable. Hit type will be covered more in Section 4.3.3 when we discuss what to do when ionization occurs in the drift region.

Not all of the RTPC details can be implemented into GEMC, so we only include the important components in the GEMC simulation. Those components include the main detector parts like the target, ground and cathode foils, GEM foils, and readout pad-board. Then there are the components that had to be included in order to understand their effect on the particles that may be traveling through them (*e.g.* down-stream end plate, electronics and translation boards, support ribs and spines, etc). Most of these secondary components had to be simplified in order to save time

during the simulation process. For example, a cylindrical volume of average density was included outside of the readout pad-board. This density included a proportional amount of the support ribs and spines, electronics, and air. The final geometry can be seen in Fig. 35, which shows the RTPC with a quarter slice taken out in order to see the internal structure.

Once the geometry is set up for the RTPC, it must be inserted within the CLAS12 detectors in GEMC. The file that brings all these detectors together in GEMC is an XML (*i.e.* extended markup language) file called a *gcard*. This file is where one defines not only which detectors to include in the simulation, but also what variables to include in the output file and what the incoming particle beam should be (*e.g.* momentum, angle, spread, etc.). For example, if one desired 10.6 GeV/c electrons to travel at 0° scattering angle θ and 0° around ϕ , with a spread of ± 10 MeV/c in momentum, $\pm 10^\circ$ in θ and $\pm 180^\circ$ in ϕ , the code would be:

```
<option name="BEAM_P" value="e-, 10.6*GeV, 0.0*deg, 0.0*deg"/>
<option name="SPREAD_P" value="10*MeV, 10*deg, 180.0*deg"/>
<option name="BEAM_V" value="(0, 0, 0)cm"/>
<option name="SPREAD_V" value="(0.3, 20)cm"/>
```

Notice that in this code snippet, the vertex of the particle `BEAM_V` is set to zero and there is a spread on that vertex `SPREAD_V` of $0 \text{ cm} \leq r \leq 0.3 \text{ cm}$ and $-20.0 \text{ cm} \leq z \leq 20 \text{ cm}$, which spans the diameter and length of the BONuS12 RTPC target.

This method of generating particles makes use of GEMC’s internal event generator. The particles that can be generated make use of the Geant4 particle bank. The trouble with this internal generator is that we do not have access to multiple particles that we may want to examine (*i.e.* secondary particles like other protons that may be in the RTPC at the same time as our “primary” proton). For that we have to look toward another method of generating particles and how to import that file into GEMC.

4.3.2 EVENT GENERATOR

For the purpose of our GEMC simulations in BONuS12, we are primarily concerned with the reaction $eD \rightarrow e'pX$ and so we need a means of generating such events. For that we use an external particle generator called Pythia. Pythia is a program for generating high-energy physics events, which is precisely what we need.

It uses known cross section data and models for e^- collisions between particles like e^- , e^+ , p and \bar{p} (*i.e.* anti-proton) to generate output in a file format named Lund, after the University where the program was developed.

TABLE I: Lund file header

Column	Quantity
1	Number of particles
2	Mass number of the target
3	Atomic number of the target
4	Target polarization
5	Beam Polarization
6	Beam particle type
7	Beam energy (GeV)
8	Interacted nucleon ID (proton or neutron)
9	Process ID
10	Event weight

This Lund output file format has very specific variables that we can take advantage of in GEMC. The first line of this Lund file contains header information for the particles to follow from the reaction simulation. This header contains 10 different columns, listed in Table I. The items in bold are used by GEMC. The header information not in bold is user defined and is not used by GEMC, but is kept in the output stream. Given the number of particles listed under column 1, there will be a list below the header with particle details for each (see Table II). That is, if there is a 5 listed under the first column in the header, then below the header will be 5 rows containing the details for each of the particles. For a simulation with multiple events, subsequent events appear after the last particle of the previous beginning again with the header line.

For the BONuS12 experiment, the event generator created a Lund file with various $D(e, e', p_s)X$ events that we must run through GEMC. To do this, instead of utilizing the GEMC internal event generator, we include the following line of code

```
<option name="INPUT_GEN_FILE" value="LUND, event_gen.lund"/>
```

in the gcard that we use to give direction to GEMC. This file will serve to instruct

TABLE II: Details about each simulated particle in an event (Lund format).

Column	Quantity
1	Index
2	Lifetime [nanoseconds]
3	Type (1 is active)
4	particle ID
5	Index of the parent
6	Index of the first daughter
7	momentum x [GeV]
8	momentum y [GeV]
9	momentum z [GeV]
10	Energy of the particle [GeV]
11	Mass of the particle [GeV]
12	vertex x [cm]
13	vertex y [cm]
14	vertex z [cm]

GEMC how many particles are in each event and the type of particle, its momentum and its vertex. For our purposes in BONuS12, we have Lund files with scattered electron-proton events that also have a number of additional protons that serve as background. The number of these background protons can vary, but the intent is always to best represent what we would expect to see. Once we run this file through GEMC with all the other variables defined that have been previously discussed, we need to take a look at what happens in the simulation when these protons travel through the RTPC.

4.3.3 DRIFT ELECTRONS

When protons travel through the sensitive region of the RTPC, they ionize the gas creating what are known as ionization electrons. Because of the electric field within that sensitive region, those ionization electrons drift toward the outer edge of the RTPC to the GEM foils and are detected by the readout electronics. Protons

traveling through the RTPC also bend in a helical pattern because of the magnetic field. The ionization electrons that are created bend as well, but in the opposite direction of the protons because they are oppositely charged.

By how much these charged particles bend when moving through the magnetic field created by the solenoid depends, in part, on the magnitude of that field throughout their path. Therefore, it is very important to get an accurate map (*ie.* the magnitude and direction of the field at small steps in space inside the solenoid) of that magnetic field. This is important for both the generation of simulated data and the reconstruction of real data. For the simulated data, the field map will define the path of both protons and ionization electrons within GEMC. For the real data, it will play a role in the reconstruction of kinematics from events.

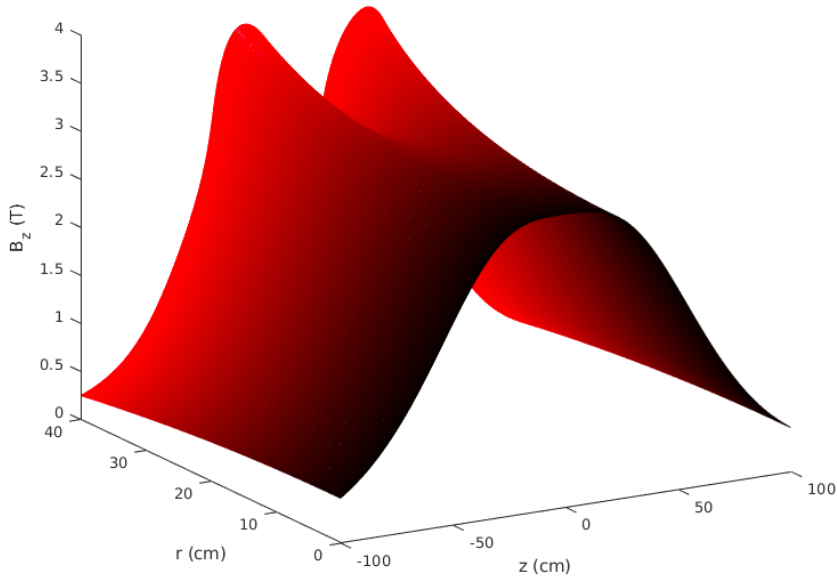


Fig. 36: CLAS12 Solenoid Field Map (courtesy of V. Lagerquist)

The field map for the solenoid magnet in CLAS12, in which the BONuS12 RTPC will reside, is mapped in steps of z and r (symmetric in ϕ) by Victoria Lagerquist at Old Dominion University (see Fig. 36). Within the sensitive region of the RTPC (*i.e.* $3 \text{ cm} \leq r \leq 7 \text{ cm}$), the B-field is shown in Fig. 37 *vs.* z . This magnetic field map allows for the detailed treatment of simulated charged particles in the solenoid, like protons traveling through the RTPC in GEMC.

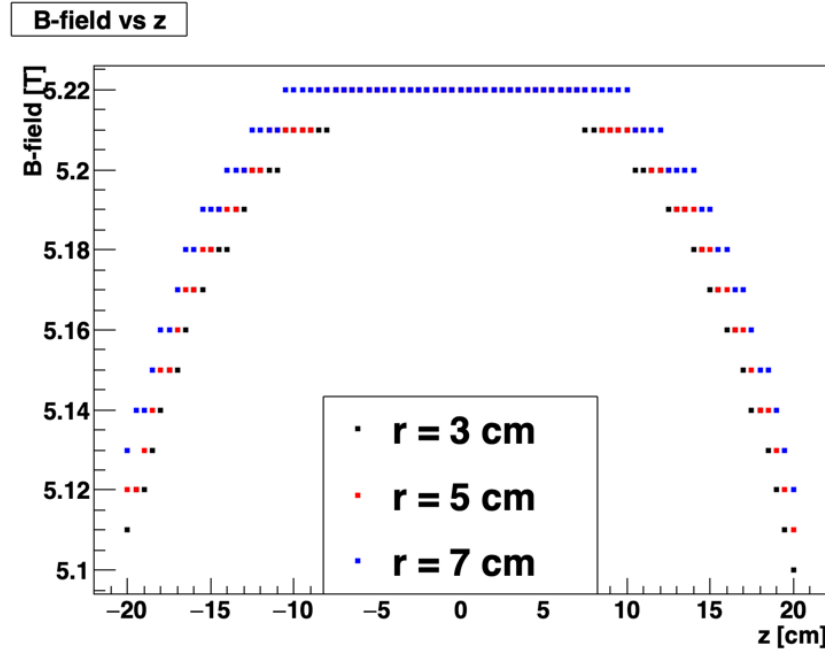


Fig. 37: Magnetic field strength versus z for values of r .

While GEMC does an acceptable job simulating the proton tracks, Garfield++ has a more specialized capacity to simulate the ionization electrons (also called drift electrons) created by the protons as they interact with the gas mixture as well as the electric and magnetic fields that are present in the sensitive region of the RTPC. The available build of Garfield++ does not allow for a magnetic field map to be imported, so it had to be written in as a custom feature.

By starting electrons at different values of r throughout the sensitive region (*i.e.* $3 \text{ cm} \leq r \leq 7 \text{ cm}$) and using known values of the electric and magnetic fields, Garfield++ calculated the time it takes that electron to reach the outer edge of the RTPC (*i.e.* 8 cm) as well as the change of angle that it makes. By defining more than one electron for Garfield++ to simulate, we can fit the resulting histogram of drift times and drift angles to Gaussians. The mean of the Gaussian fits serve as points in the graphs of drift times and drift angles. As the drift electrons go through the gas mixture, they collide with the molecules of that gas mixture. Therefore, the path of the drift electrons change each time an original ionization occurs.[44] This property is called diffusion of the drift electrons. The sigma of the Gaussian fits to the drift time and drift angle histograms defines the diffusion of the simulated drift

electrons. As we will see in the coming sections, these drift times and drift angles are of crucial importance to the BONuS12 experiment.

4.3.4 GAS OPTIMIZATION

One of the first uses for the drift time and drift angle from Garfield++ is to optimize the gas mixture that will be used in the sensitive region of the RTPC. We require a fast drift time to ensure our electronics are able to handle the signal within the available time window. This would also be less demanding on the trigger and usually means less diffusion. The other property to minimize (*i.e.* drift angle) would ensure that our track is discernible from others in the detector at the same time. Along this line is the need to minimize the diffusion that occurs within the RTPC in order to increase the resolution of the hits. Thus, we need a gas mixture that is fast, with small drift angle and diffusion properties, but with a high number of primary ionization events to reconstruct the track.

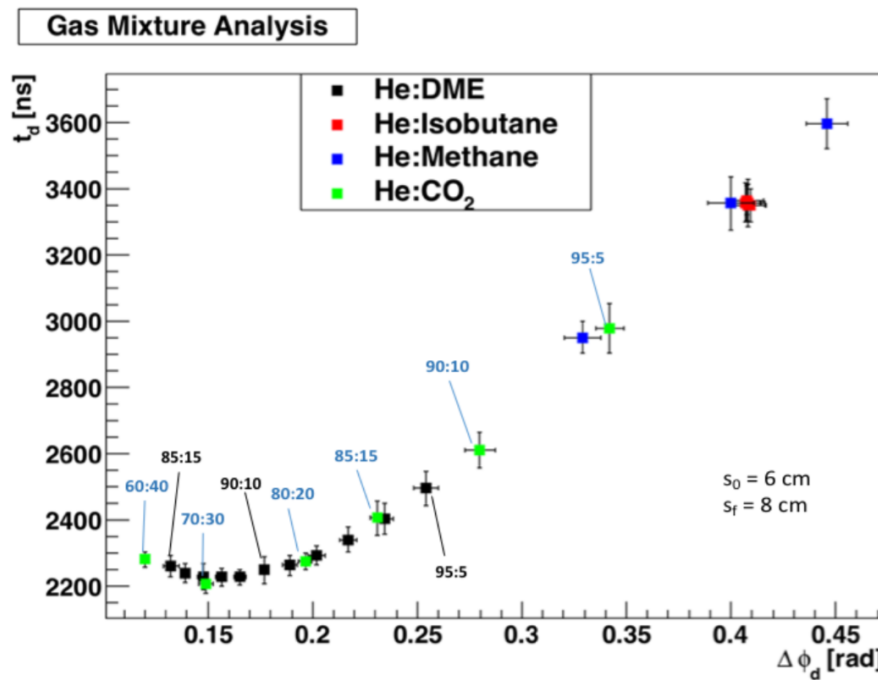


Fig. 38: Drift angle vs drift time for various gas mixtures. Only electrons created at $r = 6$ cm are included in this plot.

The purpose of mixing gases is two-fold. First, there must be a primary gas where primary ionization occurs. Typically this is chosen to be a noble gas such as

helium, neon, or argon. A noble gas is usually the primary gas because the outer electron level of the molecule is full (*i.e.* it has a closed shell), meaning the gas would not interact with the walls of the detector. Also, because the outer level is full, the probability of capturing a drift electron is low (*i.e.* they have a low electron affinity). Second, in order to prevent secondary effects such as photon feedback¹ and field emission², there must exist another gas to act as a quencher. This quencher gas is used to create a stable gas mixture that creates a signal well separated from noise of the electronics.

The first goal is to identify the type of quencher. Fig. 38 shows the drift time as a function of the drift angle of four gas mixtures in a sensitive region containing an electric field of 625 V/cm for electrons starting from 6 cm and ending at 8 cm. This electric field corresponds to a potential difference of -2500 V within the sensitive region, which is high enough to move ionization electrons to the GEMs, but lower than the breakdown potential of the gas (more about this in a few paragraphs). These initial and final radii were chosen to gather results quickly. The error bars on these points are the sigmas of the Gaussian fits of the histogram and represent the diffusion properties of the mixture.

All ratios of He-Isobutane result in almost identical drift angle and drift time. The He-DME starts with a ratio of 85:15 on the far left of Fig. 38 and goes to 100:0 on the far right. The mixture of 87:13 He:DME is at the minimum of the curve. Ideally, as in the original BONuS6 experiment, we would choose this He-DME mixture. However, in an effort to chose a non-flammable gas, we decided to take a look at He-CO₂ mixtures.

In Fig. 38, the He-CO₂ mixture is in green with the ratios labeled in blue. The 70:30 mixture is at the minimum drift time, which certainly meets the criteria for BONuS12. During a run we need to monitor the gas mixture. If we choose to be at the minimum, then identifying when a change occurs would be difficult. This is because while there may be a change in drift angle as the ratio changes, at the minimum the drift time changes are on the order of nanoseconds. If 80:20 is chosen, then we can more easily identify if a change happens during a run by the noticeable change in both drift angle and drift time. For this reason, as well as its non-flammability, we use a gas mixture of 80%:20% He:CO₂.

¹Secondary avalanches created from decay through photon emission of excited primary gas atoms.

²Electrons emitted from an electric field.

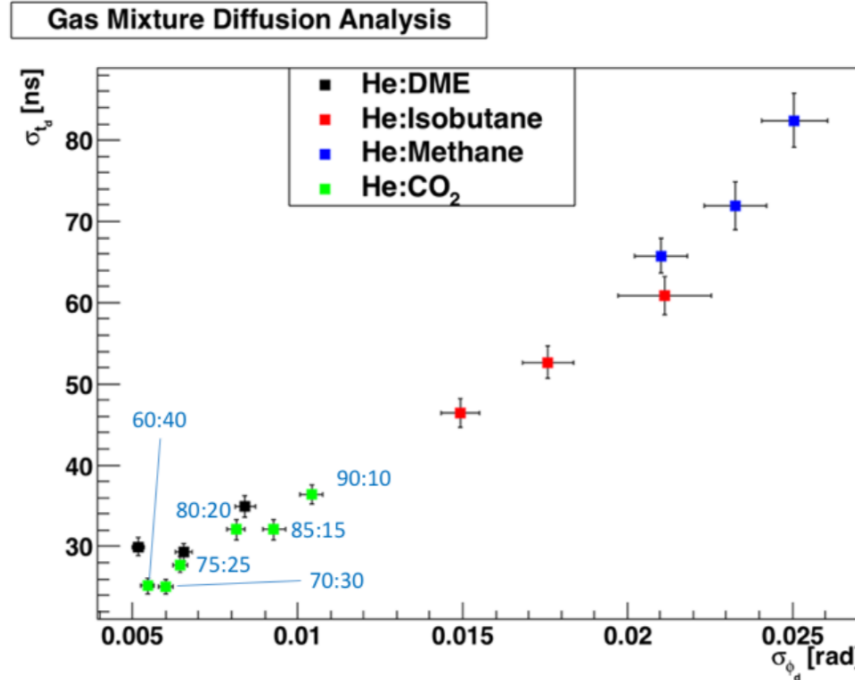


Fig. 39: Diffusion in drift angle vs diffusion in drift time for various gas mixtures.

Now we must look at reducing diffusion effects for this mixture or at least understand what those effects are for our chosen mixture and potential. If we look at a plot of the diffusion in ϕ (σ_{ϕ_d}) as a function of diffusion in time (σ_{t_d}), as shown in Fig. 39, we see that the mixtures of He-CO₂ with ratios of 80:20-75:25 rival those of He-DME. Given this plot alone, it can be concluded that mixtures containing 60-75% helium do better than the He:DME mixtures.

The next step in this optimization is to look at the potential within the sensitive region of the RTPC. Here, note that preliminary experimental studies showed that the maximum voltage on the cathode would be about -4000 V for He-CO₂. These studies were done with a flat prototype, so if we include that the cathode will be cylindrical, the potential may need to be less. Fig. 40 is a plot of He-CO₂ mixtures for potentials of -2500 V, -3500 V, and -4000 V. Again, the error bars represent the diffusion properties of the mixtures, which comes from the sigma of the Gaussian fit to the histogram. As one would expect, the higher the potential, the faster the drift time and the smaller the drift angle.

Given all of this information and the requirements of the detector, we chose a gas

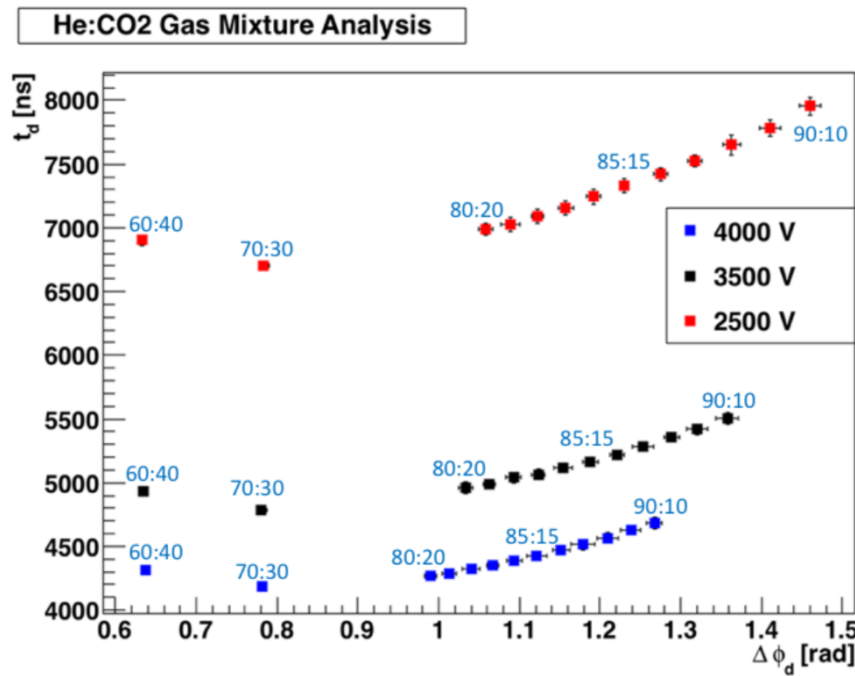


Fig. 40: Drift time versus drift angle for He:CO₂ using various potentials.

mixture of helium-carbon dioxide with a ratio of 80:20 at -3500V. The mixture He:CO₂ meets the requirement of being fast with a small drift angle. For low momentum ions, such as protons in the case of the BONuS12 experiment, reducing multiple scattering is accomplished with low-mass gas mixtures. Thus He-CO₂ is ideal. The CO₂ in the mixture does not serve so much as a quencher, since helium essentially acts as its own quencher, but does limit the diffusion that occurs within the region. In addition, CO₂ is nonflammable.

4.3.5 DRIFT EQUATIONS

By knowing the drift time and drift angles of electrons starting at various values of r and z , we can plot the points and fit the points to an equation. These fit equations can be seen in the plots of t_d vs. r and ϕ_d vs. r (*i.e.* Fig. 41a and Fig. 41b, respectively). We can then use these equations in GEMC to find the drift time and drift angle of a drift electron created at any point along the path of the proton in the sensitive region of the RTPC. In order to speed up simulation efforts, simulation electrons were created at $r = 3$ cm to $r = 7$ cm at 0.5 cm increments and $z = -19$

cm to $z = 19$ cm at 5 cm increments. This give us 81 data points to work with (*i.e.* 9 points per fit line).

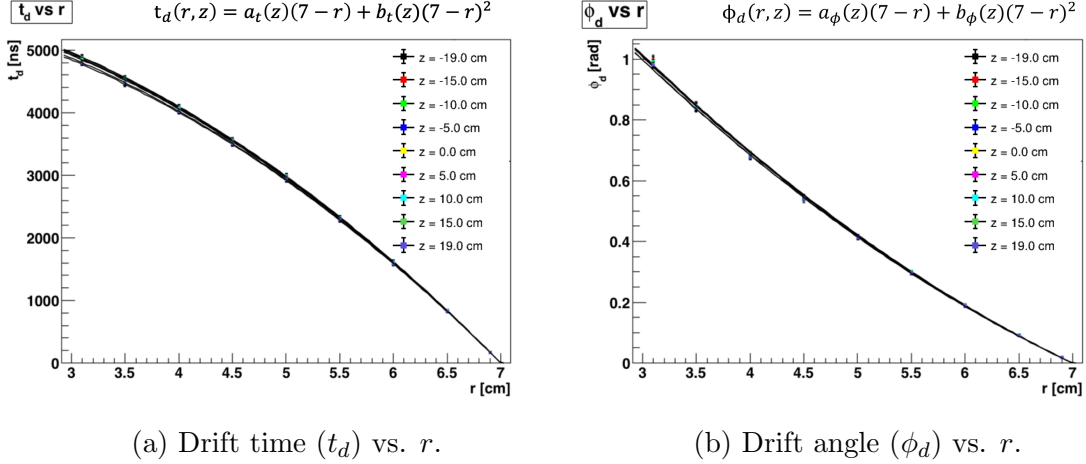


Fig. 41: Plots of drift electron properties.

The 9 points for each value of z are fit to a second-order polynomial whose coefficients a and b depend on z . This is because the magnetic field changes with z , as shown in Fig. 37, for three values of r that are within the sensitive region of the RTPC. For each of the fit lines, or values of z , we extract the values of a and b for both drift time and drift angle. These values are shown in Fig. 42 as a function of z and are then fit to fourth-order polynomials because of the shape of the magnetic field (see Fig. 37):

$$\begin{aligned} a_\phi(z) &= a_{\phi 0} z^4 + a_{\phi 1} z^3 + a_{\phi 2} z^2 + a_{\phi 3} z + a_{\phi 4}, \\ b_\phi(z) &= b_{\phi 0} z^4 + b_{\phi 1} z^3 + b_{\phi 2} z^2 + b_{\phi 3} z + b_{\phi 4}, \\ a_t(z) &= a_{t0} z^4 + a_{t1} z^3 + a_{t2} z^2 + a_{t3} z + a_{t4}, \\ b_t(z) &= b_{t0} z^4 + b_{t1} z^3 + b_{t2} z^2 + b_{t3} z + b_{t4}. \end{aligned} \quad (83)$$

These equations and parameters go into the `rtpc_hitprocess` class of GEMC. Therefore, when an ionization occurs in the simulation, GEMC uses those equations in Fig. 41b and Fig. 41a to calculate the position of the ionization electron when it reaches the outer edge of the RTPC.

4.4 DMS SIMULATIONS

As we have seen in the previous sections, the drift of the ionization electrons in the RTPC is very sensitive to the gas mixture, temperature, pressure and potential. The

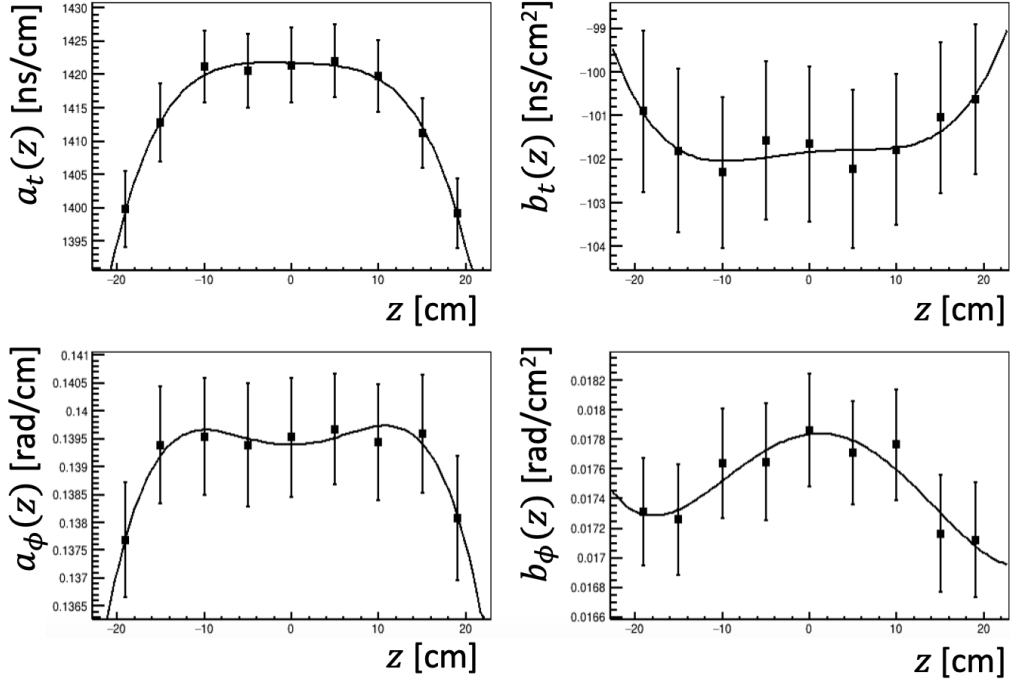


Fig. 42: Parameters a and b for drift angle (a_ϕ and b_ϕ) and drift time (a_t and b_t).

Drift-gas Monitoring System (DMS) was constructed to measure any fluctuations in those parameters of the gas by way of measuring drift velocity (see Section 3.3.3). In order to do that, simulations of the DMS had to be done to optimize the uniformity of the electric field within the drift region as well as the geometry of the chamber itself.

4.4.1 GEOMETRY

The parameters of interest to investigate and optimize were the anode diameter, diameter of the electrodes, and the distances between components. In order to look at these parameters, the geometry of the DMS was implemented into Garfield++, which consisted of its rectangular frame, grounded anode enclosure, anode wire, cathode plate, and field-shaping electrodes. The specifications of these components can be found in Appendix A, which contain the engineering drawings of the DMS.

The first step is to define the gas mixture and geometry of the box used to house all of the DMS components. By using the **Sensor** class in Garfield++, the framework and wires necessary to see the DMS response was built. Then, as seen in the code

snippet within Appendix B, grounded planes were placed along the box. Next, the anode/ground plate surrounding that wire was defined. The following code snippet shows the anode wire defined by a single declaration.

```
// Anode
comp->AddWire(x_0 + r_a + wall_d/2., L_y/2, dAnode, vAnode, "a", 100.,
50., 19.3);
comp->AddReadout("a");
sensor->AddElectrode(comp, "a");
```

The ground plate surrounding the anode was constructed from a number of large-diameter grounded wires that were placed to form the shape of that plate, since Garfield++ has difficulties with these rather complicated structures. The same was done for the cathode plate, which used two layers of wire components. The electrode wires were all placed individually, with one example in the code snippet below.

```
comp->AddWire(dist, L_y/2.+b/2.+(i*s_y), dWire, Ex*(s_1 + (j*s_x)), name,
100., 50., 19.3);
comp->AddReadout(name);
sensor->AddElectrode(comp, name);
```

The function `AddWire(double x, double y, double D, double V, string label, double L, double T, double rho)`, places the wire at `x` and `y` with diameter `D`, potential `V`, label of the wire, length `L`, tension `T`, and density `rho` in that order. This placement was repeated 60 times completing 10 rows of electrodes with 6 wires comprising each electrode.

4.4.2 ELECTRIC FIELD

Once the geometries and code were in place, simulations were done to optimize both the geometries and the sensitive region. The primary concern was ensuring near-homogeneity of the electric field within the sensitive region. In order to look at that electric field, we need to look at the field profile along the plane where the anode lies.

Fig. 43 shows the contour map of the electric field, whose values are on the right legend. The plot in Fig. 43 is made using the `FieldView()` class. The potential from the cathode through to the electrodes was set to mirror what the electric field would

be inside the RTPC (*i.e.* 875 V/cm). The profile of the field along the line at $y = 3$ cm is shown in Fig. 44 and Fig. 45 shows a zoom in to between the two sources to ensure its homogeneity (*i.e.* a straight line). These plots are created using the `PlotProfile()` function of the `FieldView()` class.

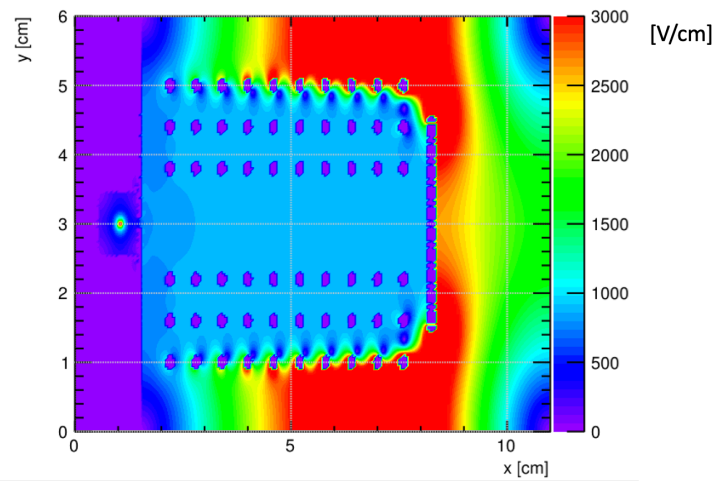


Fig. 43: Electric-field contour map along the cross-section in $x - y$ plane.

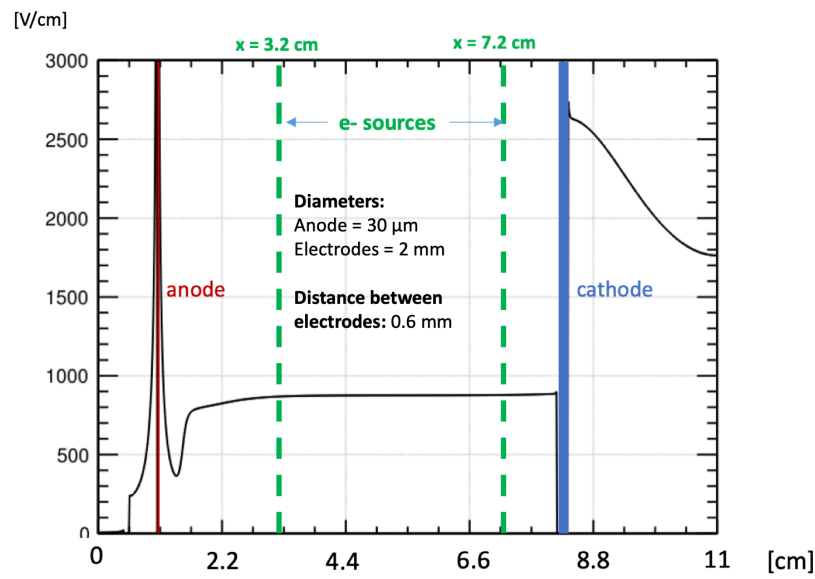


Fig. 44: Electric-field profile along the plane of the anode. The cathode and anode's locations are denoted as blue and red lines respectively. The sources and PMT's location and subsequent electron beams are pictured as green dotted lines.

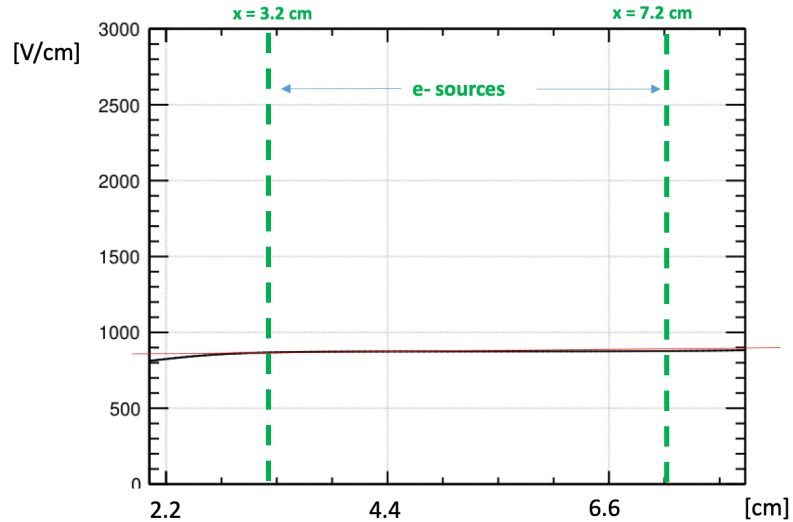


Fig. 45: Zoomed in electric-field profile to between the two sources. The cathode and anode's locations are denoted as blue and red lines respectively. The sources and PMT's location and subsequent electron beams are pictured as green dotted lines.

To achieve this straight line indicative of homogeneity, many simulations took place varying the electrode diameter and distance. The progression of these simulations can be seen in Figs. 46-48, beginning with small diameter electrodes (*i.e.* 50 μm) and a distance of 1.2 mm between each electrode (see Fig. 46). The small diameter coupled with the rather large distance between electrodes creates the large waves of field, which is not at all homogeneous. Fig. 47 shows the field profile with thicker electrodes (*i.e.* 1 mm), but the same separation as Fig. 46 (*i.e.* 1.2 mm). The waves of the field seem to be calmer, but still inhomogeneous.

Lastly, in Fig. 48, the electrode diameter was set to 2 mm and the distance between electrodes was decreased to 0.6 mm. The field here in between the sources is nearly homogeneous. Fig. 45 is zoomed in to that area between sources to verify how flat (*i.e.* homogeneous) the field is there.

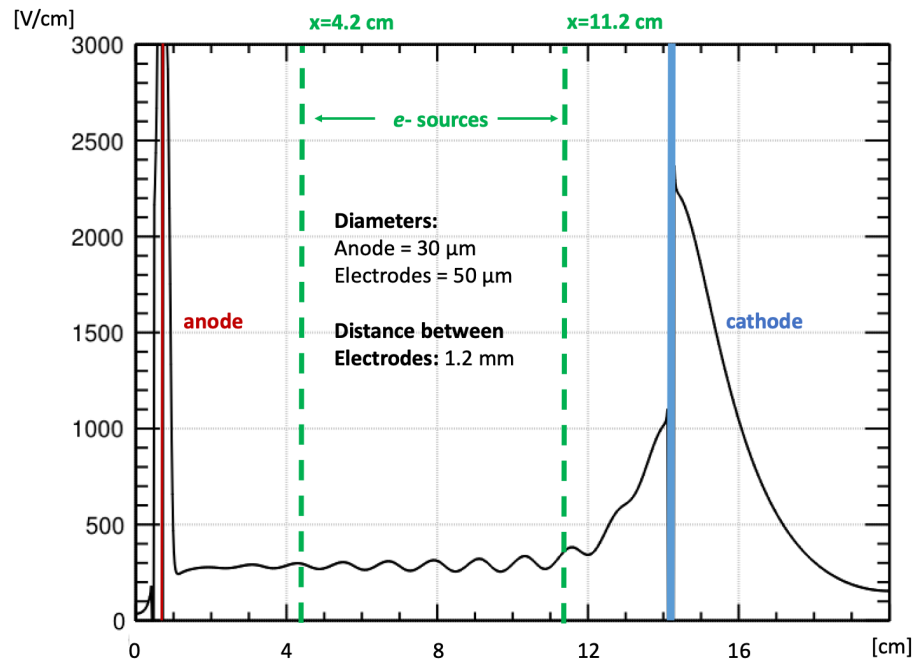


Fig. 46: Electric field profile with electrode separation of 1.2 mm and diameter of 50 μm .

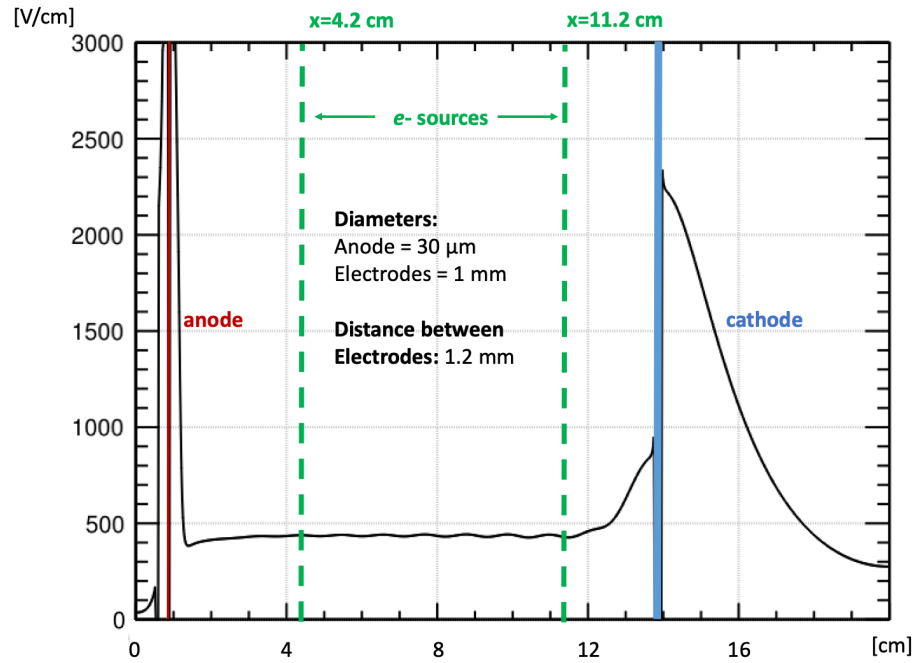


Fig. 47: Electric field profile with electrode separation of 1.2 mm and diameter of 1 mm.

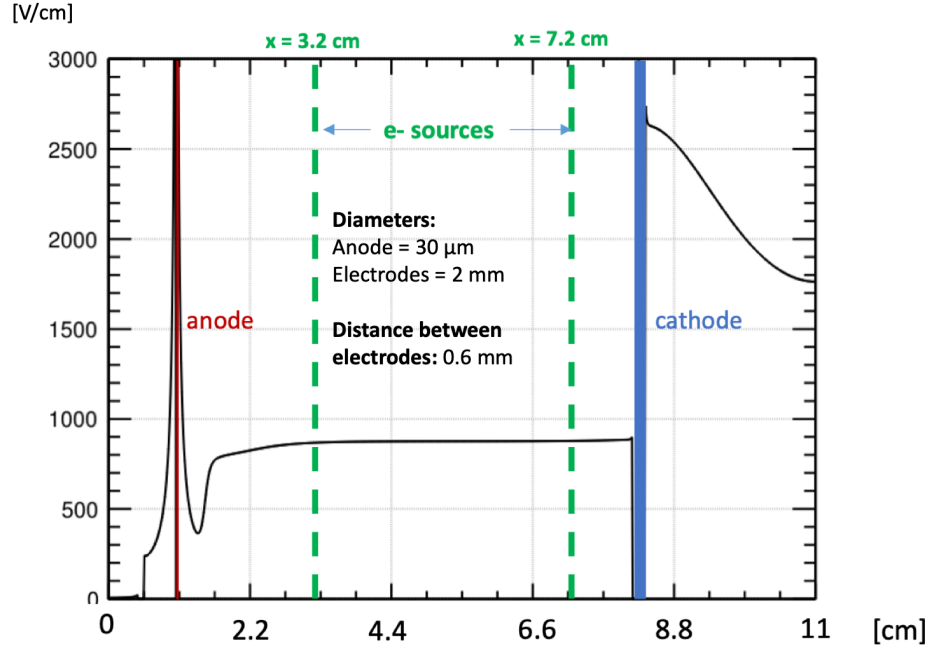


Fig. 48: Electric field profile with electrode separation of 0.6 mm and diameter of 2 mm.

Because of these simulations, we were able to identify the frame size, electrode and anode wire diameter, and distances between components. The distance between the cathode and the first set of electrodes was also chosen to be 0.6 mm, which also is the distance from the last electrode to the ground plate.

4.4.3 DRIFT VELOCITY

The last step of the Garfield++ simulations is to determine what we should expect for a drift velocity from the DMS. Just like the physical DMS, the drift velocity is calculated by finding the drift times from ionization electrons created in the sensitive region by primary electrons from the radioactive sources. In the simulations, electrons are started at one of the two areas where the sources would exist. From here the simulation tracks them toward the anode, and a histogram of the drift time is filled.

Fig. 49 shows the drift times from 20 ionization electrons created in the sensitive region on the line between each source and its associated PMT. By taking the means from both Gaussian fits of each collection of drift times with the distance between the two sources (*i.e.* 4 cm), the drift velocity can be calculated. That drift velocity

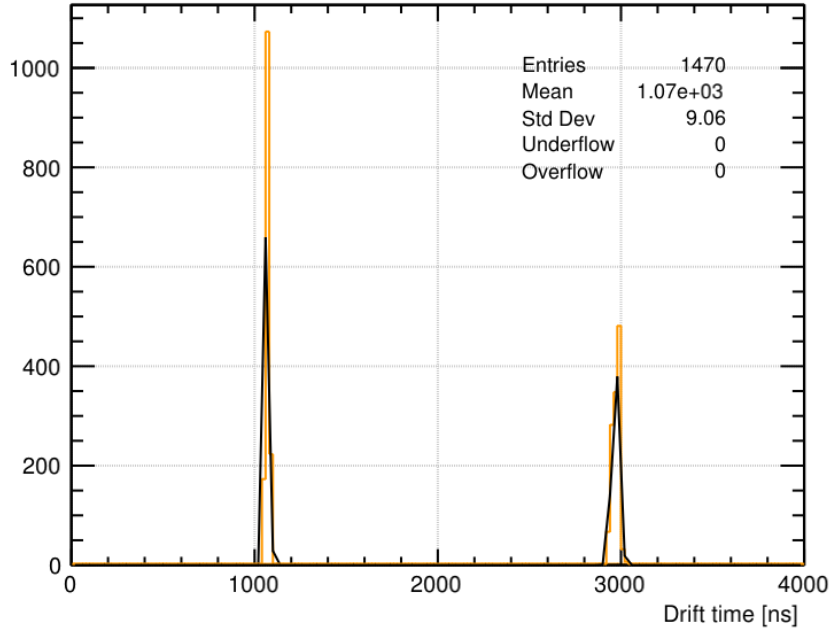


Fig. 49: Simulated drift time for ionization electrons created by radiation electrons from the near and far sources to the anode. The gas mixture is 80:20 He:CO₂ with a cathode potential of -6 kV and an anode potential of +1800V.

from Garfield++ simulations is

$$v = \frac{\Delta d}{\Delta t} = \frac{d_f - d_n}{t_f - t_n} = \frac{4 \times 10^4 \mu\text{m}}{2969.90\text{ns} - 1070.75\text{ns}} = 21.06 \mu\text{m/ns}. \quad (84)$$

This gave us an idea what to expect when beginning the data acquisition process.

CHAPTER 5

DATA ANALYSIS

The first production run at JLab’s Hall B after the completion of the 12 GeV upgrade was called Run Group A (RGA). It ran over the fall of 2018 and spring 2019 with billions of events and 2 pB of data accumulated,[45] The beam energy for the run was 10.6 GeV incident on a 5 cm long liquid hydrogen target at a current between 5 nA and 75 nA. Because this was the first set of data coming from CLAS12 detectors, it serves as an important test of our procedures, calibration, and analysis.

This chapter will outline the software tools used for turning raw data into usable data sets, including detector calibrations done to correct the raw data. Additional data analysis steps to extract inclusive deep inelastic cross scattering (DIS) sections are then described. Fiducial cuts were applied to eliminate inefficient areas of individual detectors, PID cuts were done to ensure e^- selection, and kinematic cuts were applied to select DIS events. The resulting data were binned in x and y (where $y = \nu/E$) to find the acceptance and calculate the inclusive DIS cross section. Finally the results were compared to the well-established Christy-Bosted parameterization of previous data.[46]

5.1 CLAS12 OFFLINE SOFTWARE

The raw data coming from each detector first enters into the Readout Controller (ROC) [39] and then gets stored in the EVent Input Output (EVIO) format. EVIO is a data format that is designed and maintained by the JLab Data Acquisition Group. Once that data is available for off-line use, it requires decoding. Decoding is the process of taking EVIO raw data and converting it to High Performance Output (HiPO) format.

The HIPO format provides for a flexible data container structure, and minimizes disk space by utilizing LZ4 data compression (the fastest compression method currently available). In each HIPO file, data is stored as individual records with adjustable size. Each record is compressed, with a tag associated with it, and a pointer to it is stored in the file’s index table. For analysis this provides users with faster analysis by reading portions of the file depending on the final states to be analyzed.

Once the data is in HIPO format, it is ready to be reconstructed and analyzed. The CLAS12 event Reconstruction and Analysis (or CLARA) framework.[45] allows users to reconstruct physics events and analyze the files to yield usable physics data. CLARA does this by utilizing a service-oriented architecture to enhance agility, efficiency, and productivity of the software components within the CLARA framework. During the reconstruction process, the raw data from all detectors is taken in and processed by the corresponding packages. The main packages in CLARA are for *geometry, calibration constants, magnetic fields, particle swimming, and plotting/-analysis.*

The geometry tools were created due to the complexity of the CLAS12 detector subsystem geometries. The library contains primitives that represent all of the lines, planes and shapes of all the detectors. The tools provide methods to track particles through the different volumes for evaluation of track trajectories, such as line-to-surface intersections, ray tracing through objects, and evaluation of the distance of closest approach to a line or surface. Because subsystem parameters can change from run group to run group and sometimes even within a run group, time-dependent geometry variations exist that allows for consistency between simulation, reconstruction, and event visualization packages.

The Calibration Constants Database was originally developed at JLab for the GlueX Experiment in Hall D and renamed the CLAS12 Constants Database (CCDB). It was adopted by the CLAS12 collaboration because of its functionality for storing and accessing structured tables. At the decoding stage, both file formats and data structures change. Signals are converted from hardware notation (*i.e.* crate, slot, channel) to CLAS12 notation (*i.e.* sector, layer, component).[45] Then during reconstruction, the time stamps of these databases are utilized in order to access run-specific constants. Because the constants change from run to run, CCDB contains constants for each run. The CLAS12 software tools employ an Application Programming Interface (API) that parses CCDB tables to create structured maps of the constants stored in memory by sector, layer, component. This method allows for fast retrieval of only the relevant constants.

Magfield, the magnetic field package for CLARA, consists of field maps created from engineering models of the solenoid and torus magnets in CLAS12. These field maps contain a header with meta-data describing field pedigree, its grid coordinate system, and the coordinate system of the field components. For example, the CLAS12

torus has a cylindrical grid, but Cartesian field coordinates. *Magfield* uses trilinear interpolation of the field, which is a multivariate interpolation on a three dimensional rectangular grid.[45] Because the field is often accessed within a sequence of points all contained within a single grid, *magfield* uses time-saving software probes to cache nearest neighbors.

To propagate charged particles through the CLAS12 magnetic fields in order to confirm tracks, the *swimmer* package is used in parallel with the *magfield* package. Swimmer uses a fourth-order adaptive-size Runge-Kutta integrator with single step advancement achieved by a configurable Butcher tableau advancer.¹ The purpose of swimming particles with this toolkit is to propagate particles to a given plane, to the closest point on a line, or to a given (x, y, z) coordinate. Performance is improved for forward propagation in CLARA by reducing the dimensionality of a state vector that contains the main track parameters, by changing from the path length independent variable to the coordinate along the beamline, which defines the nominal CLAS12 z -axis.

Finally, the plotting and analysis tools can be used for further data calibration, monitoring, and analysis. The toolkit was developed in the Java programming language and the interface is similar to the ROOT platform developed at CERN for high-energy physics analysis. The plotting package, called *groot*, allows for histogram and graph creation, filling and manipulation. Plot fitting can be done using the Java-based MINUIT² library available in the Journal of High Energy Physics (JHEP) repositories.

Once the information about particle tracks is collected, that information is passed to a service called the Event Builder (EB). The EB takes the results from the upstream services and correlates the information from the CLAS12 subsystems. To form charged particles from the data, EB matches geometric coincidences in the distance of closest approach (DOCA) between detector responses and tracks. The event start time is important for all time-based particle identification and is determined from the optimal charged particle candidate in the Forward Detectors with an associated Forward Time of Flight (FTOF) timing response. The last step in the EB is particle identification (PID). For our purposes, we are only concerned with e^- identification. This e^- PID is largely done through calorimetry and Cherenkov information. If the

¹Butcher tableau is the summary of the Runge-Kutta method used

²MINUIT is a numerical minimization program developed by Fred James at CERN in the 1970's

measured energy deposition in the ECAL is consistent within 5σ of the expected value of the sampling fraction (see Section 3.2.5), and the photoelectron response in the HTCC is consistent with $\beta \approx 1$, then the particle is assigned to be an electron or positron depending on the track curvature in the DC.

5.2 CALIBRATION

Once the raw data is decoded and reconstructed, it can be analyzed. However, initial analysis must be dedicated to detector calibration. Calibration is done for each detector and even for each run so that the experimental quantities like time and energy are correctly extracted from raw TDC and ADC data. Just as in the RTPC, drift times and distances of electrons in the DC are subject to the properties of the gas (*i.e.* pressure, temperature, gas mixture, etc.). These changes determine calibration constants for the drift chambers (DC), just as they do for the RTPC. Time-of-flight (TOF) calibration constants depend on cable lengths, detector geometry and other factors related to the detector and electronics. The calibrations of individual detectors have been done by a large group of CLAS12 collaborators. Those calibration efforts will be briefly discussed, focusing on the detectors relevant to this analysis.

The order of calibrating the detectors was important since some calibrations rely on the proper calibrations of other detectors. The first was the DC calibration, which consists of two steps. The first step is understanding the various fixed-time delays due to cable delays and trigger latency. The second is calibration of the distance to time function, which enables the time of arrival of a signal on the DC sense wire to be converted to a distance from the sense wire. This relied on a crude start time (few ns level) calibration of the FTOF. Next, the FTOF was calibrated more precisely with central time-of-flight (CTOF) detector time matching.³ FTOF timing calibrations employed PID from the Event Builder (EB), and defined the start time using the electron in the electromagnetic calorimeter (EC), positron in the EC, or high-momentum pion in the DC/FTOF.

Once the DC and FTOF were properly calibrated, CLAS12 subsystems were

³Time matching is the process of matching a time predicted from particle swimming to arrival time of the particle in a particular detector. For example, if a particle appears in the CTOF, then the time it will arrive in the FTOF can be calculated. If a particle arrives in the FTOF that matches that time along with the other criteria, it is identified as the same particle that appeared in the CTOF.

calibrated. This included central neutron detector (CND), CTOF, EC, forward tracker (hodoscope and calorimeter), high-threshold Cherenkov counter (HTCC), low-threshold Cherenkov counter (LTCC), and ring imaging Cherenkov hodoscope (RICH). Timing calibrations for all subsystems relied on PID from the EB and start time from the FTOF. After subsystem calibration was complete, the data was reconstructed again using the new CCDB parameters.

Run	Torus	Solenoid	$\langle i \rangle$ [nA]	E_{beam} [GeV]	Run Range
4903	-100%	-100%	45	10.6	4763-5031
5038	-100%	-100%	45	10.6	5032-5189
5197	-100%	-100%	45	10.6	5190-5285
5306	-100%	-100%	45	10.6	5286-5419

TABLE III: Summary of calibrated runs for Run Group A. The run number on the far-left column is the run that represents the calibration constants for the run range on the far right.

The resulting calibrations can be summarized in Table III, where a specific run (far-left column) was selected that represents the same run conditions for the run range (far-right column). The required specifications for calibration were generally met. Beginning March 2020, RGA Pass1 (first official run through CLARA with updated calibration constants) decoding and reconstruction began, which required an enormous amount of computing resources. This first pass only includes inbending (Torus at -100%) data. The calibration for outbending (*i.e.* Torus at +100%) is ongoing.

5.3 CHRISTY-BOSTED MODEL AND MC SIMULATED DATA

The simulated data (5M events) was generated in GEMC (see Section 4.1) using the same detector setup as Run Group A. The event generator used as input to GEMC utilized the Christy-Bested fit [46] to previous data. The Christy-Bested empirical fit to measurements of the inclusive inelastic electron-proton cross section covers a wide kinematic range of four-momentum transfer $0 \leq Q^2 < 8$ GeV 2 and final state invariant mass $1.1 < W < 3.3$ GeV. It utilized 6 different data sets and includes EMC effect (see Section 2.9) corrections. Fig. 50 shows the fit in red and existing data as black triangles.

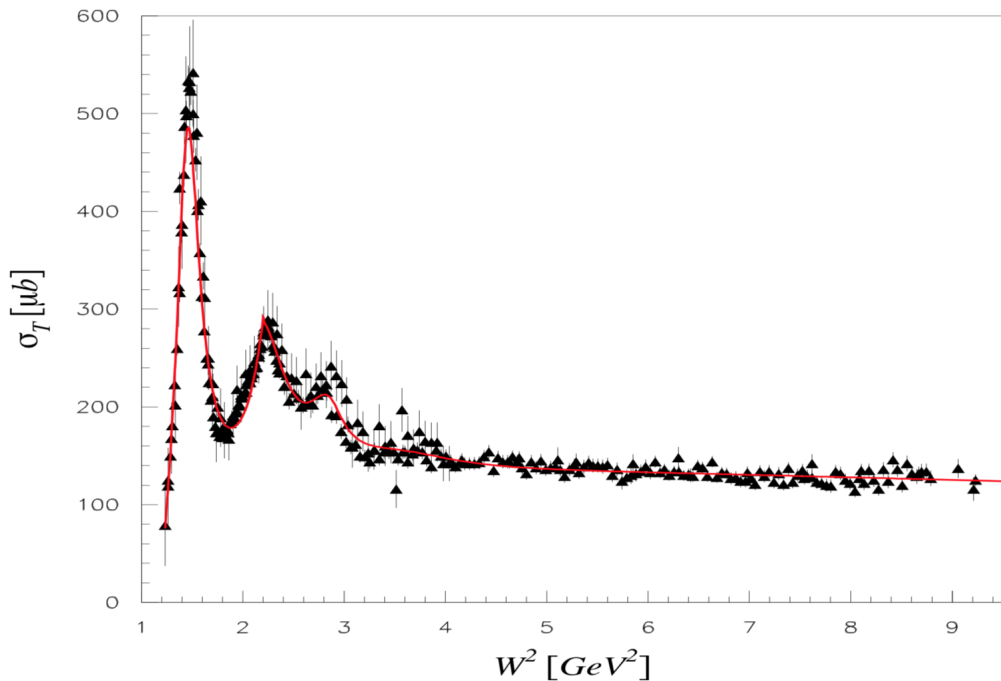


Fig. 50: Total cross section vs. W^2 for existing data (black triangles) and the Christy-Bosted fit in red [46].

The event generator uses the cross sections from the Christy-Bosted fit to create input files in LUND format that contain events from the inclusive DIS reaction $ep \rightarrow e'X$. Those LUND files are inputs to GEMC, which propagates the particles from the LUND file through the CLAS12 detectors to create raw Monte Carlo (MC) data. That data is then decoded and reconstructed using the same CLARA software as the RGA data.

5.4 FIDUCIAL CUTS

Each detector has limits where it cannot efficiently detect particles. The edges of detectors are particularly vulnerable to inefficient and inconsistent particle detection. The goal of placing fiducial cuts on detectors is to remove from the data set events that are detected in areas of low or unknown efficiency. The Event Builder in CLARA does make cuts on detectors and kinematics in order to ensure the particle identification is efficient and the event occurs within the target area, with proper response in the forward detectors.

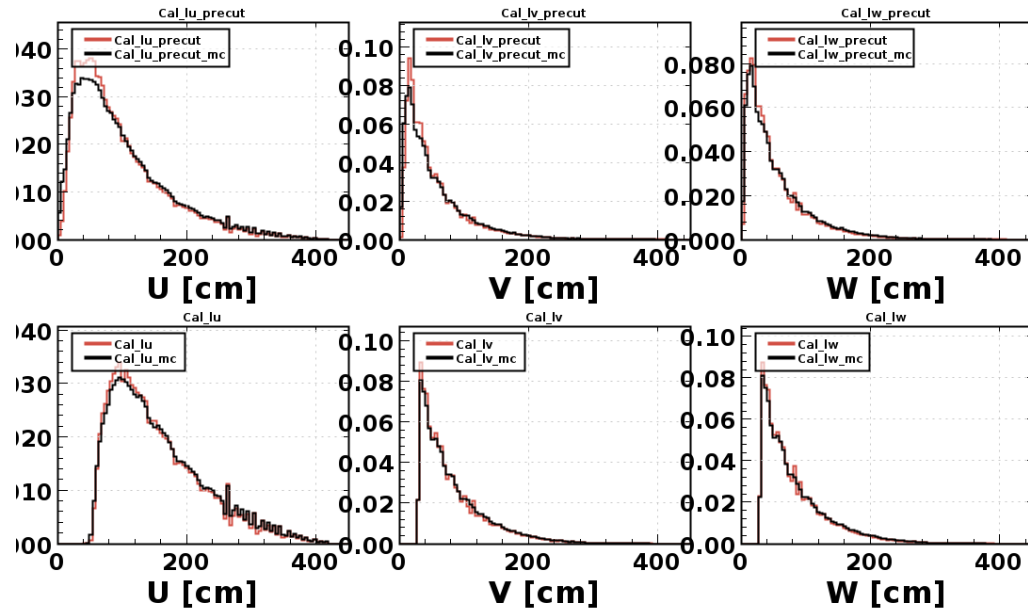


Fig. 51: Count distributions of the U , V , and W dimensions of the pre-shower calorimeter (PCAL). The raw histograms are on the top and the bottom histograms contain the cuts: $U > 30$ cm, $30 < V < 390$ cm, and $30 < W < 390$ cm. All plots are normalized to account for any mismatch in total statistics. Red lines are from RGA data and black lines are for the Monte-Carlo (MC) data.

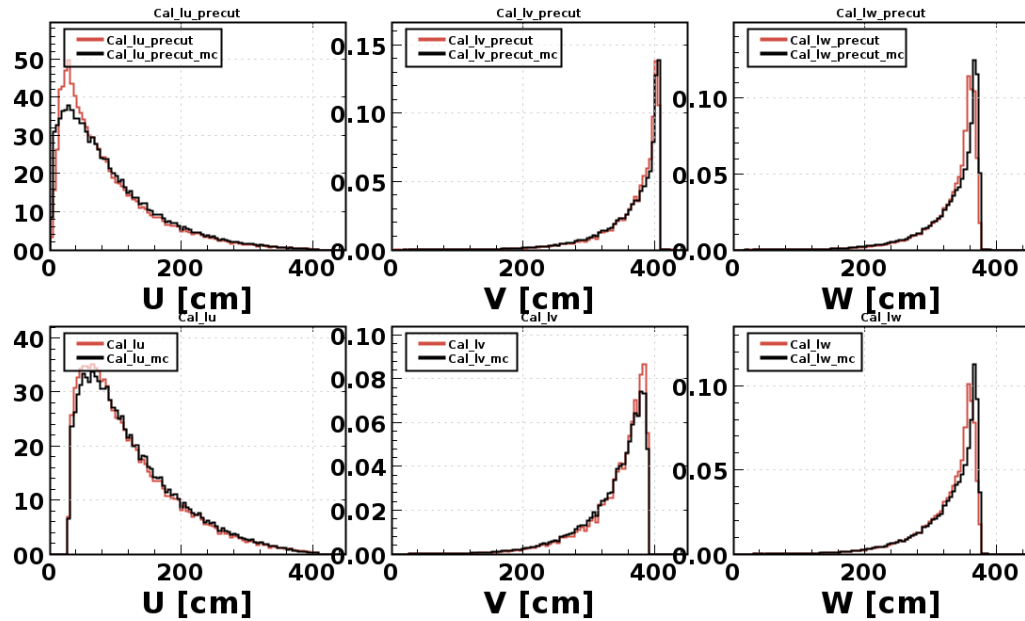


Fig. 52: Count distributions of the U, V, and W dimensions of the inner EC. The raw histograms are on the top and the bottom histograms contain the cuts on the PCAL: $U > 30$ cm, $30 < V < 390$ cm, and $30 < W < 390$ cm. All plots are normalized to account for any mismatch in total statistics. Red lines are from RGA data and black lines are for the Monte-Carlo (MC) data.

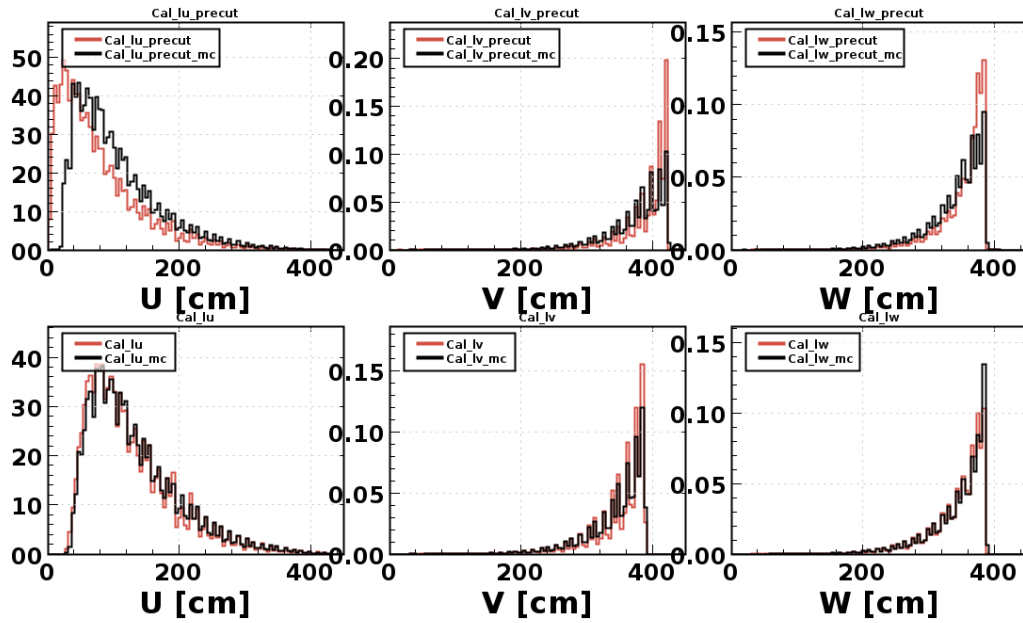


Fig. 53: Count distributions of the U, V, and W dimensions of the outer EC. The raw histograms are on the top and the bottom histograms contain the cuts on the PCAL: $U > 30$ cm, $30 < V < 390$ cm, and $30 < W < 390$ cm. All plots are normalized to account for any mismatch in total statistics. Red lines are from RGA data and black lines are for the Monte-Carlo (MC) data.

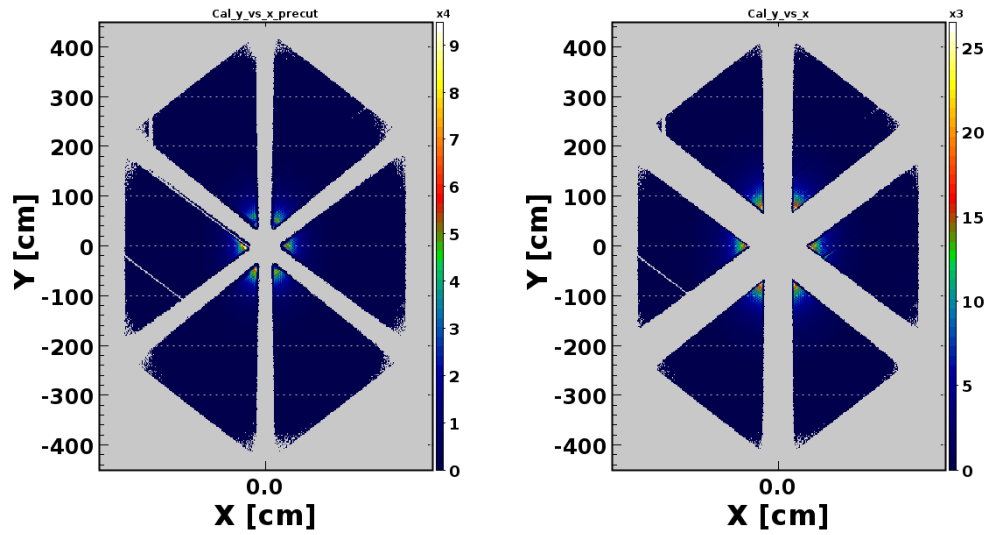


Fig. 54: 2D histograms of the uncut PCAL hits on the left and after the fiducial cuts are applied (right).

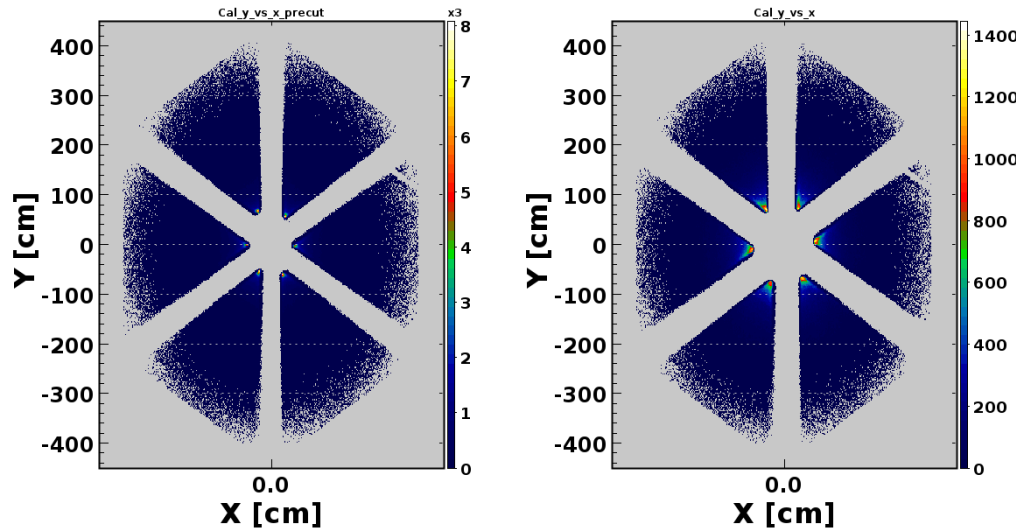


Fig. 55: 2D histograms of the inner EC hits. On the left is before cuts on the PCAL, and on the right is after the fiducial cuts on the PCAL are applied.

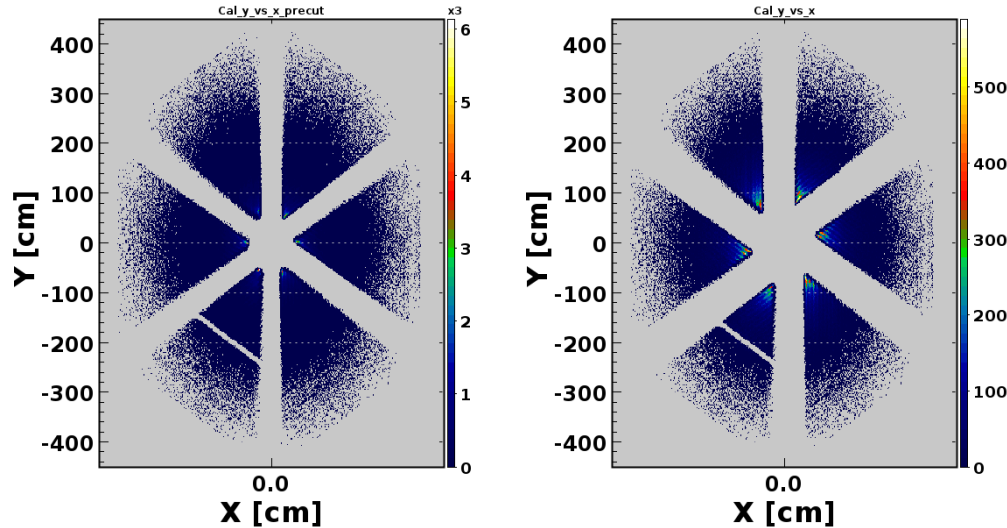


Fig. 56: 2D histograms of the outer EC hits. On the left is before cuts on the PCAL, and on the right is after the fiducial cuts on the PCAL are applied.

The EC is the detector that we use for determining the scattered electron energy and all kinematics that are calculated from that energy. When electrons enter the EC they shower and stop. That EM shower is broad, so we have to remove events close to the edges since the total energy deposited is unreliable for e^- identification in those cases. The Event Builder makes an $E_{\text{PCAL}} > 60$ MeV cut on the PCAL energy and a $-15 < v_z < 15$ cm vertex cut.

Remember that an EC detector is defined by U, V, and W edges of its triangular shape (see Section 3.2.5). We can cut on those edges for the PCAL only and the effects will propagate through to the EC_{inner} (ECin) and EC_{outer} (ECout) detectors. The established cuts for the PCAL are $U > 30$ cm, $30 < V < 390$ cm, and $30 < W < 390$ cm. Fig. 51 shows the count distributions of the U, V, and W sectors of the PCAL. Fig. 52 shows the count distributions of the inner EC and Fig. 53 shows the count distributions for the outer EC. For Figs. 51-53 the uncut histograms are on the top and the bottom histograms contain the PCAL cuts that were described. Fig. 54 contains the two-dimensional histograms of the uncut PCAL hits on the left and the 2D histogram containing the fiducial cuts on the right. Fig. 55 and Fig. 56 show the 2D histograms for the inner EC and outer EC, respectively, with the uncut plots on the left and plots including PCAL cuts on the right. It is clear that there are less electrons that make it through the inner EC than the PCAL, and not as many make it through the outer EC than the inner EC.

5.5 KINEMATIC AND PID CUTS

Our goal is to extract the inclusive DIS cross section for the process $ep \rightarrow e'X$, which means that certain constraints must be put on some of the kinematic variables. To isolate DIS events, we select $W > 2$ GeV and $Q^2 > 1$ GeV². In order to isolate events that originate at the target, we require -10 cm $< v_z < 10$ cm, where v_z is the z-vertex position of the track. Fig. 57 shows v_z before (left) and after (right) cuts. It is clear that a -15 cm $< v_z < 15$ cm cut was made during reconstruction.

The last significant cut occurs on the sampling fraction. The sampling fraction is defined as E_{tot}/p , where E_{tot} is the total energy deposited by the particle in both layers of the EC (*i.e.* inner and outer EC) and p is the particle's momentum as measured by the drift chambers. When the sampling fraction is plotted vs p , electrons will appear as a band around 0.25 E_{tot}/p . A selection of momentum above 1 GeV was applied to eliminate any minimum ionizing particles like pions (see Fig. 58). To select events near the band at 0.25, we take momentum slices of the data, find the mean and sigma of E_{tot}/p for that slice and cut out events outside $\pm 2.5\sigma$. Fig. 59 shows one of those slices with the Gaussian fit. This is done for values along p and fit the points for means and $\pm 2.5\sigma$ to polynomials. These two second-order polynomials are

$$\left(\frac{E_{tot}}{p} \right)_{+2.5\sigma} = 0.0008p^2 - 0.0112p + 0.3137 \quad (85)$$

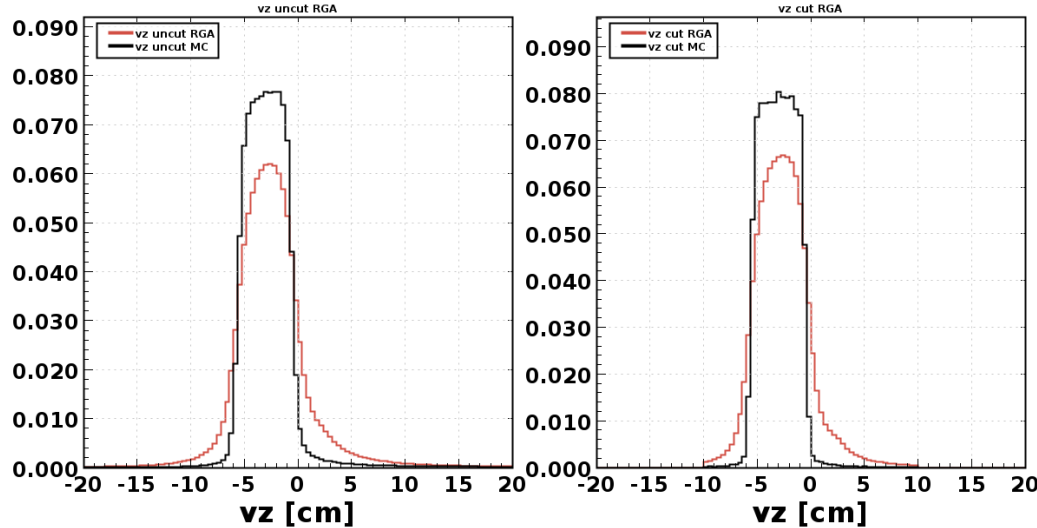


Fig. 57: The electron vertex v_z before (left) and after (right) all described cuts. Red lines are from RGA data and black lines are for the Monte-Carlo (MC) data.

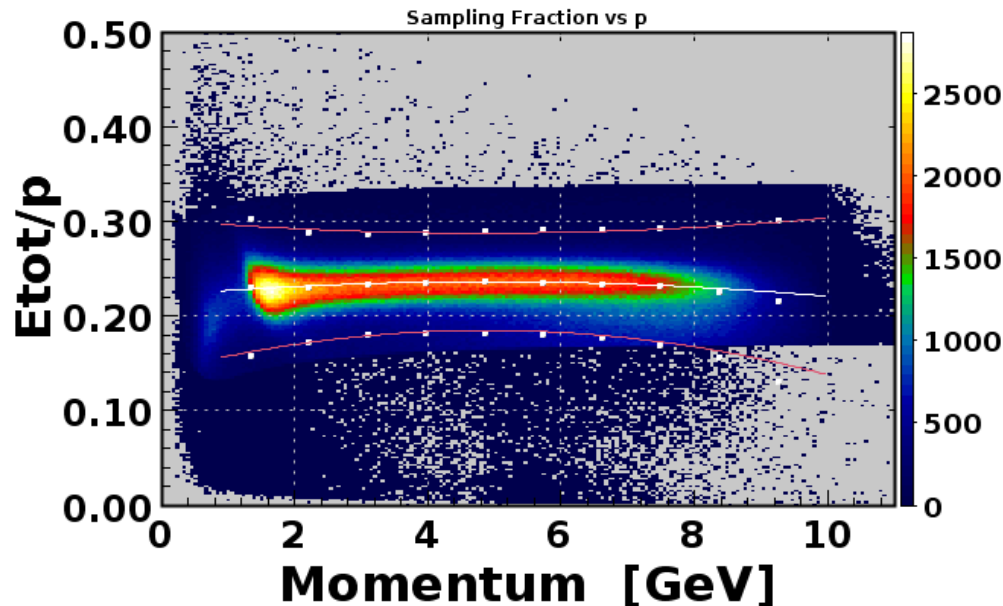


Fig. 58: Sampling fraction as a function of particle momentum. The dots represent the mean along the center and values $\pm 2.5\sigma$ from that mean. The red lines are the fitted polynomials.

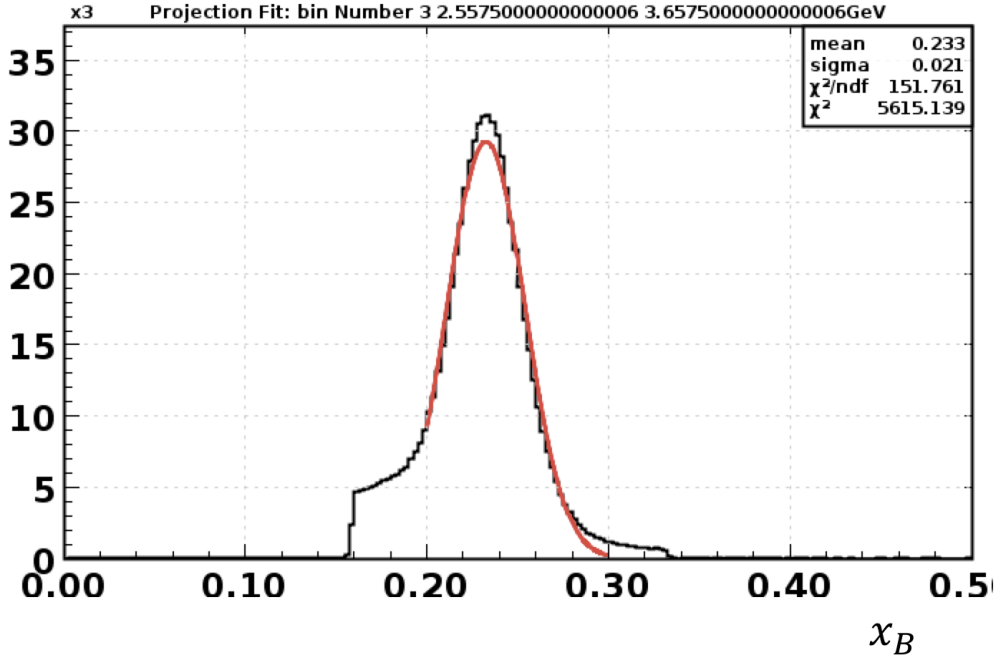


Fig. 59: Slice of the sampling fraction for $2.58 < p < 3.66$ GeV fitted to a Gaussian. The sigma is used to find the $\pm 2.5\sigma$ fit seen in Fig. 58.

and

$$\left(\frac{E_{\text{tot}}}{p}\right)_{-2.5\sigma} = -0.0017p^2 + 0.0228p + 0.1397 \quad (86)$$

for $+2.5\sigma$ and -2.5σ , respectively.

Because of the Forward Detector's coverage in θ , we apply an additional $5^\circ < \theta < 40^\circ$ cut on that variable. Fig. 60 shows the uncut kinematic variables and Fig. 61 was created with the kinematic cuts described. Fig. 62 and Fig. 63 shows uncut and cut (respectively) distributions for E' , E_{ECin} , E_{ECout} , E_{PCAL} , E_{ECtot} , and the number of photoelectrons in the HTCC ($nphe$). The total energy deposited in the EC (*i.e.* E_{ECtot}) is the addition of E_{ECin} and E_{ECout} . The next group of plots Figs. 64-69 shows two-dimensional histograms of various kinematic variables all uncut and after applying all cuts. In Fig. 69 one can clearly see the successful application of the 5σ cut described in the previous paragraph. The summary of applied cuts is as follows:

DIS Kinematics

- $W > 2 \text{ GeV}$
- $Q^2 > 1 \text{ GeV}^2$

Fiducial

- PCAL cuts: $U > 30 \text{ cm}$, $30 < V < 390 \text{ cm}$, and $30 < W < 390 \text{ cm}$
- $-10 < v_z < 10 \text{ cm}$
- $5^\circ < \theta < 40^\circ$

Particle ID (e^- selection)

- 5σ cut on sampling fraction
- HTCC cut: $nphe > 5$
- EC energy cuts: $E_{\text{PCAL}} > 0.06 \text{ GeV}$, $E_{\text{EC}_{\text{in}}} > 0.025 \text{ GeV}$, $E_{\text{EC}_{\text{out}}} > 0.05 \text{ GeV}$

There are clearly cuts applied during reconstruction (*i.e.* before the data analysis described here). These cuts occur in the Event Builder whose job it is to build tracks and identify particles. Some of the cuts that were described in this section to identify DIS electrons are used to identify all electrons. For example, in order to ensure a clear signal in the HTCC, the EB uses a cut below 2 photoelectrons (or 2 nphe) to assist in e^- PID. After the described cuts, the data agreed well with the MC data, with a few exceptions. The energy distributions for E_{PCAL} and $E_{\text{EC}_{\text{in}}}$ in Fig. 63 shows differences between RGA data and MC data, the cause of which remains unknown. In that same figure, there is a disagreement in the number of photoelectrons ($nphe$) in the HTCC between RGA and MC data. The reason for this also remains elusive.

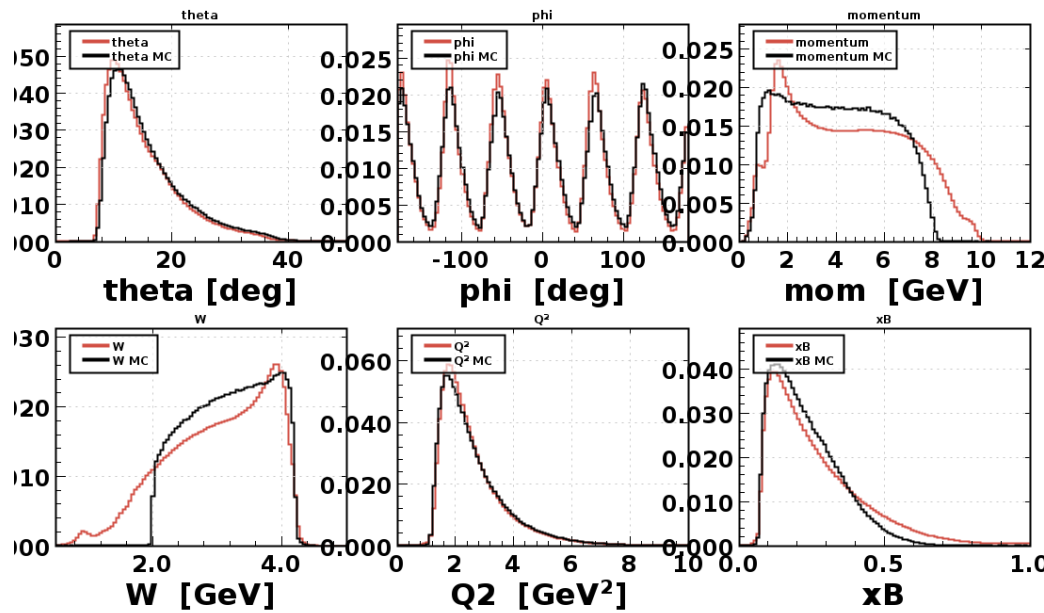


Fig. 60: Kinematic variables before cuts. Red lines are from RGA data and black lines are for the Monte-Carlo (MC) data.

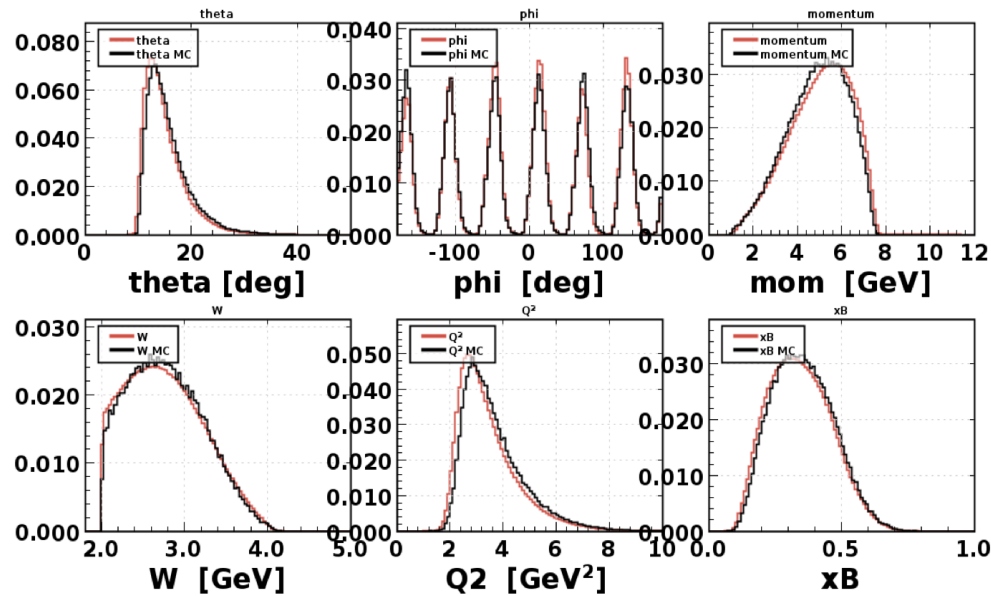


Fig. 61: Kinematic variables after all described cuts. Red lines are from RGA data and black lines are for the Monte-Carlo (MC) data.

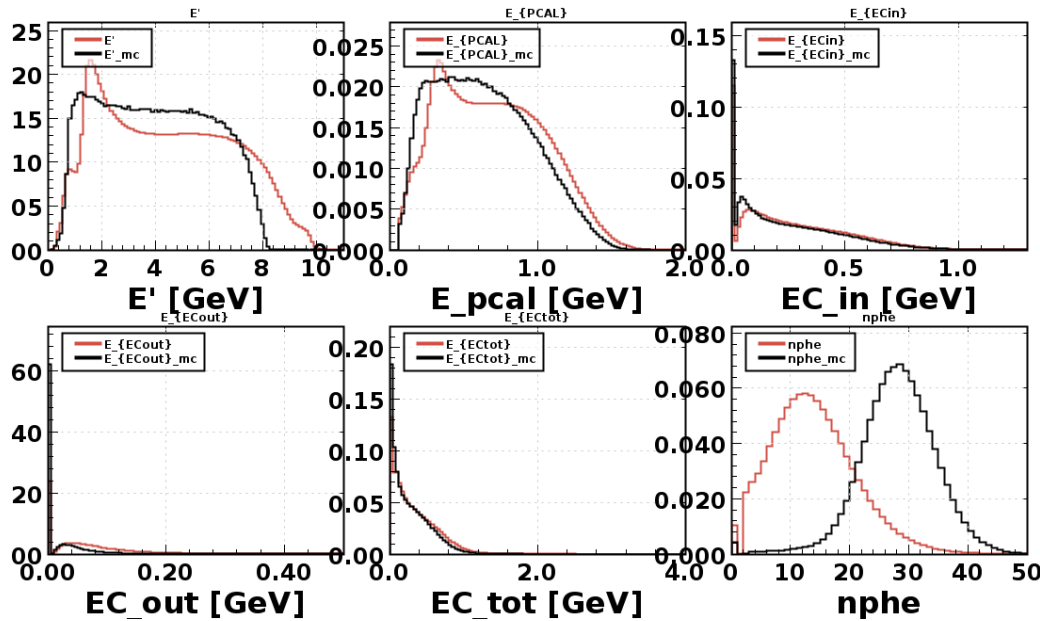


Fig. 62: E' , EC energies, and nphe before cuts. Red lines are from RGA data and black lines are for the Monte-Carlo (MC) data.

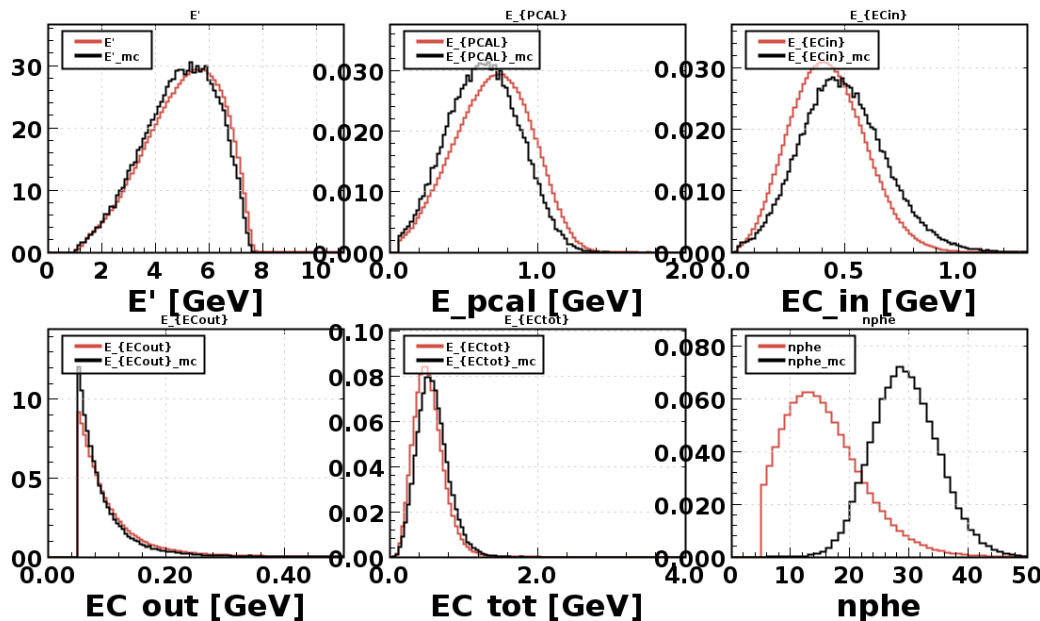


Fig. 63: E' , EC energies, and nphe after all described cuts. Red lines are from RGA data and black lines are for the Monte-Carlo (MC) data.

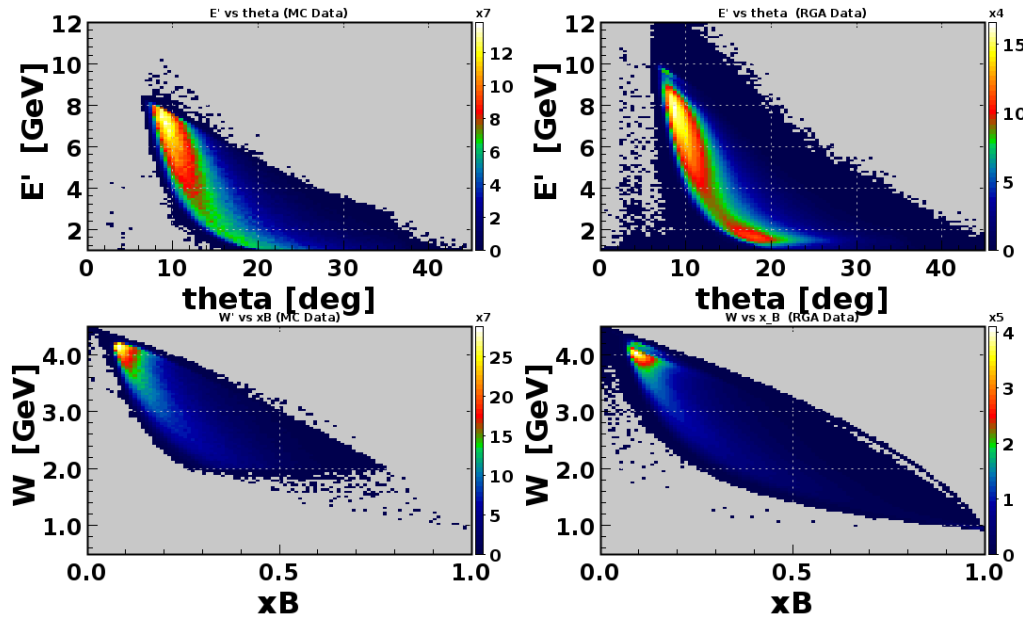


Fig. 64: E' vs. θ and W vs. x_B before cuts. The Monte Carlo data is on the left and the RGA data is on the right.

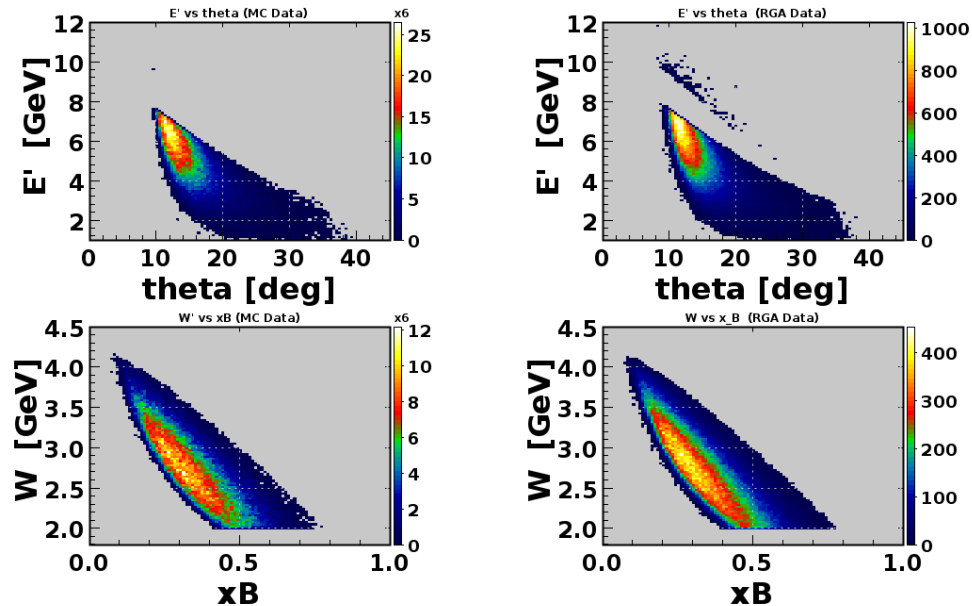


Fig. 65: E' vs. θ and W vs. x_B after all described cuts. The Monte Carlo data is on the left and the RGA data is on the right.

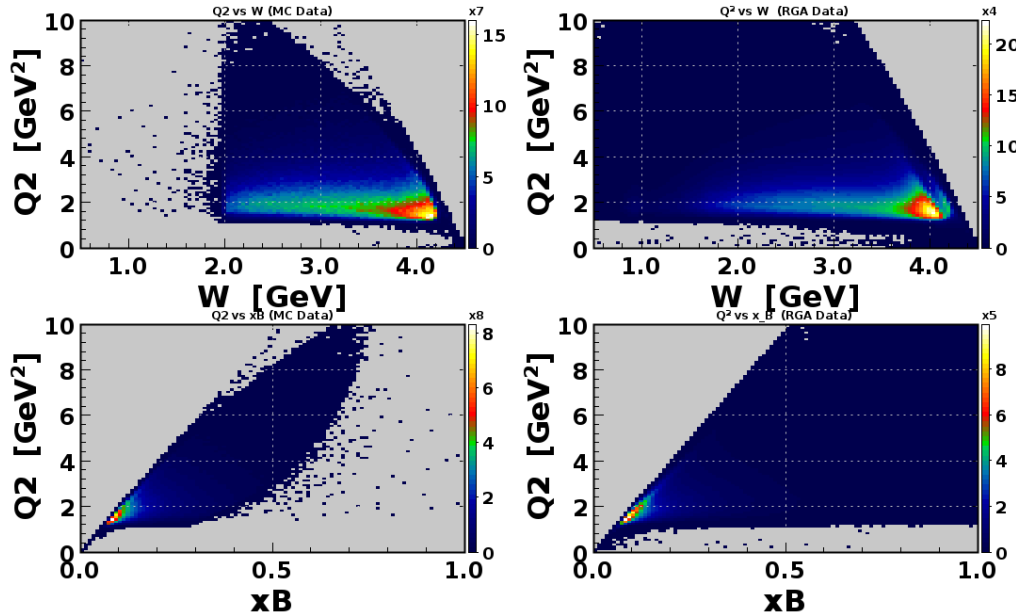


Fig. 66: Q^2 vs. W and Q^2 vs x_B before cuts. The Monte Carlo data is on the left and the RGA data is on the right.

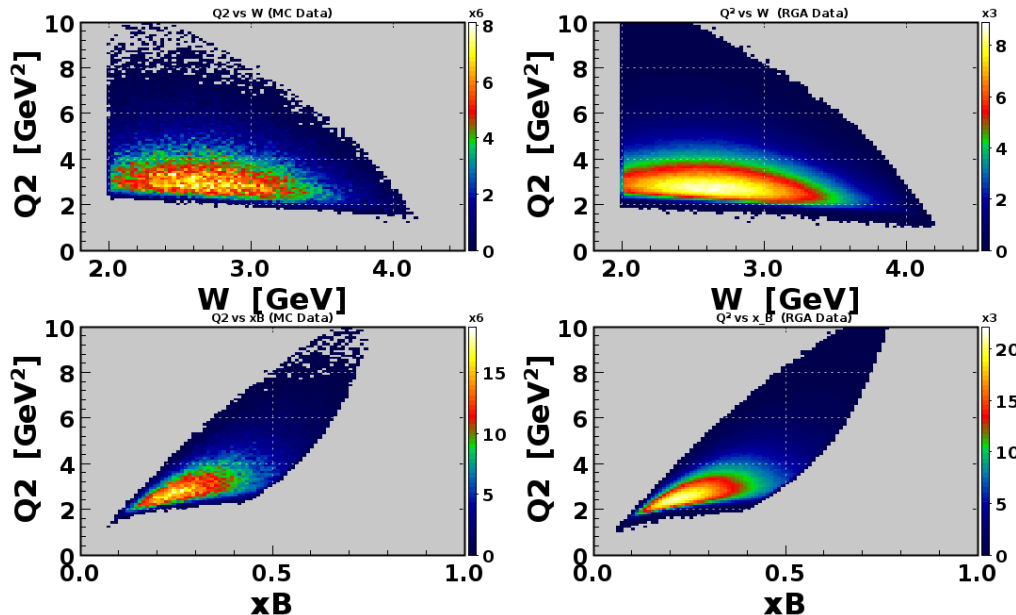


Fig. 67: Q^2 vs. W and Q^2 vs x_B after all described cuts. The Monte Carlo data is on the left and the RGA data is on the right.

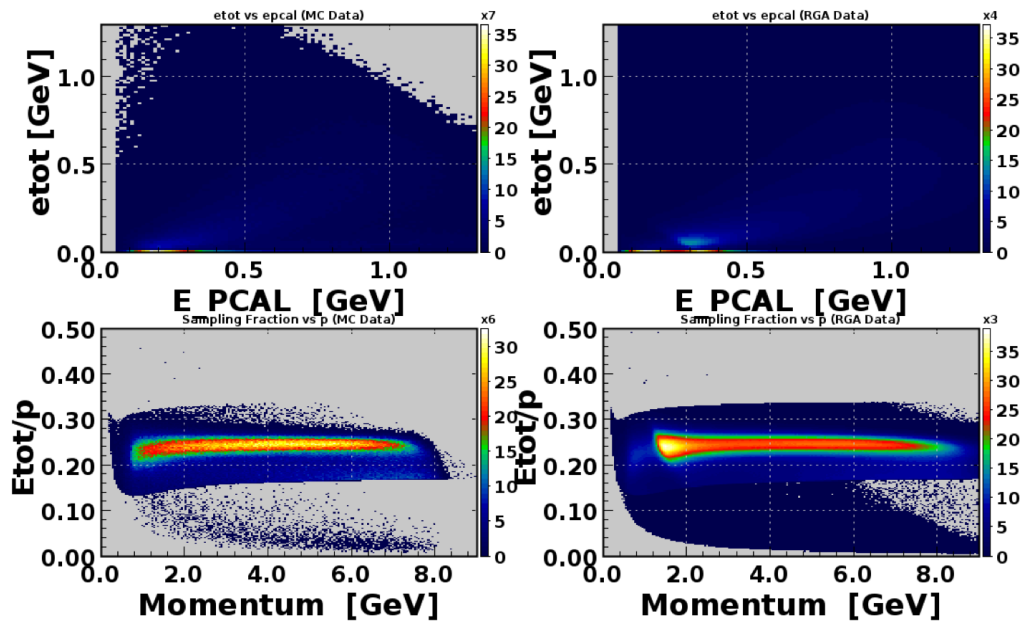


Fig. 68: $E_{EC_{tot}}$ vs E_{PCAL} and Sampling fraction vs. p before cuts. The Monte Carlo data is on the left and the RGA data is on the right.

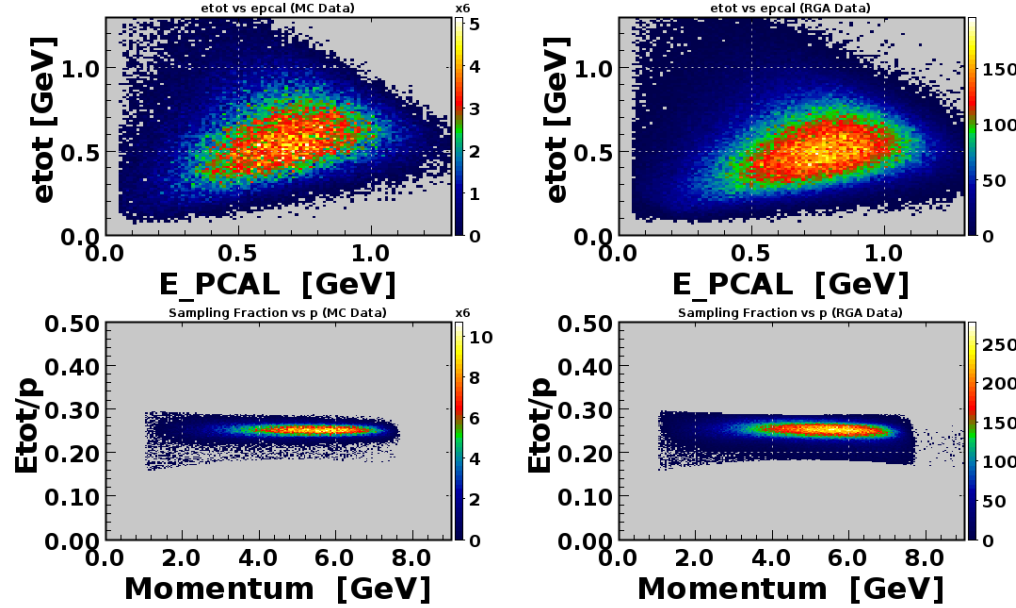


Fig. 69: $E_{EC_{tot}}$ vs E_{PCAL} and Sampling fraction vs. p after all described cuts. The Monte Carlo data is on the left and the RGA data is on the right.

5.6 BINNING AND ACCEPTANCE

The data, after kinematic and fiducial cuts, needs to be separated into kinematic bins in order to first obtain the acceptance of the bin and then to extract the cross section for each bin. The acceptance for the bin is the probability that an event in that bin will be successfully reconstructed in CLAS12. The acceptance can be determined using simulated (Monte Carlo) data:

$$A(x, y) = \frac{N_{\text{rec}}(x, y)}{N_{\text{gen}}(x, y)}, \quad (87)$$

where $A(x, y)$ is the acceptance of the bin, $N_{\text{gen}}(x, y)$ is the number of generated events in that bin, and $N_{\text{rec}}(x, y)$ is the number of reconstructed events in that bin. The binning occurs in x (*i.e.* the Bjorken- x scaling variable) and y , which is defined as $y = \nu/E$. This particular binning was chosen because of the form of the cross section used by Christy-Bosted [46], who parameterized existing data to the inclusive cross section, namely:

$$\frac{d^2\sigma}{dxdy} = \frac{4\pi\alpha_{\text{em}}S}{Q^4} \left[xy^2 F_1(x, Q^2) + \left(1 - y - xy \frac{M^2}{S} \right) F_2(x, Q^2) \right], \quad (88)$$

where $S = 2ME$.

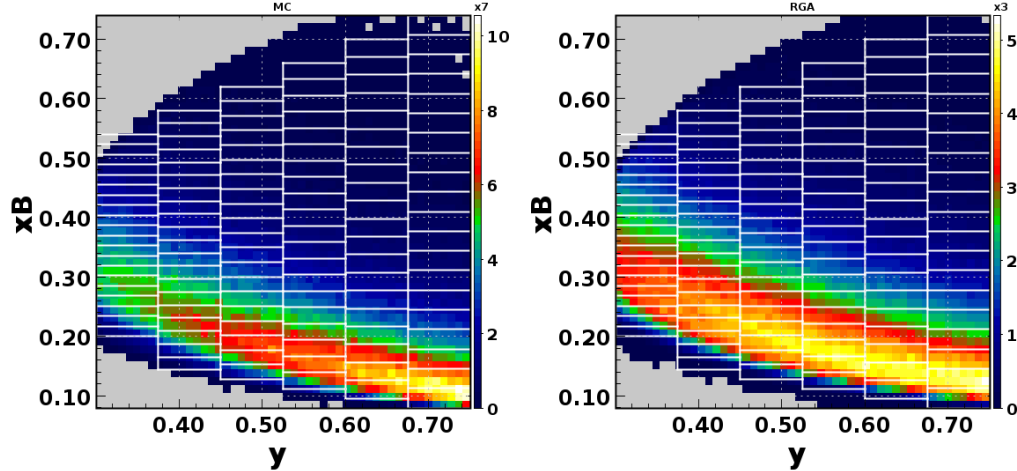


Fig. 70: Binning in the x, y space for MC data (left) and RGA Run 5036 data (right). These plots contain all events that pass the inclusive DIS cuts imposed as described in Section 5.5.

The binning in x and y was done in an attempt to ensure there were reasonable statistics in each bin. Equal bins were chosen in y because the distribution was

relatively flat in the range $0.3 < y < 0.74$. In x , however, the distribution in each y bin required binning within different ranges of x . Table IV outlines the bin size and range for x . Fig. 70 shows the binning in the x, y space.

Bin	y Range	x_{\min}	x_{\max}	Δx
1	0.3-0.375	0.2	0.54	0.017
2	0.375-0.45	0.144	0.58	0.0218
3	0.45-0.525	0.128	0.62	0.0246
4	0.525-0.6	0.112	0.66	0.0274
5	0.6-0.675	0.096	0.7	0.0302
6	0.675-0.74	0.08	0.74	0.033

TABLE IV: Summary of binning in x and y .

Figs. 71-73 show the acceptance for each bin. For each bin in y , the value of which is located in the caption of each plot, the acceptance is then plotted for each bin in x . The error on the acceptance is calculated using

$$\delta A(x, y) = \frac{A(x, y)}{\sqrt{N_{\text{rec}}}} \quad (89)$$

Ideally the acceptance for all bins would be unity, but in practice the CLAS12 detector cannot reconstruct all events because of geometric and detector limitations. It is clear that the acceptance in some bins is low. In fact, the first bin in x for each y bin was so low that those data points were omitted. In Fig. 71 we see that the acceptance is low at $x \rightarrow 0$ and in Fig. 73 acceptance drops as $x \rightarrow 1$.

5.7 FARADAY CUP AND INTEGRATED LUMINOSITY

As will become more evident in the next section, cross section extraction from data depends on the number of beam electrons accumulated during a particular run. Since the cross section is the probability that a reaction occurs for a given process, it also depends on the number of target nuclei. The *luminosity* (\mathcal{L}) is a quantity that incorporates both accumulated charge and the number of target nuclei by expressing the number of beam particles per time multiplied by the number of target nuclei per unit area. By integrating that luminosity over time, we can recover the total number of beam electrons multiplied by the number of target nuclei per unit area

$$\mathcal{L}_{\text{int}} = \int \mathcal{L} dt = \frac{N_B \times N_{\text{target}}}{A}, \quad (90)$$

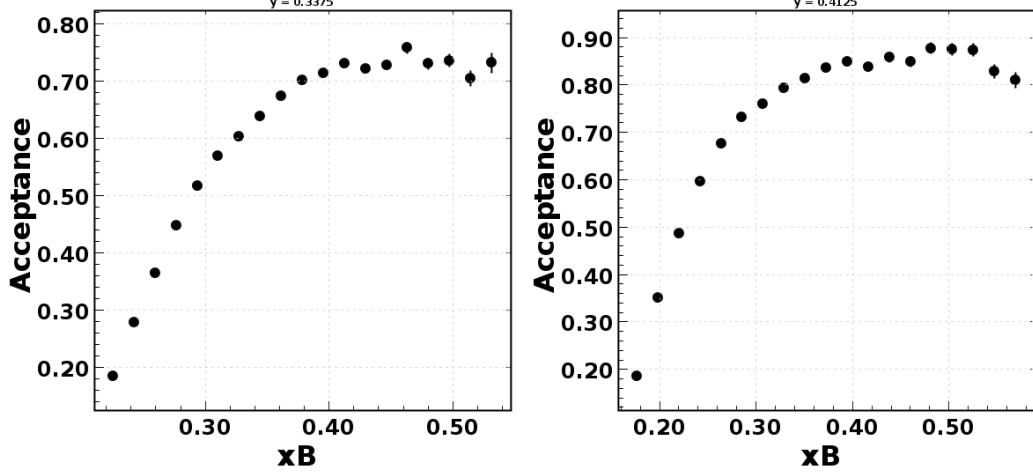


Fig. 71: Acceptance for $y = 0.3375$ (left) and $y = 0.4175$ (right) *vs* x .

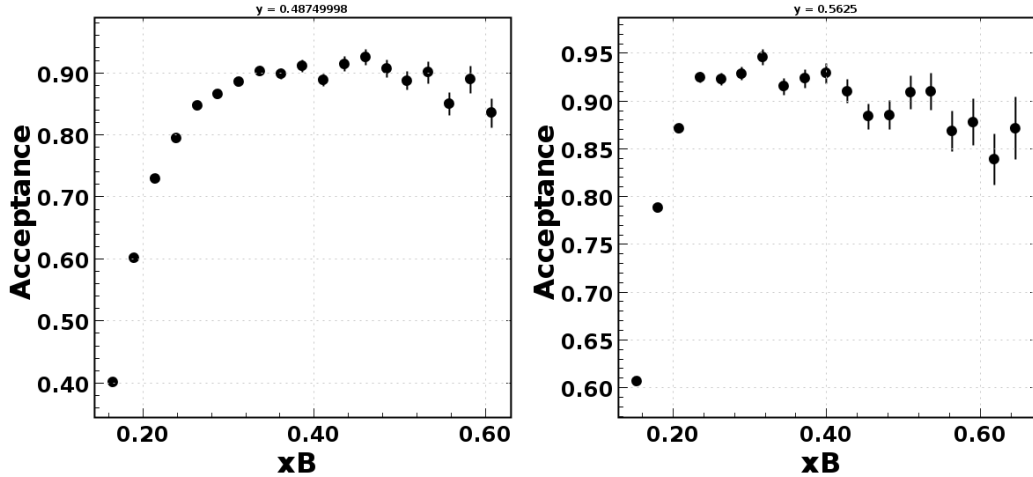


Fig. 72: Acceptance for $y = 0.4875$ (left) and $y = 0.5625$ (right) *vs* x .

where N_B is the total number of incident electrons, N_{target} is the number of target nuclei, and A is the cross-sectional area of the target (not to be confused with the acceptance $A(x, y)$). This time-integrated luminosity (\mathcal{L}_{int}) depends on calculating N_{target}/A and knowing the total number of electrons incident on the target.

Calculating the number of target nuclei per area can be done utilizing the expression

$$N_{\text{target}} = 2nN_A, \quad (91)$$

where n is the number of moles of target molecules, $N_A = 6.0221 \times 10^{23} \text{ mol}^{-1}$ is

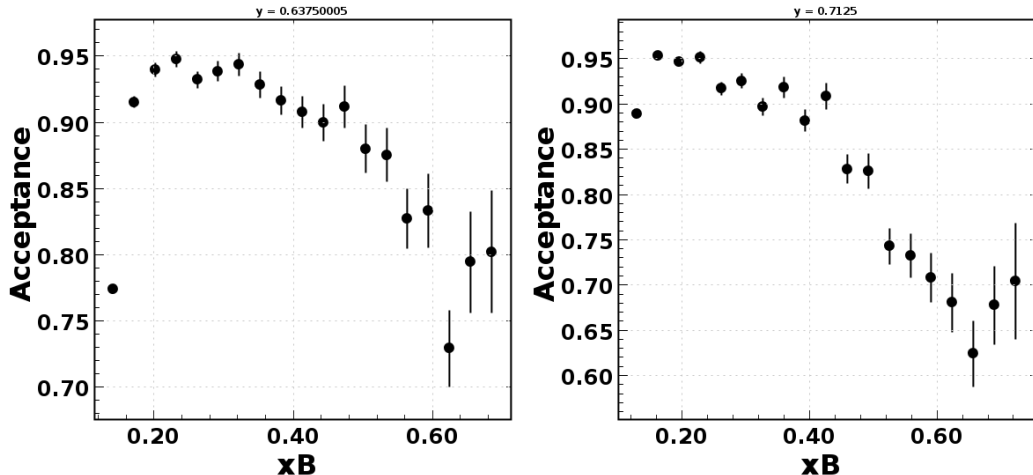


Fig. 73: Acceptance for $y = 0.6375$ (left) and $y = 0.7125$ (right) *vs* x .

Avogadro's number, and the "2" comes from the fact that molecular hydrogen (H_2) is used in liquid hydrogen target for Run Group A (RGA). In order to find N_{target} in terms of the target density $\rho = m/V$, where m is the mass of the target material and V is the volume of the target, we use the relation

$$n = \frac{m}{M_m} = \frac{\rho V}{M_m}, \quad (92)$$

where M_m is the molar mass. That results in

$$N_{\text{target}} = \frac{2\rho V N_A}{M_m}. \quad (93)$$

This gives us a time-integrated luminosity

$$\mathcal{L}_{\text{int}} = \frac{2N_B N_A \ell \rho}{M_m}, \quad (94)$$

where ℓ is the length of the target. The length of the RGA liquid H_2 was 4.87 cm.

Finally, we must find the total number of electrons N_B . We do this by accessing the charge accumulation in the Faraday Cup. The Faraday Cup (FC) is a device located at the end of the beam line that detects charged particles and accumulates the charge, giving access to the total charge during a given period (see Section 3.2.6). The FC data is given in nano Coulombs (nC) integrated over the entire run, where in every nC of charge there are 6.2415×10^9 electrons. That allows us to get the total number of incident electrons for each run, which is N_B in our integrated luminosity.

5.8 DIFFERENTIAL CROSS SECTION EXTRACTION

The final step is to actually calculate the differential cross section for each x, y bin. That cross section for experimental data is given by

$$\frac{d^2\sigma}{dxdy} = \frac{N(x, y)}{\mathcal{L}_{\text{int}} A(x, y) \Delta x \Delta y}, \quad (95)$$

where $N(x, y)$ is the number of DIS events in the bin, \mathcal{L}_{int} is the integrated luminosity, $A(x, y)$ is the acceptance of that bin, Δx is the size of the bin in x , and Δy is the size of the y bin. The number of selected inclusive deep inelastic scattering events $N(x, y)$ is tabulated for each x, y bin in Appendix C. The statistical uncertainty of the RGA extracted cross section is given by

$$\delta \frac{d^2\sigma(x, y)}{dxdy} = \frac{d^2\sigma/dxdy}{\sqrt{N(x, y)}}. \quad (96)$$

In the next chapter present the DIS cross section results for RGA data.

CHAPTER 6

RESULTS AND CONCLUSIONS

At the onset of this project, the goal was to simulate, optimize, design, construct, install and run the Radial Time Projection Chamber (RTPC) for the Barely-Offshell Nucleon Structure experiment at 12 GeV (BONuS12). BONuS12 ran successfully from January to March 2020, collecting 3.9 billion triggers and about 2.8 billion triggers with the RTPC. The run was cut short by the COVID19 pandemic, with only half of the expected data collected. Because it was always known that data collection would not be done in time for a full BONuS12 analysis in this work, important analysis on the first experiment (Run Group A) of CLAS12 was done to contribute to data analysis for the collaboration. This chapter will summarize the results of the RGA data analysis as well as the first monitoring and preliminary analysis plots from BONuS12.

6.1 RGA CROSS SECTION

The inclusive deep inelastic scattering differential cross section was extracted for $0.06 < x < 0.74$ and $0.3 < y < 0.74$ using data from Run Group A (RGA) Run 5036 (as shown in Fig. 76). The cross section was plotted and compared to the calculated cross section parameterized from fits of F_1 and F_2 (Eq. 88) by Christy-Bosted.[46] Fig. 76 shows the inclusive DIS differential cross section (on the y-axis) for the various y bins as a function of Bjorken- x (on the x-axis). The open dots are the extracted cross sections from the RGA data. The green band represents the fit including uncertainty of the DIS cross section calculated from the Christy-Bosted fits to F_1 and F_2 ,[46] The extracted cross section from RGA data is in reasonable agreement with the model and only begins to differ drastically at lower x .

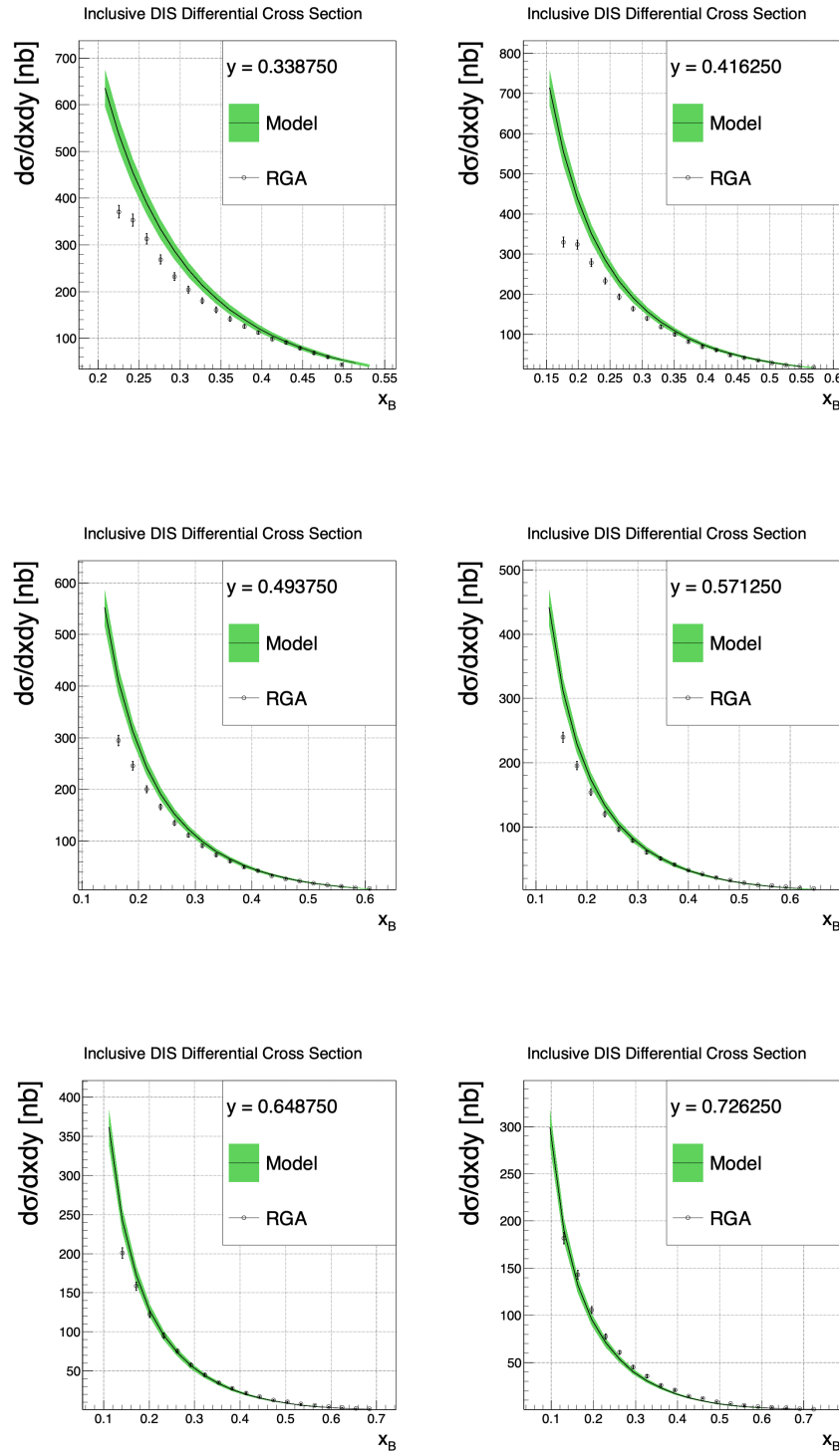


Fig. 76: Plots of inclusive DIS differential cross section vs x_B for various values of y . The green band represents the uncertainty of the DIS cross section calculated from the Christy-Bosted fits to F_1 and F_2 [46].

6.2 BONUS12

During the run time of BONuS12, some adjustment were made and target gases were used. The target was changed from hydrogen H₂ to helium ³He for calibration and deuterium D₂ for production. At the beginning of Run Group F, of which BONuS12 was a part, the beam energy was set to 1 pass around the accelerator to produce 2.14 GeV energy. This allowed the gathering of data to measure elastic scattering from protons in hydrogen, a well known process used to confirm that all detectors were functioning well. Once the 2.14 GeV data were gathered, the energy was increased to 5 passes to created 10.4 GeV beam electrons.

Once the 10.4 GeV beam energy was reached, it became clear that the RTPC was not operating up to expectations. The number of hits/track and the mean ADC value of those individual hits began to decrease. In order to fix these problems, the potential in the drift region as well the potential differences between each GEM foil was adjusted. The hits/track and mean ADC of the hits would increase for a time (about 6-12 hours), and then those values would decrease again. The magnitude of the magnetic field created by the solenoid was also adjusted. The first runs were at 5T field, and then decreased to 4T. This was in an attempt to decrease the drift angle of the drift electrons, thinking that those electrons were having a difficult time passing through the GEM foils. In all, the first RTPC (RTPC1) was in use for 33 days at roughly 50% efficiency. After that time, RTPC1 was replaced with another, previously constructed, RTPC (RTPC3) during a 5 day replacement period. RTPC3 ran for 3 days before the shutdown.

6.2.1 DMS

During the running of BONuS12, the RTPC gas system ensured that the proper gas flow rate and pressure was maintained. Downstream of the RTPC, the drift gas flowed through the Drift-gas Monitoring System (DMS). The DMS was there to monitor any fluctuations in important gas properties (*e.g* temperature, pressure, gas mixture, etc.). The output of the DMS was two TDC readings accumulated in histograms for each channel. Channel 1 (CH1) was the TDC readout for the time difference between the anode signal and the signal from the PMT near to the anode. Channel 2 (CH2) was the TDC readout for the time difference between the anode signal and the signal from the PMT far from the anode.

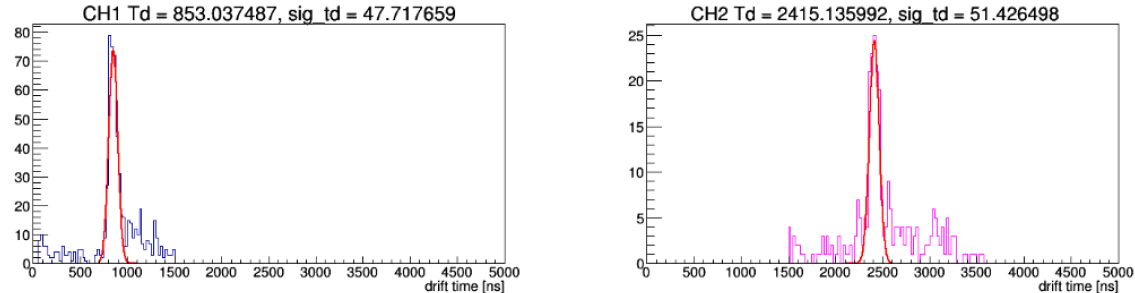


Fig. 77: DMS drift time histograms for CH1 (left) and CH2 (right) on Run 11953.

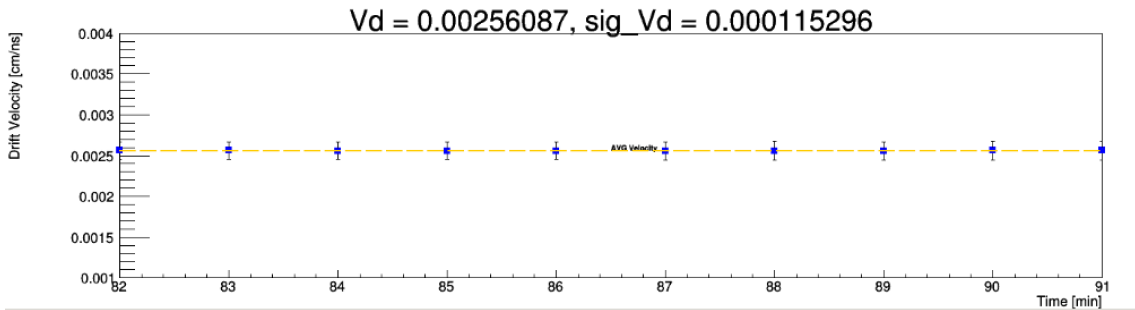


Fig. 78: DMS drift velocity vs. time graph during Run 11953.

Fig. 77 shows an example of the drift time output for channels 1 and 2 (left and right, respectively) for Run 11953. The drift velocity is calculated by

$$v = \frac{\Delta d}{\Delta t} = \frac{4 \text{ cm}}{t_{\text{CH2}} - t_{\text{CH1}}}. \quad (97)$$

Fig. 78 shows the drift velocity vs. time graph for Run 11953. The orange dotted line is the average velocity for the 10 minutes shown on the plot. These plots were indicative of the majority of runs, showing that the gas parameters were relatively stable. The few exceptions occurred for two reasons.

The first reason for deviations from typical DMS output was its sensitivity to the flow rate of the drift gas through the RTPC. If it was too low, not enough gas would flow into the DMS and the number of accumulated statistics would decrease and the peaks in drift time typical of runs (as in Fig. 77) would not appear. This did serve as an advantage when identifying empty gas bottles, however. If the flow rate was high and statistics still dropped, it was an indicator that the bottle of drift gas needed to be replaced.

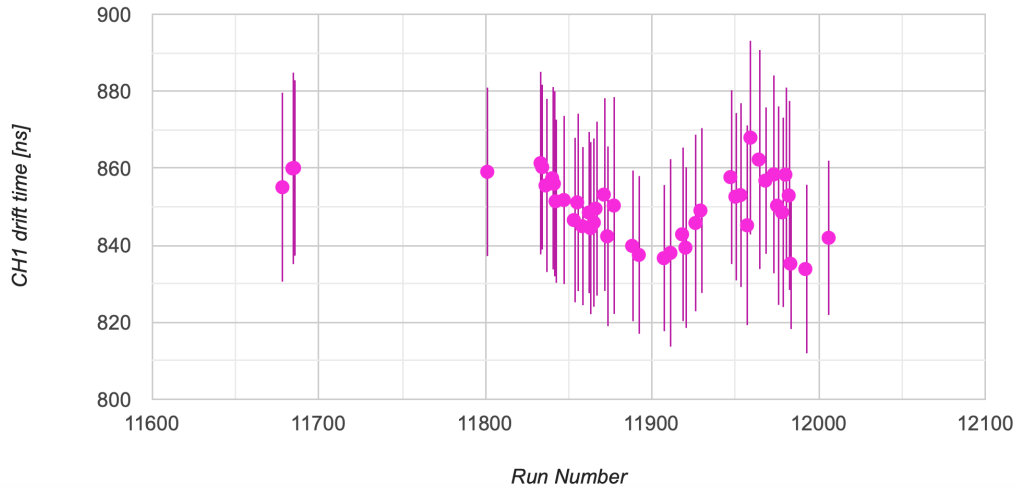


Fig. 79: DMS drift velocity for channel 1 vs. run.

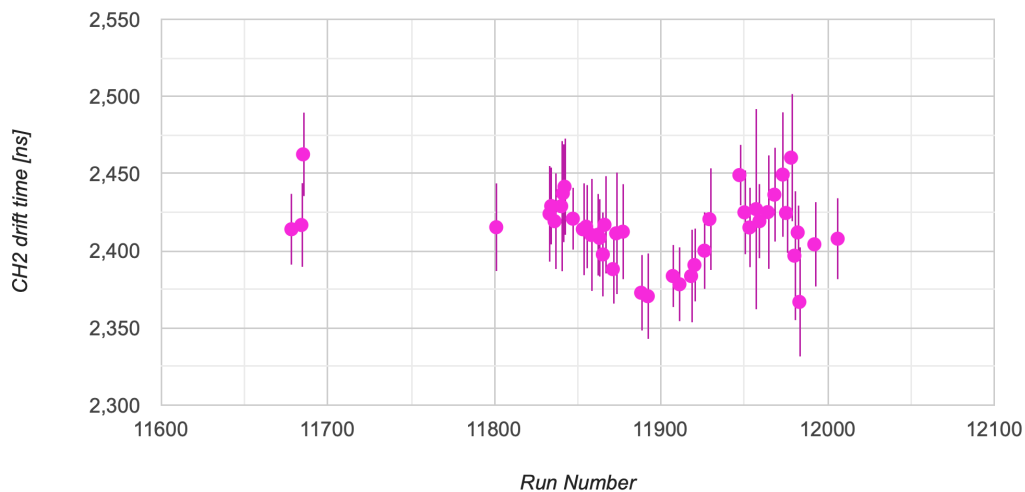


Fig. 80: DMS drift velocity for channel 2 vs. run.

The other reason for deviations from typical DMS output was, of course, variations in the parameters it was designed to monitor. When the ambient pressure decreased, the drift times for each channel would decrease, which meant the drift velocity increased. Fig. 79 shows the channel 1 drift time for each run. Fig. 80 shows the channel 2 drift time for each run, and Fig. 81 shows the DMS pressure for each run. The ambient pressure began to decrease around Run 11847 to a minimum at Run 11918. This corresponds to the decreased drift times visible during the same

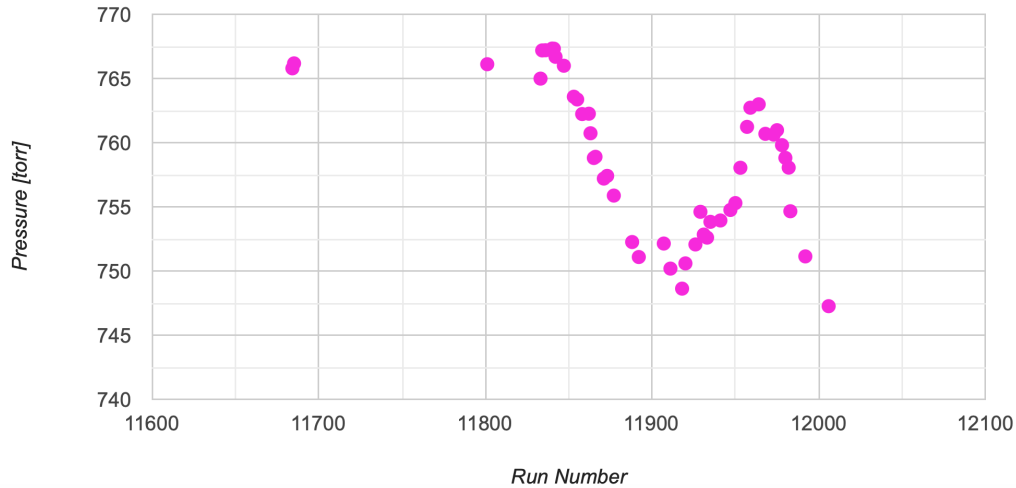


Fig. 81: DMS gas pressure vs. run.

runs (Figs. 79 and 80), which means that the DMS was sensitive to changes in gas pressure. Fig. 82 shows the drift velocity over Run Group F.

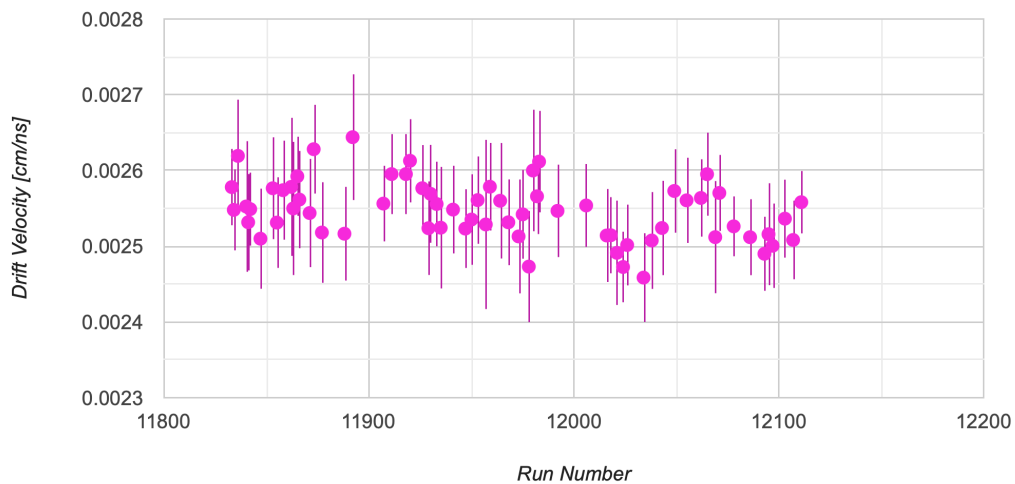


Fig. 82: DMS drift velocity over all RGF runs.

6.2.2 RTPC

The tracking software developed by David Payette for RTPC hit reconstruction was put into use on RGF data as soon as data started flowing into the DAQ. Fig. 83 shows two examples of reconstructed tracks using Version 27 of the reconstruction software for Run 11637, which is a 2.14 GeV run at 5 nA. Fig. 84 shows the reconstructed tracks for separate two time windows in Run 12240, which is a 10.4 GeV run at 240 nA. The increase in current is the reason there are more tracks per event.

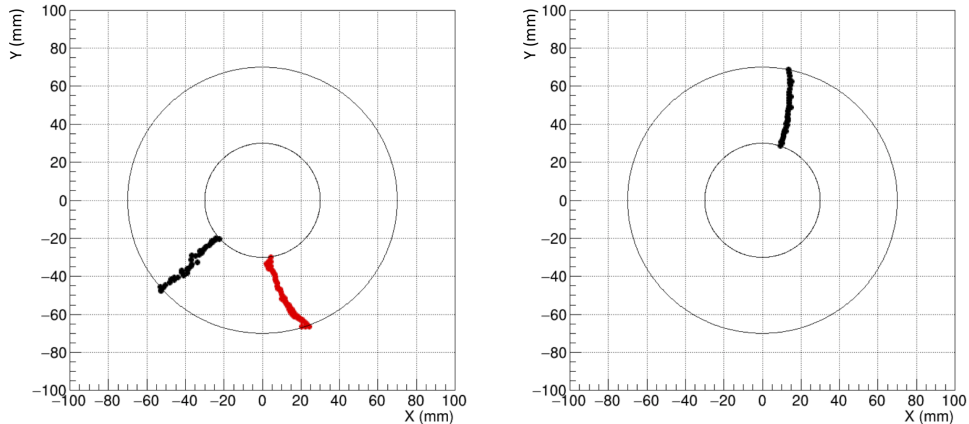


Fig. 83: Two examples of reconstructed tracks in one time window in the RTPC using Version 27 of the reconstruction software in a Cartesian x, y space for Run 11637 (2.14 GeV). [Courtesy D. Payette.]

The RTPC reconstruction class, which is integrated into CLARA, consists of a few steps necessary for proton momentum reconstruction that is critical for extraction of the F_2^n/F_2^p structure function ratio. The first is the reconstruction of all hits in an event. This is done using a combination of parameters extracted from Garfield++ and data. The next step is to separate the hits into tracks and disentangle crossing tracks from one another. Finally, once tracks are identified, a helix fitter is used to recover the momentum and vertex of the track. A particle with charge q follows a helical path in a uniform magnetic field B with a certain radius R . The momentum of that particle is then

$$p = RqB. \quad (98)$$

Obviously, since the magnetic field is not uniform, the charged particle (in our case, the proton) does not travel in an exact helix. The answer to this problem is called

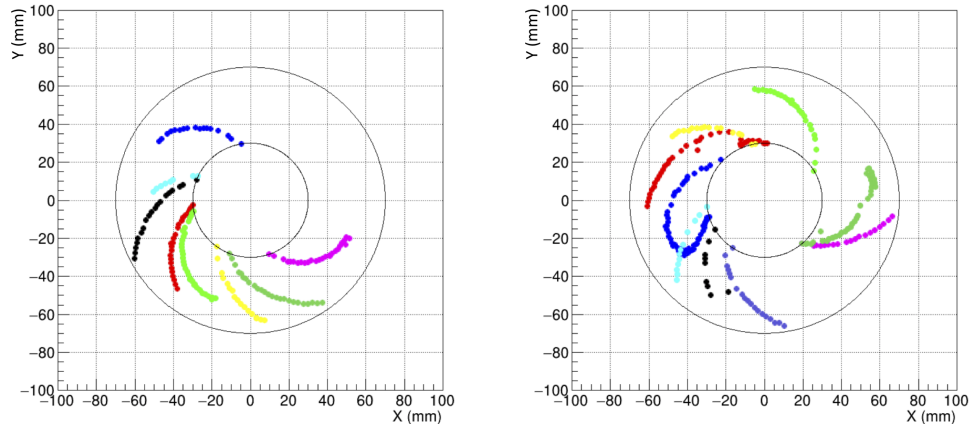


Fig. 84: Two examples of reconstructed tracks in one time window in the RTPC using Version 26 of the reconstruction software in an Cartesian x, y space for Run 12240 (10.4 GeV). [Courtesy D. Payette.]

a Kalman Filter. The Kalman Filter accounts for non-uniform magnetic fields and decreasing proton momentum by accounting for variations in each step. Implementation of the Kalman Filter will likely be done at a later date.

Once the kinematics of the proton tracks are reconstructed from the raw data, that reconstructed data is analyzed to find the “good” proton (corresponding to the electron that triggered the event) among the background. This identification in parallel with revisions to the reconstruction code will be an ongoing process. Fig. 85 shows some of the kinematics of the reconstructed protons with one cut on t_{shift} , which is a variable determined from the electron trigger. This cut of $-200\text{ns} < t_{\text{shift}} < 500\text{ns}$ is done in an attempt to isolate protons tracks that occur around the time of an identified electron trigger in the CLAS12 forward detectors (FD).

Because Run 11637 was a low energy run at 2.14 GeV, it was analyzed in comparison to expected elastic scattering kinematics. For elastic $ep \rightarrow e'p'$ events, the proton momentum is

$$p_{\text{calc}} = \sqrt{Q^2 + \frac{Q^4}{4M_P^2}} \quad (99)$$

and the scattering angle is

$$\theta_{\text{calc}} = \tan^{-1} \left[\frac{1}{\left(1 + \frac{E}{M_p} \right) \tan \left(\frac{\theta_e}{2} \right)} \right], \quad (100)$$

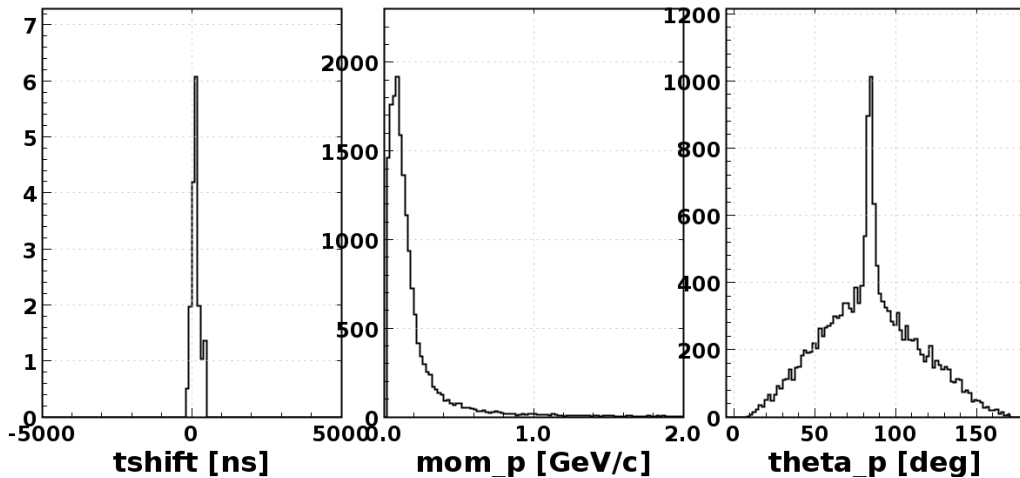


Fig. 85: The time shift (t_{shift}), momentum, and theta (θ) of the reconstructed protons in Run 11637.

where E is the beam energy and θ_e is the scattering angle of the electron. Fig. 86 shows the 2D distribution of the calculated momentum (“mom_predicted” in the plot) and measured momentum for protons as well as the difference between the predicted and measured values of the momentum for Run 11637. Fig. 87 shows the 2D distributions of the calculated theta (“theta_predicted” in the plot) and measured theta for protons as well as the difference between the predicted and measured values of theta for Run 11637.

There are some clear irregularities in the reconstruction of proton kinematics. For example, in Fig. 86, the peak of Δp is around 200 MeV, which should be at zero. Calibrations that focus on recovering accurate kinematics will be ongoing by BONuS12 collaborators until expected results for the calibration runs are achieved. Once acceptable calibration occurs, intensive data analysis to recover the proton momentum will begin and likely continue for years to come. This analysis will lead to an extraction of the F_2^n/F_2^p structure function ratio at higher x than previously accessed. Knowing this structure function ratio allows us to know more about the overall structure of the neutron, which was the goal of the simulation and development of the Radial Time Projection Chamber for the Barely Off-shell Nucleon Structure experiment at 12 GeV.

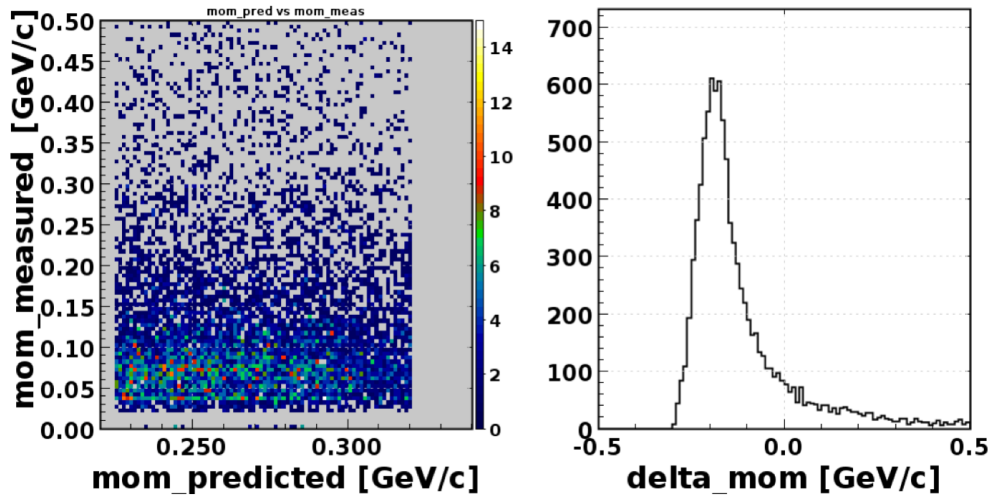


Fig. 86: On the left: 2D distributions of the calculated momentum (“mom_predicted” in the plot) on the x -axis and reconstructed momentum (“mom_measured” in the plot) for protons on the y -axis in Run 11637. On the right: The difference between the predicted and measured values of the momentum for Run 11637.

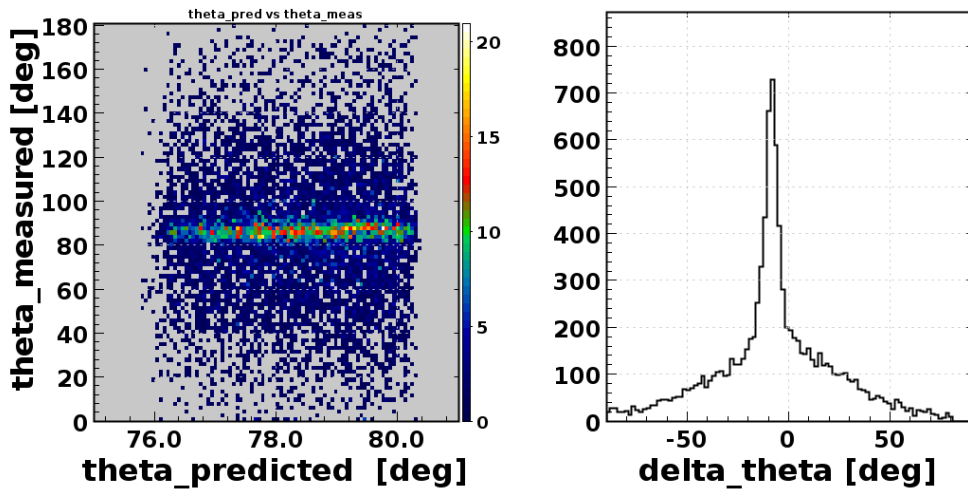


Fig. 87: On the left: 2D distributions of the calculated theta (“theta_predicted” in the plot) on the x -axis and reconstructed theta (“theta_measured” in the plot) for protons on the y -axis in Run 11637. On the right: The difference between the predicted and measured values of theta for Run 11637.

6.3 CONCLUSIONS

The Drift-gas Monitoring System for the BONuS12 experiment worked well during the experimental run and proved its usefulness in monitoring gas properties. The BONuS12 experiment itself, while it ended rather abruptly, did successfully run for 33 days and gathered 2.8 billion triggers with the RTPC. At this time, calibration of the RTPC is not complete and so the proton kinematics do not yet agree with elastic scattering predictions. The data gathered will shed light on the the F_2^n/F_2^p ratio, which is the key quantity for understanding the quark structure of the neutron. Extracting this ratio depends on an accurate understanding of the scattered electron as detected in CLAS12. Inclusive deep inelastic scattering from an earlier data set were presented and compared to an established model. The results presented in this work were consistent with previous data, although deviations were observed at small x , where the acceptance was considerably small and possibly inaccurate. The overall program of investigating nucleon structure will continue for years to come at Jefferson Lab and then with the Electron Ion Collider at Brookhaven National Lab in Upton, NY.

REFERENCES

- [1] J. Dalton, *A New system of chemical philosophy*. London, 1808.
- [2] R. Carlitz, “On radiant matter,” *The Popular Science Monthly D*, vol. 16, 1880.
- [3] J. Thomson, “Cathode rays,” *The Electrician*, vol. 39, 1897.
- [4] E. Rutherford, *Radioactive Transformations*. Charles Shribner’s Sons, 1906.
- [5] E. Rutherford, *Radioactive Substances and their radiations*. Cambridge, 1913.
- [6] A. Einstein, “On a heuristic viewpoint concerning the production and transformation of light,” *Annalen der Physik*, vol. 322, 1905.
- [7] B. Povh *et al.*, *Particles and Nuclei: An Introduction to Physical Concepts*. Springer, 2008.
- [8] F. Halzen and A. Martin, *Quarks and Leptons: An Introductory Course in Modern Particle Physics*. John Wiley and Sons, 1984.
- [9] J. Bjorken and S. Drell, *Relativistic quantum mechanics*. McGraw-Hill, 1964.
- [10] M. Tanabashi *et al.*, “Particle Data Group,” *Phys. Rev. D*, vol. 98, 2018.
- [11] M. Tanabashi *et al.*, “Baryon form factors at high Q^2 and the transition to perturbative QCD,” *Phys. Rep.*, vol. 226, 1993.
- [12] A. Accardi *et al.*, “Constraints on large- x parton distributions from new weak boson production and deep-inelastic scattering data,” *Phys. Rev. D*, vol. 93, 2016.
- [13] F. Close, *An Introduction to Quarks and Partons*. Academic Press, 1979.
- [14] F. Close, “ νW_2 at small ω and resonance form factors in a quark model with broken $SU(6)$,” *Phys. Lett. B*, vol. 43, p. 422, 1973.
- [15] R. Carlitz, “ $SU(6)$ symmetry breaking effects in deep inelastic scattering,” *Phys. Lett. B*, vol. 58, p. 345, 1975.
- [16] N. Isgur, “Violations of $SU(6)$ selection rules from quark hyperfine interactions,” *Phys. Rev. Lett*, vol. 41, pp. 1269–1272, 1978.

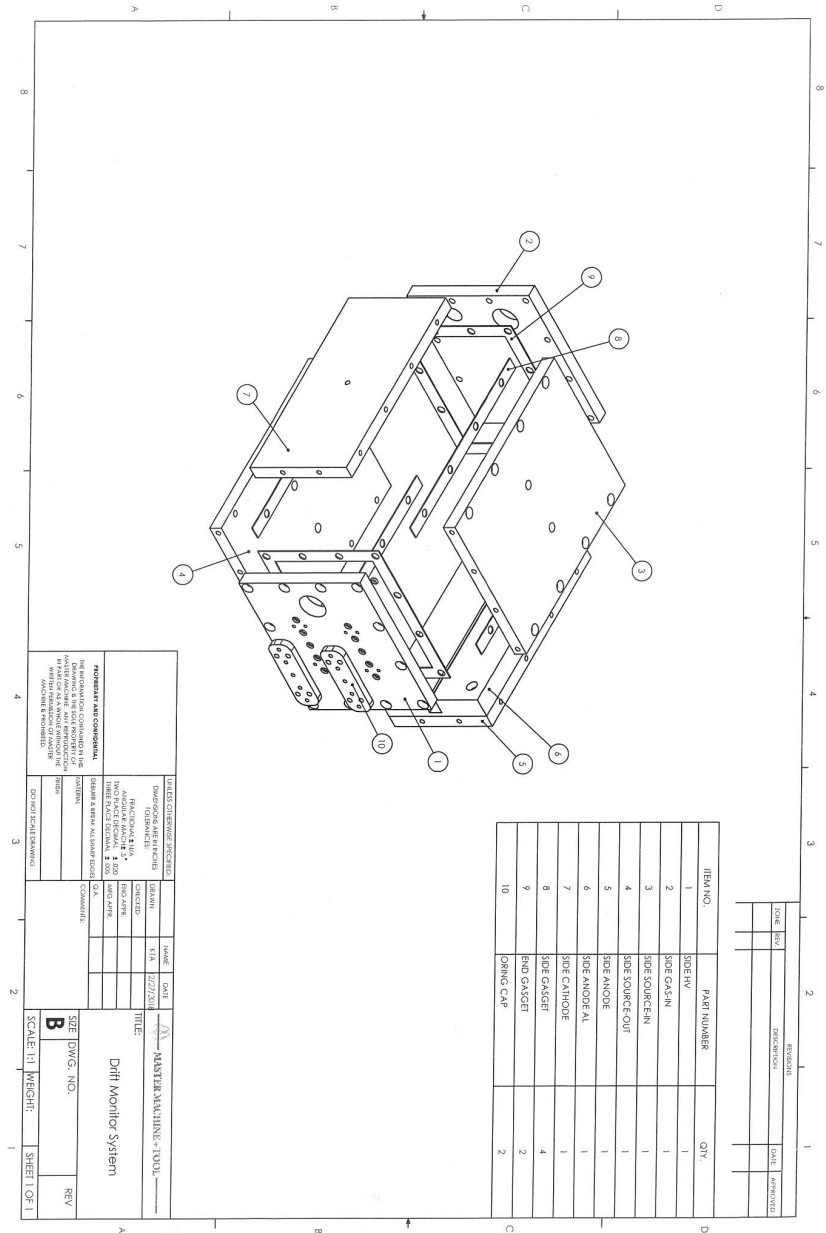
- [17] N. Insgur, “Valence quark spin distribution functions,” *Physical Review D*, vol. 59, p. 034013, 1999.
- [18] J. Arlington, “MeAsurement of the F_2^n/F_2^p , d/u RAtios and A=3 EMC Effect in Deep Inelastic Electron Scattering Off the Tritium and Helium MirrOr Nuclei,” *Jefferson Lab PAC37 Proposal*, 2010.
- [19] G. Farrar and D. Jackson, “Pion and nucleon structure functions near $x = 1$,” *Phys. Rev. Lett.*, vol. 35, p. 1416, 1975.
- [20] S. Brodsky *et al.*, “Perturbative QCD constraints on the shape of polarized quark and gluon distributions,” *Nucl. Phys. B*, vol. 441, pp. 197–214, 1995.
- [21] J. Ashman *et al.*, “A measurement of the ratio of the nucleon structure function in copper and deuterium,” *Z. Phys. C*, vol. 57, p. 211, 1993.
- [22] J. Gomez *et al.*, “Measurement of the A-dependence of deep inelastic electron scattering,” *Phys. Rev D*, vol. 49, p. 4348, 1994.
- [23] D. Geesaman *et al.*, “The nuclear EMC effect,” *Ann. Rev. Nucl. Part. Sci.*, vol. 45, pp. 337–390, 1995.
- [24] M. Sargsian and M. Strickman, “Model independent method for determination of the DIS structure of free neutron,” *Phys.Lett. B*, vol. 639, p. 223, 2006.
- [25] C. Ciofi degli Atti *et al.*, “Hadronization and final state interaction effects in semi-exclusive deep inelastic scattering off nuclei,” *Eur. Phys. Jour. A*, vol. 19, pp. 133–137, 2004.
- [26] M. Spata, “CEBAF overview.”
- [27] D. Douglas *et al.*, “The Continuous Electron Beam Accelerator Facility: CEBAF at the Jefferson Laboratory,” *Annu. Rev. Nucl. Part. Sci. 2001*, vol. 51, pp. 413–450, 2001.
- [28] R. Fair *et al.*, “The CLAS12 superconducting magnets,” *Nucl. Inst. and Meth. A*, vol. 962, p. 163578, 2020.
- [29] Y. Sharabian *et al.*, “The CLAS12 high threshold cherenkov counter,” *Nucl. Inst. and Meth. A*, vol. in press, 2020.

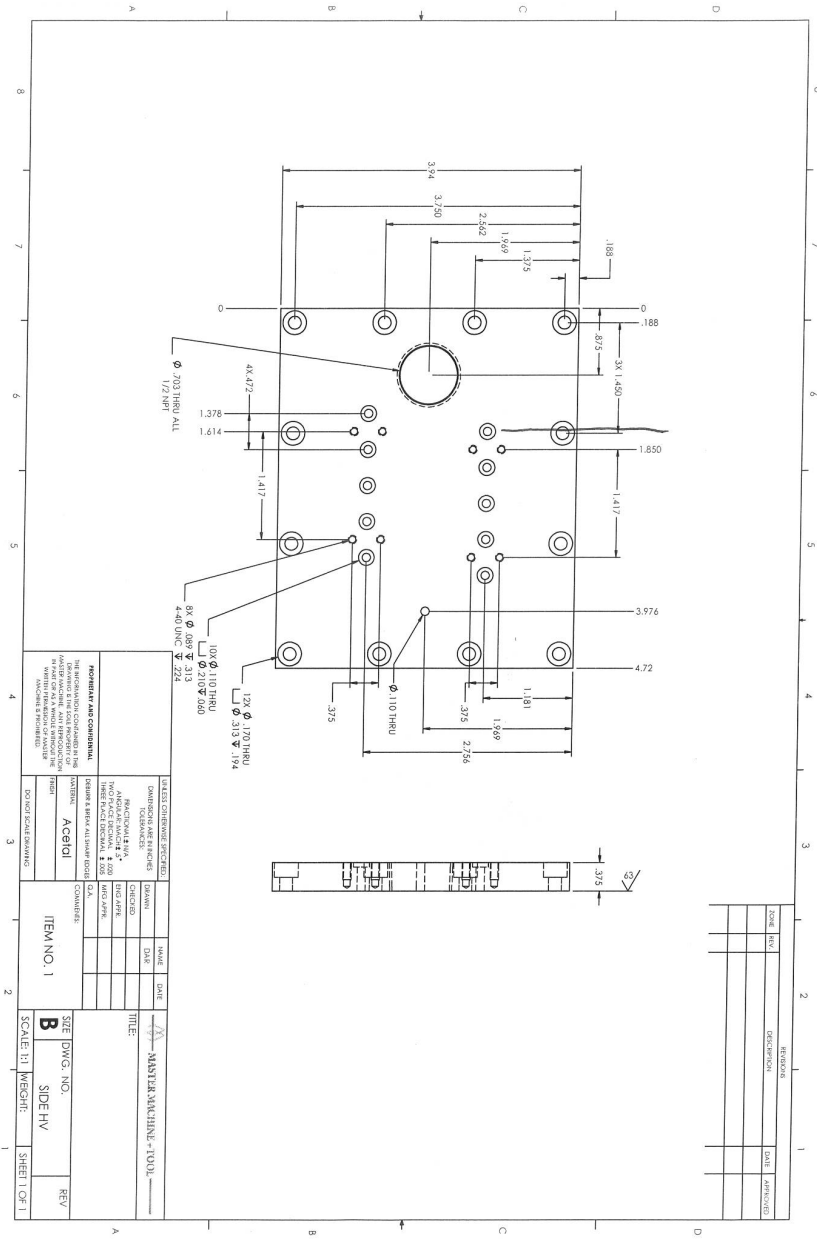
- [30] M. Ungaro *et al.*, “The CLAS12 low threshold cherenkov detector,” *Nucl. Inst. and Meth. A*, vol. 957, p. 163420, 2020.
- [31] M. Mestayer *et al.*, “The CLAS12 drift chamber system,” *Nucl. Inst. and Meth. A*, vol. 959, p. 163518, 2020.
- [32] D. Carman *et al.*, “The CLAS12 forward time-of-flight system,” *Nucl. Inst. and Meth. A*, vol. 960, p. 163629, 2020.
- [33] G. Gilfoyle and K. Sherman, “Geometry update for the electromagnetic calorimeter in CLAS12,” *CLAS12 Note 2014-008*, 2014.
- [34] G. Asryan *et al.*, “The CLAS12 forward electromagnetic calorimeter,” *Nucl. Inst. and Meth. A*, vol. 959, p. 163425, 2020.
- [35] V. Burkert *et al.* [CLAS12 Collaboration], “The CLAS12 Spectrometer at Jefferson Lab,” *Nuc. Inst. and Meth. A*, vol. 959, p. 163419, 2020.
- [36] D. Carman *et al.*, “The CLAS12 central time-of-flight system,” *Nucl. Inst. and Meth. A*, vol. 960, p. 163626, 2020.
- [37] F. Sauli, “The gas electron multiplier (GEM): Operating principles and applications,” *Nucl. Inst. and Meth. A*, vol. 805, pp. 2–24, 2016.
- [38] P. Baron *et al.*, “DREAM user manual, version 3.0.”
- [39] S. Boyarinov *et al.*, “The CLAS12 data acquisition system,” *Nucl. Inst. and Meth. A*, vol. 966, p. 163698, 2020.
- [40] A. Acker *et al.*, “The CLAS12 micromegas vertex tracker,” *Nucl. Inst. and Meth. A*, vol. 957, p. 163423, 2020.
- [41] A. Acker *et al.*, “The CLAS12 forward tagger,” *Nucl. Inst. and Meth. A*, vol. 959, p. 163475, 2020.
- [42] M. Ungaro *et al.*, “The CLAS12 Geant4 simulation,” *Nucl. Inst. and Meth. A*, vol. 959, p. 163422, 2020.
- [43] S. Agostinelli *et al.*, “Geant4 - a simulation toolkit,” *Nuc. Inst. Meth. A*, vol. 506, pp. 250–303, 2003.

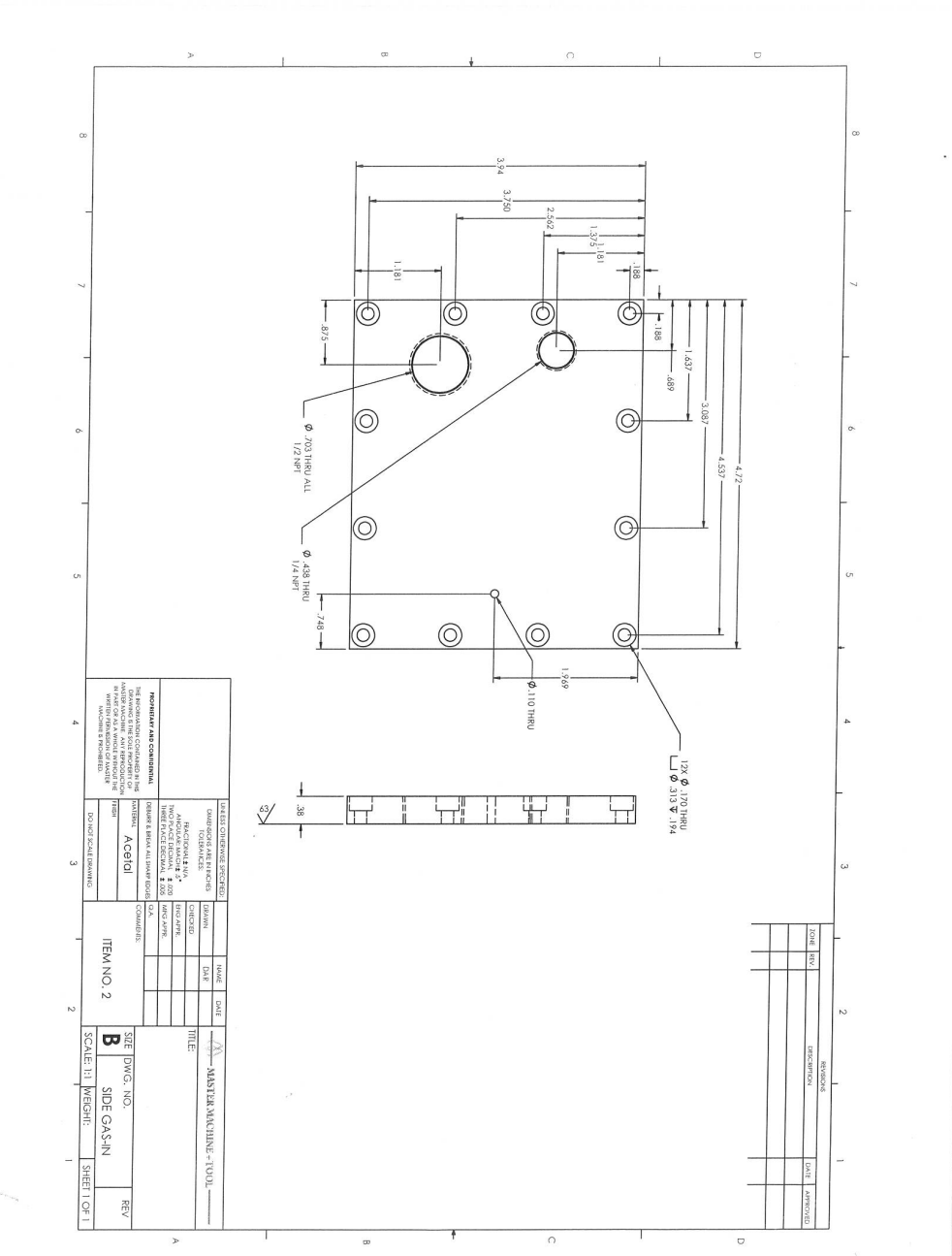
- [44] W. Blum and L. Rolandi, *The Drift of Electrons and Ions in Gases*. Springer, 1993.
- [45] V. Ziegler *et al.*, “The CLAS12 software framework and event reconstruction,” *Nucl. Inst. and Meth. A*, vol. 959, p. 163472, 2020.
- [46] M.E. Christy and P.B. Bosted, “Empirical fit to precision inclusive electron-proton cross sections in the resonance region,” *Phys. Rev. C*, vol. 81, p. 055213, 2010.

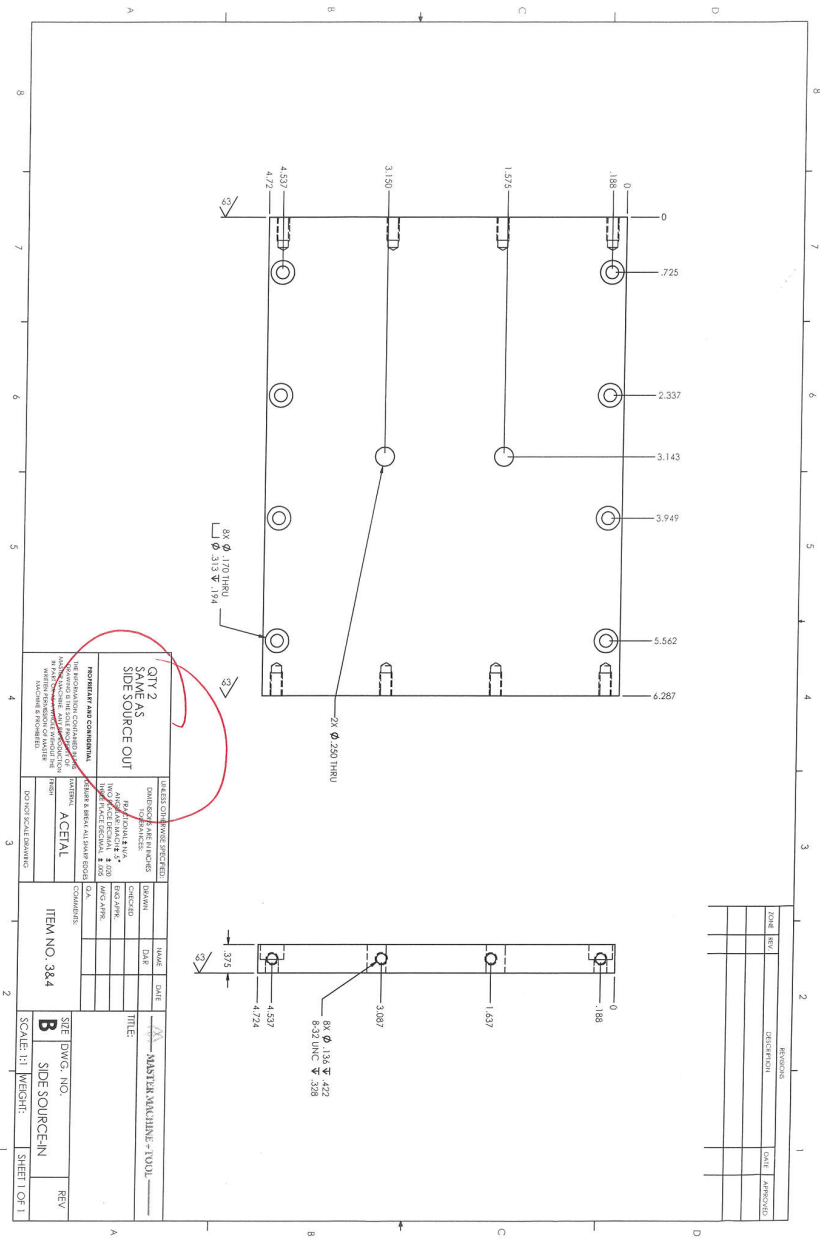
APPENDIX A

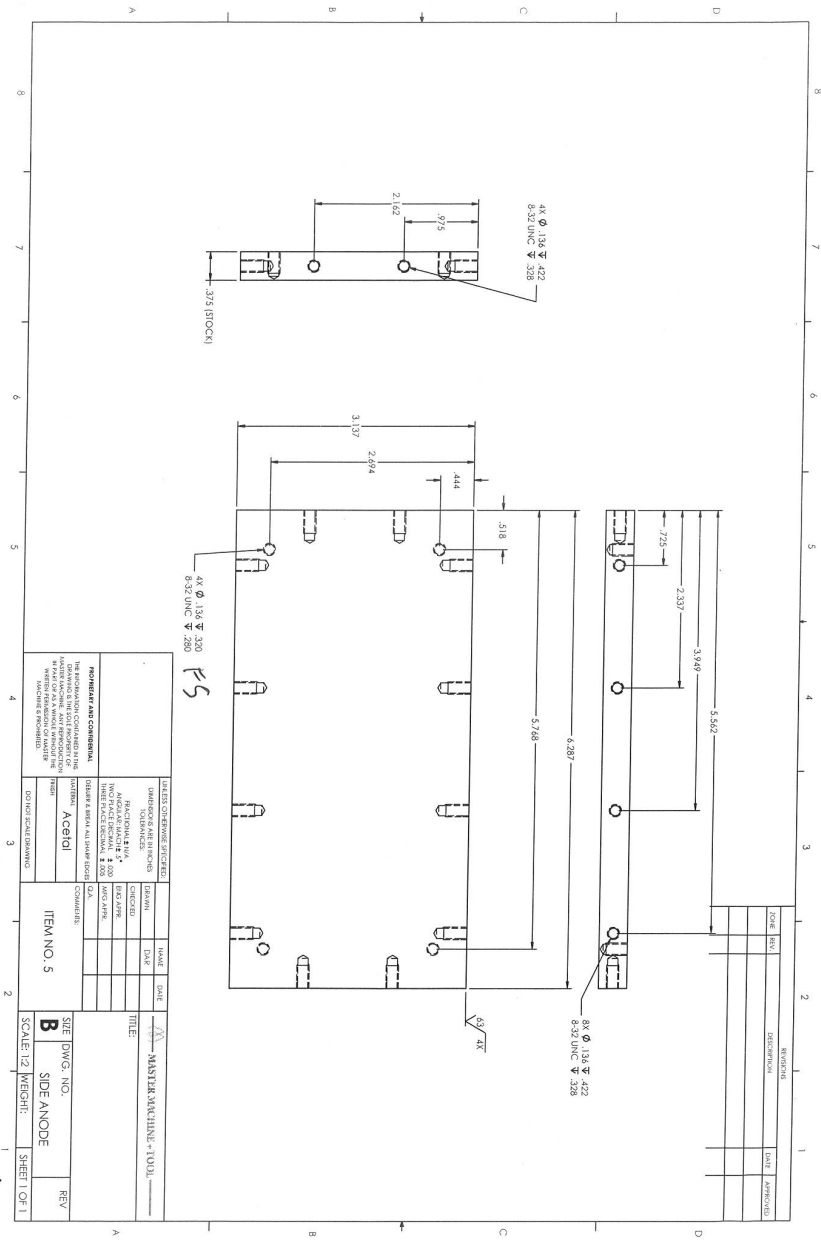
DMS ENGINEERING DRAWINGS

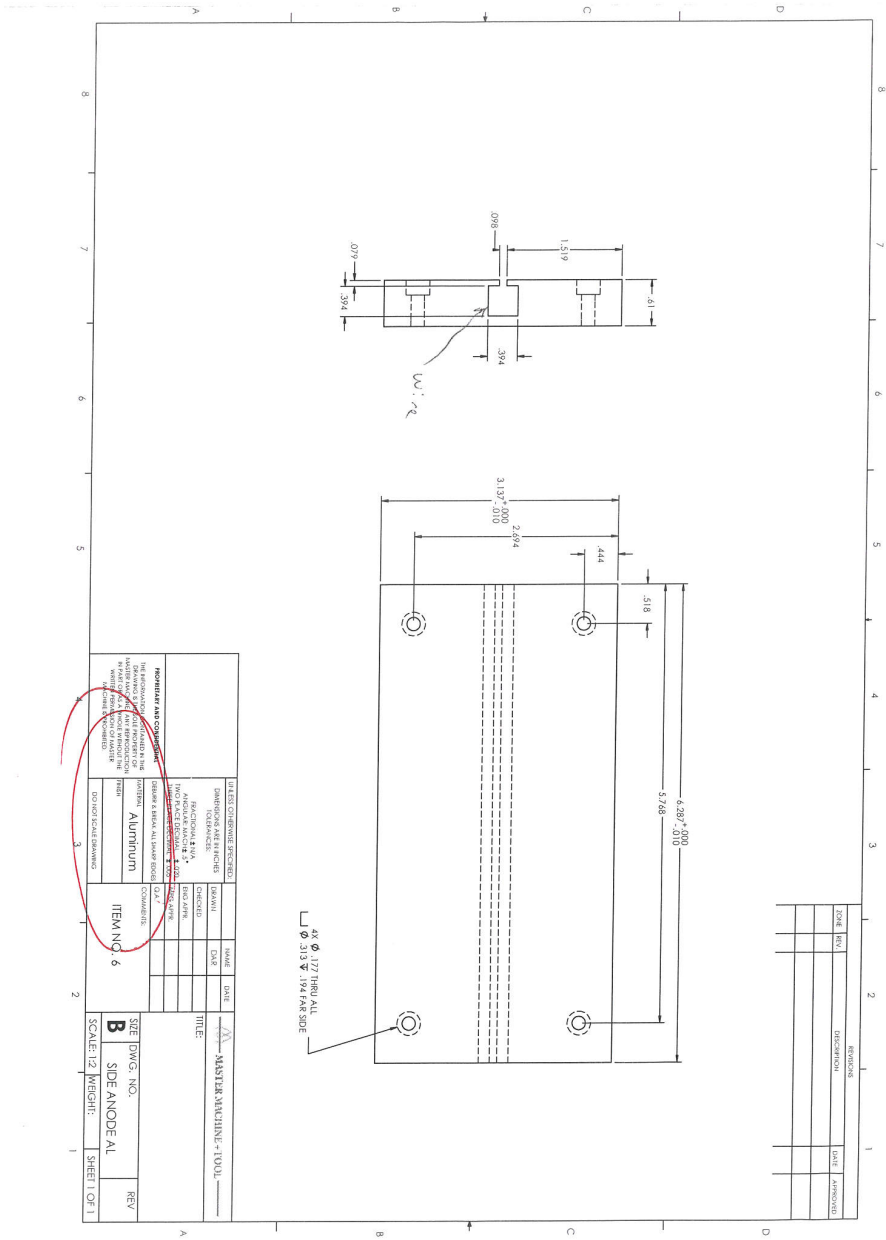


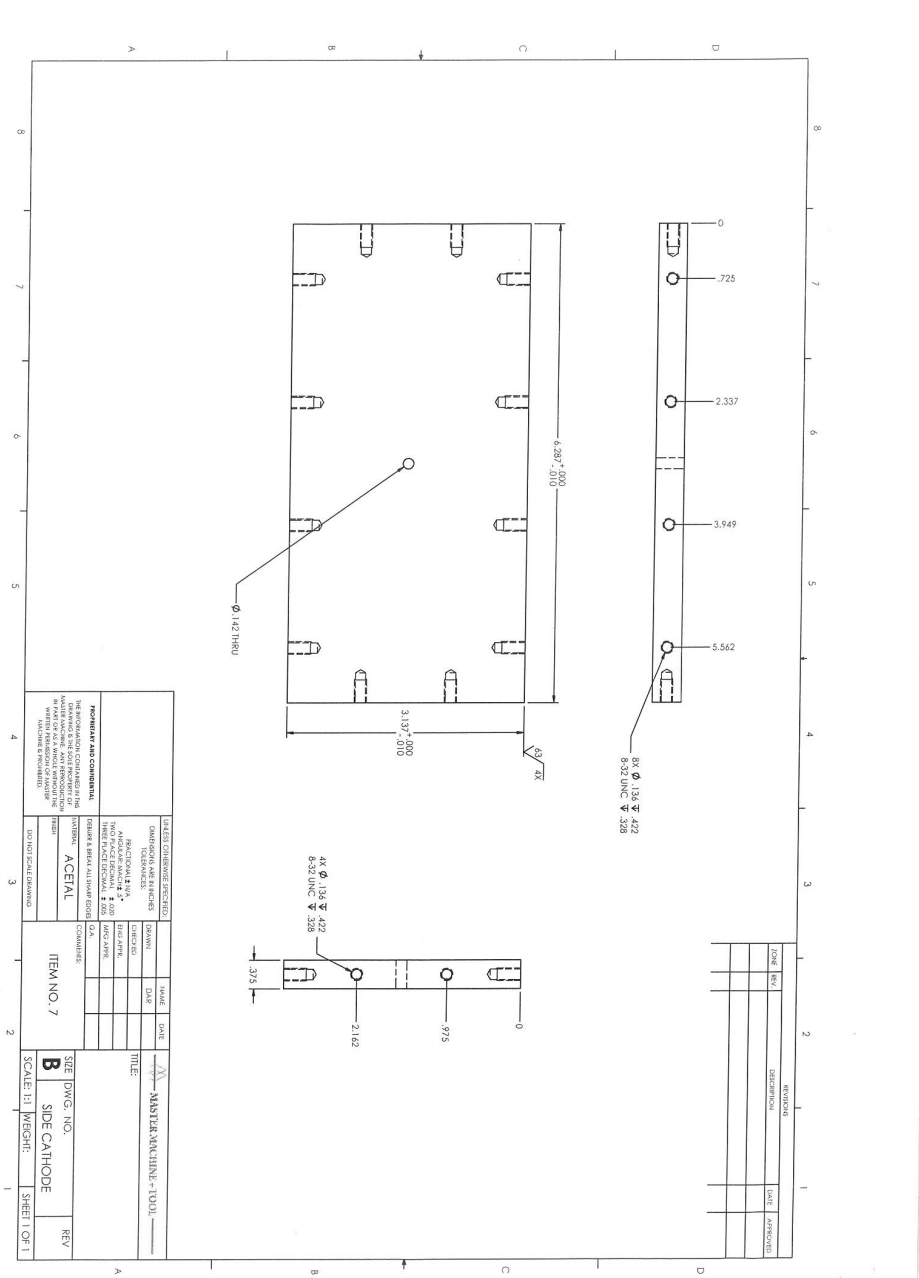


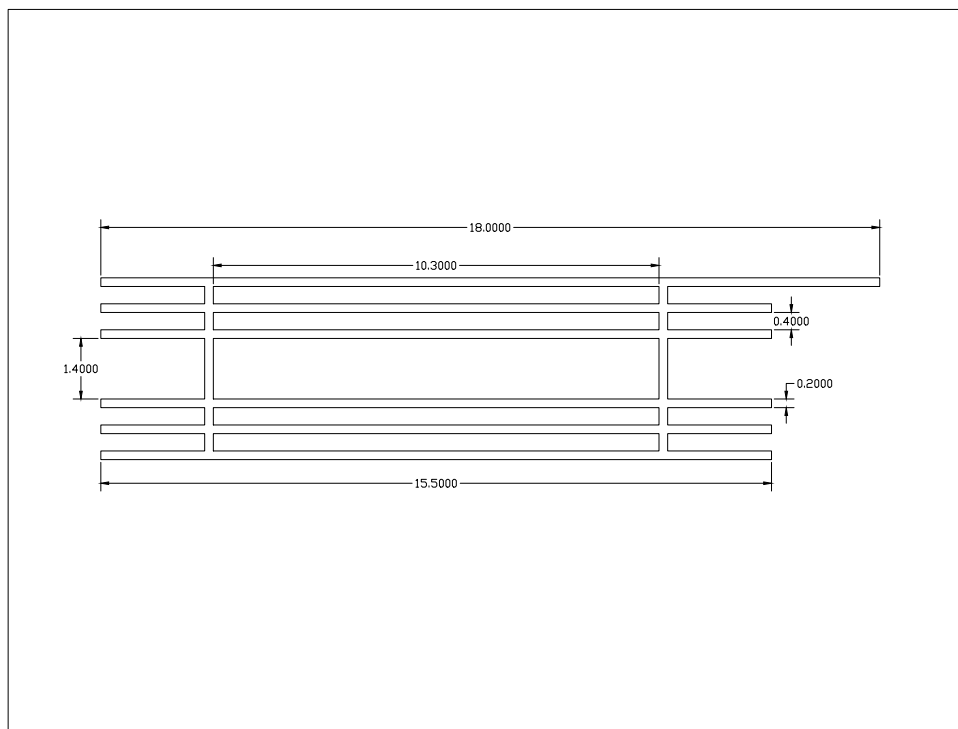












APPENDIX B

DMS GARFIELD++ CODE SNIPPET

```

// Setup the gas
MediumMagboltz* gas = new MediumMagboltz();
gas->SetComposition("He",80.,"CO2",20.);
gas->SetTemperature(293.);
gas->SetPressure(760.);
gas->EnableDrift();           // Allow for drifting in this medium
gas->PrintGas();

// Build the geometry
GeometrySimple* geo = new GeometrySimple();
SolidBox* box = new SolidBox(L_x/2., L_y/2., L_z/2., L_x/2., L_y/2.,
                           L_z/2.);
geo->AddSolid(box, gas);

// Make a component with analytic electric field
ComponentAnalyticField* comp = new ComponentAnalyticField();
comp->SetGeometry(geo);

// Create a sensor for readouts
Sensor* sensor = new Sensor();
sensor->AddComponent(comp);

// Create grounded planes at the edges of the box
comp->AddPlaneX(0.,0.,"x_min");
comp->AddPlaneX(L_x,0.,"x_max");
comp->AddPlaneY(0.,0.,"y_min");
comp->AddPlaneY(L_y,0.,"y_max");

comp->AddReadout("x_min");
comp->AddReadout("x_max");

```

```
comp->AddReadout("y_min");
comp->AddReadout("y_max");

sensor->AddElectrode(comp, "x_min");
sensor->AddElectrode(comp, "x_max");
sensor->AddElectrode(comp, "y_min");
sensor->AddElectrode(comp, "y_max");
```

APPENDIX C

RGA CROSS SECTION DATA

Run 5036

$$\mathcal{L}_{\text{int}} = 2.464 \times 10^{38} \text{ cm}^{-2} = 2.464 \times 10^5 \text{ nb}^{-1}$$

$\langle y \rangle$	$\langle x \rangle$	N_{gen}	N_{rec}	$A(x, y)$	N_{RGA}	$\left(\frac{d^2\sigma}{dxdy}\right)_{\text{MC}}$	$\left(\frac{d^2\sigma}{dxdy}\right)_{\text{RGA}}$
0.3775	0.2255	24965	4621	0.185099	22283	635.759	370.893
0.3775	0.2425	21474	5975	0.278243	31881	536.557	353.011
0.3775	0.2595	18081	6603	0.36519	37104	455.628	313.026
0.3775	0.2765	15657	7021	0.448426	39127	388.89	268.822
0.3775	0.2935	13482	6986	0.518172	39048	333.344	232.167
0.3775	0.3105	11575	6608	0.570886	37860	286.749	204.322
0.3775	0.3275	9903	6000	0.605877	35476	247.398	180.399
0.3775	0.3445	8585	5501	0.640769	33466	213.972	160.912
0.3775	0.3615	7378	4980	0.67498	30918	185.436	141.122
0.3775	0.3785	6473	4558	0.704156	28695	160.971	125.548
0.3775	0.3955	5402	3871	0.716586	26100	139.923	112.215
0.3775	0.4125	4732	3471	0.733516	23455	121.758	98.5155
0.3775	0.4295	4156	3008	0.723773	21327	106.044	90.7842
0.3775	0.4465	3628	2652	0.730981	18607	92.4236	78.4235
0.3775	0.4635	3022	2296	0.759762	16899	80.6008	68.5277
0.3775	0.4805	2506	1835	0.732243	14216	70.3268	59.8129
0.3775	0.4975	1707	1257	0.73638	10390	61.3901	43.4696
0.3775	0.5145	1188	842	0.708754	7210	53.6069	31.345
0.3775	0.5315	750	554	0.738667	4994	46.8132	20.8323

$\langle y \rangle$	$\langle x \rangle$	N_{gen}	N_{rec}	$A(x, y)$	N_{RGA}	$\left(\frac{d^2\sigma}{dxdy}\right)_{\text{MC}}$	$\left(\frac{d^2\sigma}{dxdy}\right)_{\text{RGA}}$
0.455	0.1767	34022	6331	0.186085	25553	714.41	329.922
0.455	0.1985	26342	9249	0.351112	47300	554.687	323.656
0.455	0.2203	21018	10255	0.487915	56519	438.527	278.304
0.455	0.2421	16875	10080	0.597333	58005	351.493	233.301
0.455	0.2639	13783	9335	0.677284	54592	284.738	193.653
0.455	0.2857	11255	8262	0.734074	50129	232.572	164.067
0.455	0.3075	9106	6935	0.761586	44330	191.182	139.847
0.455	0.3293	7629	6079	0.796828	39251	157.932	118.347
0.455	0.3511	6335	5173	0.816575	33933	130.947	99.837
0.455	0.3729	5178	4337	0.837582	28659	108.861	82.2059
0.455	0.3947	4356	3715	0.852847	24658	90.6578	69.4628
0.455	0.4165	3703	3108	0.839319	21287	75.5708	60.9354
0.455	0.4383	2980	2561	0.859396	17395	63.0099	48.6306
0.455	0.4601	2342	1991	0.850128	14805	52.516	41.8424
0.455	0.4819	2136	1881	0.880618	12816	43.7273	34.9655
0.455	0.5037	1671	1465	0.876721	10523	36.3558	28.8367
0.455	0.5255	1342	1178	0.877794	8615	30.1698	23.5803
0.455	0.5473	1140	945	0.828947	7234	24.9815	20.9675
0.455	0.5691	907	741	0.816979	6022	20.6371	17.711

$\langle y \rangle$	$\langle x \rangle$	N_{gen}	N_{rec}	$A(x, y)$	N_{RGA}	$\left(\frac{d^2\sigma}{dxdy}\right)_{\text{MC}}$	$\left(\frac{d^2\sigma}{dxdy}\right)_{\text{RGA}}$
0.5325	0.1649	29526	11870	0.402019	55595	552.249	294.43
0.5325	0.1895	22169	13356	0.602463	69657	409.711	246.164
0.5325	0.2141	16784	12281	0.731709	68901	312.318	200.482
0.5325	0.2387	12929	10293	0.796117	62250	242.772	166.477
0.5325	0.2633	10274	8734	0.850107	53889	191.443	134.964
0.5325	0.2879	8277	7187	0.86831	45449	152.582	111.441
0.5325	0.3125	6716	5967	0.888475	37877	122.566	90.7669
0.5325	0.3371	5416	4900	0.904727	31077	99.0092	73.1336
0.5325	0.3617	4346	3917	0.901289	25911	80.2847	61.2096
0.5325	0.3863	3355	3064	0.913264	21368	65.2489	49.8152
0.5325	0.4109	2764	2468	0.892909	17871	53.078	42.6128
0.5325	0.4355	2264	2076	0.916961	14252	43.1656	33.0932
0.5325	0.4601	1774	1645	0.927283	11644	35.0564	26.735
0.5325	0.4847	1407	1281	0.910448	9594	28.4028	22.4358
0.5325	0.5093	1185	1055	0.890295	7742	22.9351	18.5156
0.5325	0.5339	883	796	0.901472	6195	18.4411	14.6313
0.5325	0.5585	750	639	0.852	4997	14.7519	12.4875
0.5325	0.5831	541	485	0.896488	3882	11.7313	9.22084
0.5325	0.6077	430	361	0.839535	3120	9.26904	7.91464

$\langle y \rangle$	$\langle x \rangle$	N_{gen}	N_{rec}	$A(x, y)$	N_{RGA}	$\left(\frac{d^2\sigma}{dxdy}\right)_{\text{MC}}$	$\left(\frac{d^2\sigma}{dxdy}\right)_{\text{RGA}}$
0.61	0.1531	26802	16287	0.607679	76176	441.511	239.618
0.61	0.1805	19190	15151	0.789526	80706	311.95	195.395
0.61	0.2079	14183	12391	0.873652	70428	229.381	154.093
0.61	0.2353	10587	9811	0.926703	58302	173.266	120.26
0.61	0.2627	7964	7375	0.926042	46571	133.348	96.1302
0.61	0.2901	6423	5990	0.932586	38431	103.971	78.7711
0.61	0.3175	4819	4575	0.949367	30130	81.7869	60.6649
0.61	0.3449	3799	3492	0.919189	24471	64.6991	50.8893
0.61	0.3723	3066	2843	0.927267	20122	51.336	41.4818
0.61	0.3997	2318	2159	0.931406	15796	40.7667	32.4184
0.61	0.4271	1793	1637	0.912995	12666	32.3395	26.5195
0.61	0.4545	1421	1265	0.890218	9957	25.5849	21.3802
0.61	0.4819	1134	1007	0.888007	7942	20.1559	17.0963
0.61	0.5093	827	753	0.91052	6198	15.7898	13.0129
0.61	0.5367	678	620	0.914454	4740	12.2833	9.9085
0.61	0.5641	539	470	0.871985	3965	9.47616	8.69222
0.61	0.5915	393	346	0.880407	3159	7.24015	6.86002
0.61	0.6189	310	260	0.83871	2215	5.47134	5.04823
0.61	0.6463	218	190	0.87156	1805	4.08505	3.95899

$\langle y \rangle$	$\langle x \rangle$	N_{gen}	N_{rec}	$A(x, y)$	N_{RGA}	$\left(\frac{d^2\sigma}{dxdy}\right)_{\text{MC}}$	$\left(\frac{d^2\sigma}{dxdy}\right)_{\text{RGA}}$
0.6875	0.1413	25958	20150	0.776254	89924	361.441	200.905
0.6875	0.1715	17329	15894	0.917191	83855	242.556	158.558
0.6875	0.2017	12257	11543	0.941748	66567	172.456	122.585
0.6875	0.2319	8947	8490	0.948921	52184	127.087	95.3729
0.6875	0.2621	6666	6223	0.933543	40629	95.8312	75.4773
0.6875	0.2923	4967	4671	0.940407	31532	73.3217	58.1518
0.6875	0.3225	3740	3538	0.945989	24739	56.5792	45.3543
0.6875	0.3527	2731	2544	0.931527	18867	43.833	35.1256
0.6875	0.3829	2261	2081	0.920389	14717	33.9714	27.7311
0.6875	0.4131	1742	1586	0.910448	11502	26.263	21.9102
0.6875	0.4433	1274	1149	0.901884	9061	20.2051	17.4243
0.6875	0.4735	996	911	0.914659	6942	15.4375	13.163
0.6875	0.5037	708	625	0.882768	5395	11.6924	10.6004
0.6875	0.5339	562	493	0.877224	4006	8.7641	7.92051
0.6875	0.5641	434	359	0.827189	3071	6.48992	6.44009
0.6875	0.5943	282	235	0.833333	2073	4.73932	4.31501
0.6875	0.6245	229	167	0.729258	1482	3.40624	3.52439
0.6875	0.6547	141	112	0.794326	1085	2.40443	2.36906
0.6875	0.6849	96	77	0.802083	784	1.66429	1.69708

$\langle y \rangle$	$\langle x \rangle$	N_{gen}	N_{rec}	$A(x, y)$	N_{RGA}	$\left(\frac{d^2\sigma}{dxdy}\right)_{\text{MC}}$	$\left(\frac{d^2\sigma}{dxdy}\right)_{\text{RGA}}$
0.765	0.1295	25671	22945	0.89381	102268	299.291	181.595
0.765	0.1625	16441	15708	0.955416	86118	190.64	143.058
0.765	0.1955	10900	10343	0.948899	63196	131.851	105.701
0.765	0.2285	7608	7260	0.954259	46601	95.4216	77.5063
0.765	0.2615	5678	5218	0.918986	35199	70.8604	60.7906
0.765	0.2945	4137	3839	0.927967	26509	53.3397	45.34
0.765	0.3275	2968	2667	0.898585	20102	40.3604	35.505
0.765	0.3605	2192	2020	0.921533	15123	30.5148	26.047
0.765	0.3935	1718	1515	0.881839	11586	22.9507	20.8536
0.765	0.4265	1214	1106	0.911038	8197	17.115	14.2803
0.765	0.4595	931	772	0.829216	6203	12.6223	11.8731
0.765	0.4925	614	508	0.827362	4402	9.18713	8.44586
0.765	0.5255	513	382	0.744639	2982	6.5871	6.35748
0.765	0.5585	344	253	0.735465	2166	4.64366	4.67578
0.765	0.5915	250	179	0.716	1441	3.21167	3.19476
0.765	0.6245	169	116	0.686391	1085	2.17323	2.50986
0.765	0.6575	125	79	0.632	704	1.43374	1.76802
0.765	0.6905	93	63	0.677419	436	0.918837	1.02342
0.765	0.7235	44	31	0.704545	255	0.572246	0.575135

VITA

Nathan M Dzbenksi
Department of Physics
Old Dominion University
Norfolk, VA 23529

Nathan Dzbenksi received a Bachelor of Science degree in physics from the University of North Carolina Wilmington (Wilmington, NC) in 2014. The same year he started graduate school at Old Dominion University (Norfolk, VA), where he received a Masters of Science degree in physics (Nuclear Physics) in 2016. In 2016, he began the Ph.D. program in physics (Experimental Nuclear Physics) at Old Dominion University (Norfolk, VA). The projected date of graduation is August 2020. Nathan Dzbenksi is a member of the American Physical Society, CLAS (CEBAF Large Acceptance Spectrometer) collaboration, and CLAS12 Deep Processes Physics Working Group.